Adaptively Refined Large-Eddy Simulations of Galaxy Clusters

Dissertation zur Erlangung des
naturwissenschaftlichen Doktorgrades
der Bayerischen Julius-Maximilians-Universität Würzburg

vorgelegt von
Andreas Maier
aus Coburg

Würzburg 2008

Eingereicht am
bei der Fakultät für Physik und Astronomie

1. Gutachter: Prof. Dr. Jens Niemeyer
2. Gutachter:
der Dissertation

1. Prüfer: Prof. Dr. Jens Niemeyer
2. Prüfer:
3. Prüfer:
im Promotionskolloquium

Tag des Promotionskolloquiums:

Doktorurkunde ausgehändigt am ______________

Посвящаю Ольге

Contents

1 Introduction **9**

1.1 Historical overview . . . 9

1.2 Aim of this work . . . 12

2 Turbulence **15**

2.1 Phenomenology of Turbulence . . . 16

2.2 The Kolmogorov theory . . . 18

3 Filter formalism **21**

3.1 Reynolds filter . . . 21

3.2 Germano formalism . . . 22

3.3 Favre-Germano formalism . . . 23

3.4 Explicit filtering . . . 24

4 Favre-filtered equations of fluid dynamics **27**

4.1 Basic equations . . . 27

4.2 Resolved energy and turbulent energy equations . . . 28

4.3 Summary . . . 30

5 LES and SGS model **33**

5.1 The concept of LES . . . 33

5.2 Schmidt model . . . 34

- 5.2.1 Transport term $\mathbb{D}$ . . . 34
- 5.2.2 Pressure dilatation λ . . . 34
- 5.2.3 Turbulent dissipation ϵ . . . 35
- 5.2.4 Turbulence production tensor $\hat{\tau}(v_i, v_j)$ . . . 35
- 5.2.5 Summary of the Schmidt model . . . 36

5.3 Impact of the Schmidt SGS on the fluid equations . . . 36

- 5.3.1 General observations . . . 36
- 5.3.2 Dimensional analysis . . . 38

5.4 Sarkar model . . . 41

- 5.4.1 Turbulent dissipation ϵ . . . 41
- 5.4.2 Pressure dilatation λ . . . 41

6 AMR and LES **43**
6.1 Adaptive mesh refinement . . . 43
6.2 Attempts to combine LES and AMR . . . 45
6.3 ϵ-based approach to combine AMR and LES . . . 46

7 Numerical testing **49**
7.1 The Enzo code . . . 49
7.2 Modifications to Enzo . . . 50
7.2.1 Turbulent energy as a color field . . . 50
7.2.2 Coupling of turbulent energy and time step restriction . . . 51
7.2.3 Transfer of turbulent energy at grid refinement/derefinement . 51
7.2.4 Random forcing . . . 53
7.2.5 Statistics tool . . . 53
7.3 Energy conservation . . . 53
7.4 Scaling of turbulent energy . . . 56
7.5 Comparison of static grid to AMR turbulence simulations . . . 57

8 Cluster physics **61**
8.1 Cluster formation . . . 61
8.1.1 Initial density fluctuations . . . 61
8.1.2 Hierarchical growth of density fluctuations . . . 62
8.2 Intracluster medium . . . 63
8.2.1 Mean free path of the ICM . . . 63
8.2.2 Magnetic fields . . . 64
8.2.3 X-ray observations of the ICM . . . 65
8.2.4 Turbulence in the ICM . . . 67

9 Simulations of galaxy clusters **71**
9.1 Details of the simulations . . . 71
9.1.1 Common features . . . 71
9.1.2 Numerical issues . . . 72
9.2 Results . . . 74
9.2.1 Energy conservation . . . 74
9.2.2 Mass fractions of different gas phases . . . 75
9.2.3 Development of turbulence in different gas phases . . . 77
9.2.4 Scaling of turbulent energy . . . 79
9.2.5 Radial profiles of the cluster . . . 81
9.2.6 Spatial distribution of turbulent energy . . . 86
9.2.7 Cluster core analysis . . . 89
9.2.8 Influence of SGS parameters on cluster core . . . 91

10 Summary and Conclusions **93**

A Dimensional analysis 97

B Properties of second order tensors 101

C Derivation of the stress tensor for a newtonian fluid 103

D Fourier transform and structure functions 105
- D.1 Fourier transform of a delta function . . . 106
- D.2 Convolution theorem . . . 107
- D.3 Autocorrelation and Wiener-Khinchin Theorem . . . 107
- D.4 Structure functions . . . 109

E The divergence equation 111

F Vlasov-Poisson Equations 113

G Hydrostatic equilibrium 115
- G.1 Standard derivation . . . 115
- G.2 Derivation including turbulent pressure . . . 116

H Fluid dynamics in comoving coordinates 117
- H.1 Introduction . . . 117
- H.2 Useful transformations . . . 118
- H.3 Equations in comoving coordinates . . . 119

I Color fields 121

Bibliography 123

1 Introduction

1.1 Historical overview

Clusters of galaxies are the largest and most recent gravitationally-relaxed structures in the universe. They typically contain hundreds to thousands of galaxies with a total mass of about $10^{14} - 10^{15}$ solar masses ($\mathrm{M}_{\odot}$), spread over a region whose size is roughly 10 million light-years (Mly). Galaxy clusters themselves form even greater structures called superclusters, which are gravitationally-attracted, but not relaxed, collections of ten to one hundred clusters and groups of galaxies. The Milky Way itself belongs to the "Local Group" , which is an aggregation of about 40 galaxies, with the Andromeda Galaxy and the Milky Way as the largest members of the group. The Local Group belongs to the "Virgo Supercluster", with the Virgo cluster at the center. The Virgo cluster is the nearest cluster of galaxies to our own galaxy at a distance of 60 Mly; another famous cluster of galaxies is the Coma cluster, which is called a very regular cluster, because it is nearly spherically symmetric (see figure 1.1).

The tendency of galaxies to form clusters in the sky has long been noticed (for example Messier (1784) had identified already 16 galaxies, which - as we now know - belong to the Virgo cluster, and he noted that they form a group), but the first to study them in detail was Wolf (1906). A great step forward in the systematic study of the properties of clusters was the work of Abell (1958), who compiled the first extensive, statistically complete catalog of so-called rich clusters of galaxies[1]. This catalog and its successors (e.g. Abell et al. (1989)) are the foundation for much of our modern understanding of clusters.

The cited catalogs of clusters are based on optical identification techniques. However in the early 1970s extended x-ray emission from clusters of galaxies was observed by Gursky et al. (1971); Kellogg et al. (1972), which had been already correctly attributed to thermal bremsstrahlung several years earlier by Felten et al. (1966). This interpretation requires the space between galaxies in clusters to be filled with a very hot ($\approx 10^8\,\mathrm{K}$) low density ($\approx 10^3\,\mathrm{atoms/m^3}$) gas. Remarkably, the total mass in this intracluster medium (ICM) is comparable to the total mass of all galaxies in the cluster. Nevertheless this discovery did not solve the so called missing mass problem in clusters, which was first formulated by Zwicky (1933, 1937). Zwicky (1933) was

---

[1] The richness of a galaxy is a measure that is basically proportional to the number of bright galaxies in a cluster. It was first strictly defined by Abell for his catalog.

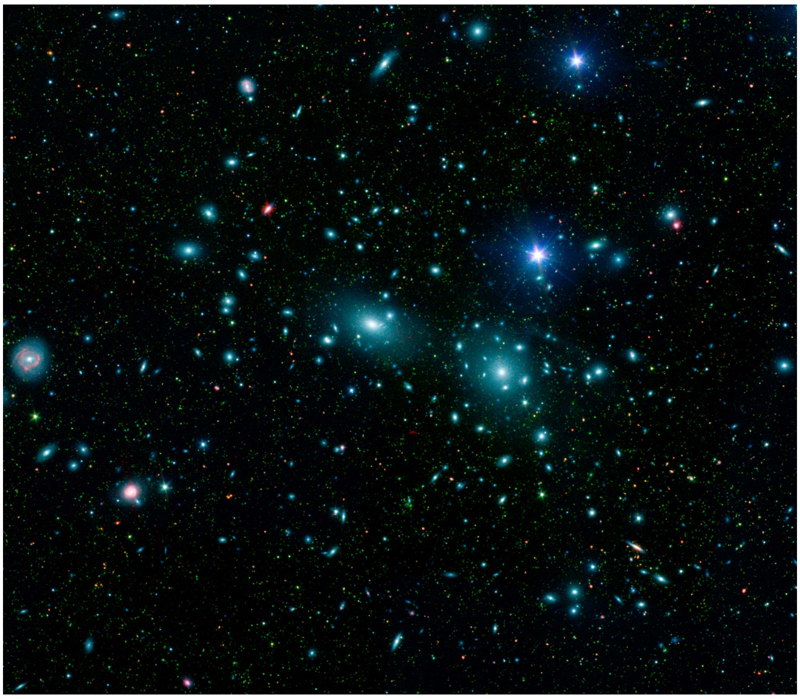

Figure 1.1: A Sloan Digital Sky Survey/Spitzer Space Telescope image of the Coma Cluster in ultraviolet and visible light. From Jenkins (2007).

the first to measure the velocity dispersion of galaxies in the Coma cluster, finding $\sigma_{galaxy} = 700\,\mathrm{km\ s}^{-1}$, and he correctly concluded from this fact and his estimate of the Coma's cluster overall radius, that the cluster mass, which he computed using the virial theorem, must be far greater than the observed luminous mass - the first evidence for dark matter in the universe. In his remarkable paper of 1937, Zwicky also proposed gravitational lensing as an alternative technique for measuring the masses of background galaxies. This technique finally became practicable after six more decades (Tyson et al., 1990), and is now a standard technique for measuring cluster mass (Bartelmann, 2003).

Measuring the masses of clusters is not only important for the search of dark matter. Some of the most powerful constraints on current cosmological models come from observations of how the cluster mass function $n(M)$, which gives the number density of clusters with a mass greater than M in comoving volume element, evolves with time (Voit, 2005). The reason why the evolution of the cluster mass function is so highly sensitive to cosmology is simply because the matter density of the universe controls the rate at which structure grows. The cluster mass function can be measured using optical surveys. However it is easier to use X-ray surveys, because in the X-ray band, instead of a collection of galaxies, each cluster appears only as a single source (see figure 1.2), which makes it observationally easier to define consistently cluster properties like the radius. Independently from Supernova IA

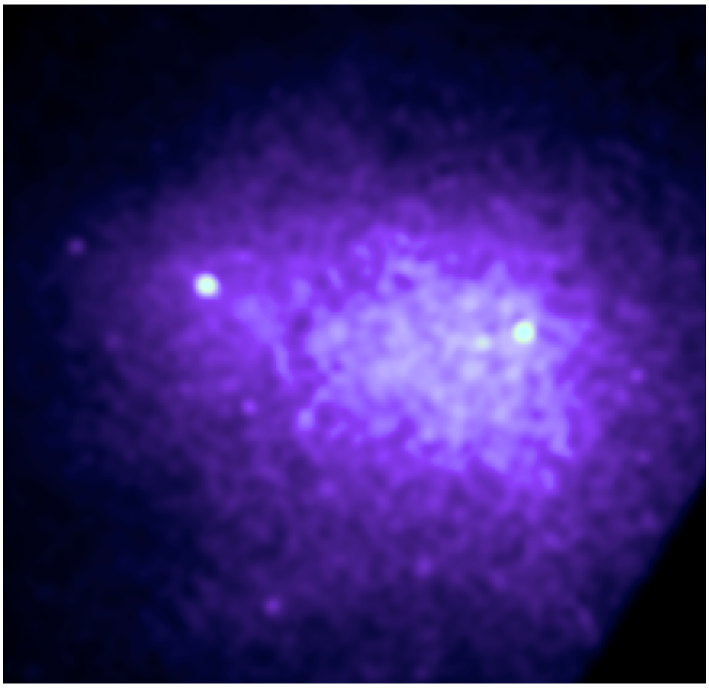

Figure 1.2: Chandra X-ray image of the central region of the Coma Cluster. From Vikhlinin (2002).

and cosmic microwave background (CMB) measurements, these and other cluster-related surveys can now restrict several important parameters of the cosmological concordance model (see figure 1.3).

Most of these cluster surveys make use of several relations like the mass-temperature or luminosity-temperature relation, which are only based on observational findings. If gravity alone would determine the thermodynamical properties of the clusters, we would expect clusters to be self-similar, meaning clusters of different size would be scaled versions of each other, leading to a specific simple form of these relations (Kaiser, 1986). However astronomers have known for more than a decade that the intracluster medium cannot be self-similar, because the luminosity-temperature relation of clusters does not agree with self-similar scaling (Voit, 2005). So only by breaking the self-similar scaling of clusters can the observed relations be explained. But it is theoretically still uncertain, which mechanism(s) is (are) responsible for that similarity breaking. Many mechanisms have been proposed including preheating, radiative cooling, feedback from supernovae, feedback from active galactic nuclei (Voit, 2005), shocks, magnetic fields, cosmic rays and turbulence (Dolag et al., 2008). It therefore remains a challenge for the theory of cluster physics to find the responsible mechanisms and explain the relations mentioned above.

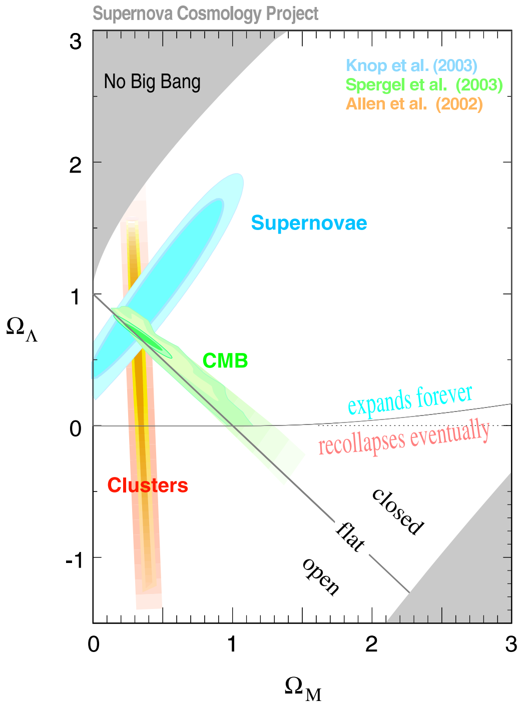

Figure 1.3: Plot of 68% and 90% confidence regions for Ω_M and Ω_Λ for Supernova IA, CMB and cluster data. From Knop et al. (2003).

1.2 Aim of this work

One of the proposed mechanisms that break gravitationally self-similar scaling properties of clusters is turbulence. Turbulence is also believed to play an important role in explaining the magnetic field strengths of galaxy clusters and the higher than expected temperature of cluster cores (the "cooling flow problem"). However numerical simulations of the influence of turbulence in an astrophysical context in general and especially for clusters have been restricted to measuring passively statistical quantities like velocity dispersion from simulation data (e.g. Dolag et al. (2005b)). The active role of small scale velocity fluctuations on the large scale flow could not be treated at all. There are two main reasons for this:

1. Basically turbulence is a physical phenomenon that is far from being understood. The sole currently existing theory is only applicable to isotropic, incompressible turbulence. No accepted theoretical framework for describing turbulent flows in astrophysical environment including compressible, selfgravitating, high Mach number flows exists.

2. Models describing the effective influence of turbulence in fluid dynamic simulations are restricted to a specific length scale. They are not suitable to treat the vast range of different length scales (from cosmological scales $\approx 10^{24}$ m

down to the thickness of a shock front ($\approx 10^{11}$ m, Medvedev et al. (2006)) we need to address when simulating astrophysical environments.

Therefore it is aim of this work to develop, implement, and apply a new numerical scheme for modeling turbulent, multiphase astrophysical flows such as galaxy cluster cores and star forming regions. The method combines the capabilities of adaptive mesh refinement (AMR) and large-eddy simulations (LES) to capture localized features and to represent unresolved turbulence, respectively; it will be referred to as Fluid mEchanics with Adaptively Refined Large-Eddy SimulationS or FEARLESS.

To start explaining the idea behind this ansatz, we first give a brief overview of the theory of turbulence in chapter 2. In chapter 3 we introduce a filter formalism, which is necessary for modeling compressible turbulence according to the ideas of LES. In chapter 4 we use this formalism to derive the filtered equations of fluid dynamics, which are the basis for the introduction of our turbulence or subgrid scale (SGS) model (adapted from work by Schmidt et al. (2006a)) in chapter 5. In this chapter we also analyse in some detail the influence of the turbulence model on the equation of fluid dynamics. In chapter 6 we explain the specific problem of combining LES and AMR in some detail and propose a new method to circumvent this problem. In chapter 7 we comment on several modifications and numerical issues that had to be taken into account when implementing our method into the cosmological fluid code Enzo. We also present the results of several driven turbulence test simulations, showing the consistency of our treatment of turbulence. Chapter 8 summarizes some important facts about cluster physics and we also give a brief introduction to turbulence in cluster simulations. In chapter 9 we describe several issues with our turbulence model when treating turbulence in cluster simulations on cosmological scales. We explain our setup and then describe the main results of a first study of turbulence in galaxy cluster simulations using our FEARLESS approach. Finally in chapter 10 we summarize our findings and draw conclusions about the influence of turbulence in the context of cluster simulations.

2 Turbulence

The equations for a general compressible, viscous, selfgravitating fluid with density $\rho(r_i, t)$, momentum density $\rho v_i(r_i, t)$ and total energy density $\rho e(r_i, t)$ are[1]

$$\frac{\partial}{\partial t}\rho + \frac{\partial}{\partial r_j}(v_j \rho) = 0, \tag{2.1}$$

$$\frac{\partial}{\partial t}(\rho v_i) + \frac{\partial}{\partial r_j}(v_j \rho v_i) = -\frac{\partial}{\partial r_i} p + \frac{\partial}{\partial r_j}\sigma'_{ij} + \rho g_i, \tag{2.2}$$

$$\frac{\partial}{\partial t}(\rho e) + \frac{\partial}{\partial r_j}(v_j \rho e) = -\frac{\partial}{\partial r_j}(v_j p) + \frac{\partial}{\partial r_j}(v_i \sigma'_{ij}) + v_i \rho g_i, \tag{2.3}$$

with Newtonian gravity (Poisson Equation)

$$\frac{\partial}{\partial r_j} g_j = 4\pi G \rho \tag{2.4}$$

and an equation of state to compute the pressure $p(r_i, t)$ dependent on the material of the fluid. For a Newtonian fluid the stress tensor σ_{ij} is of the form[2]

$$\sigma'_{ij} = 2\eta \left[\frac{1}{2}\left(\frac{\partial v_i}{\partial r_j} + \frac{\partial v_j}{\partial r_i} \right) - \frac{1}{3}\delta_{ij}\frac{\partial v_k}{\partial r_k} \right] + \zeta \delta_{ij} \frac{\partial v_k}{\partial r_k}, \tag{2.5}$$

where the so called dynamic viscosity η and the second viscosity ζ are defined to be constants[3] in a Newtonian fluid.

This system of differential equations is complex and highly nonlinear if the nonlinear advection term $\frac{\partial}{\partial r_j}(v_j \rho v_i)$ dominates in the momentum equation (2.2) and in general can be solved only numerically. The influence of the advection term can be estimated by writing down the momentum equation in dimensionless form, which yields[4]

$$\underbrace{\frac{l_0}{v_0 t_0}}_{Sr} \frac{\partial}{\partial t^*}(\rho^* v_i^*) + \frac{\partial}{\partial r_j^*}(v_j^* \rho^* v_i^*) = -\underbrace{\frac{p_0}{\rho_0 v_0^2}}_{Ma_{iso}^{-2}} \frac{\partial}{\partial r_i^*} p^* + \underbrace{\frac{\sigma_0}{\rho_0 v_0^2}}_{Re^{-1}} \frac{\partial}{\partial r_j^*}\sigma_{ij}^* + \underbrace{\frac{\rho_0 g_0 l_0}{\rho_0 v_0^2}}_{Fr^{-1}} \rho^* g_i^*. \tag{2.6}$$

---

[1] see eg. Landau and Lifschitz (1991).

[2] For a derivation see Appendix C.

[3] The literature on incompressible flows often defines the so called kinematic viscosity $\nu = \frac{\eta}{\rho}$. It should be noted, that this quantity is a constant only for fluids of constant density and cannot be used in a meaningful way when discussing compressible flows.

[4] See Appendix A.

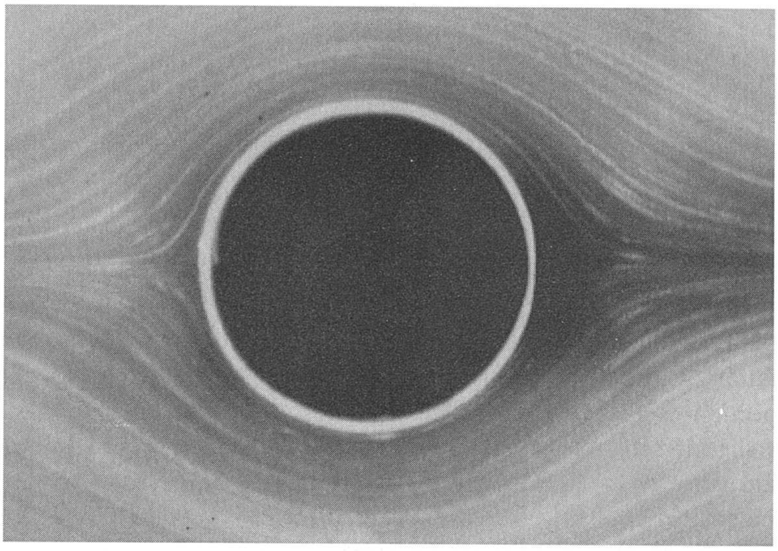

Figure 2.1: Laminar flow past a cylinder at $Re = 0.16$ (Frisch, 1995).

The arising dimensionless numbers[5] (Re = Reynolds number, Ma_{iso} = isothermal Mach number, and Fr = Froude number) show the ratio of the mean pressure energy density p_0, the mean potential energy density $\rho_0 g_0 l_0$, and the mean energy dissipation density σ_0 to the mean kinetic energy density $\rho_0 v_0^2$. If all these numbers are much greater than one (which means the mean kinetic energy is big compared to the other energies), the advection term dominates and the fluid flow is called turbulent.

2.1 Phenomenology of Turbulence

As there is no accepted theory of compressible, selfgravitating turbulence we have to restrict the following discussion to incompressible turbulence. For an incompressible fluid, it can be shown that the Reynolds number

$$Re = \frac{\rho_0 v_0^2}{\sigma_0} = \frac{\rho_0 l_0 v_0}{\eta_0} \tag{2.7}$$

is the only number which characterizes the dynamics of the fluid flow (Feynman, 1964).

If the Reynolds numbers is small, which is the case for high viscosity and/or low flow speed, we call the fluid laminar. In this laminar state the streamlines of the fluid exhibit all the symmetries of the equations and boundary conditions. This

---

[5] The Strouhal number Sr can be set to one by assuming $v_0 = \frac{l_0}{t_0}$.

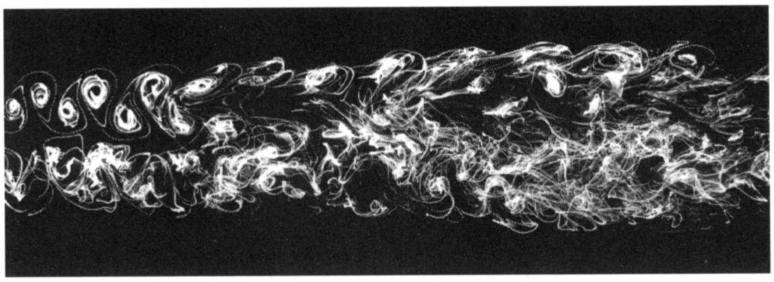

(a) $Re = 240$

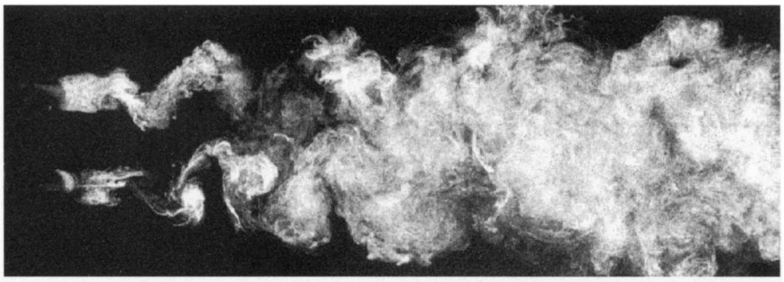

(b) $Re = 1800$

Figure 2.2: Wake behind two identical cylinders (Frisch, 1995).

can be seen in figure 2.1, where the streamlines of a fluid around a cylinder show up-down and left-right symmetry.[6]

With increasing Reynolds number, the left-right symmetry first (figure 2.2(a)) and then the up-down symmetry are broken (figure 2.2(b)). If $Re > 1000$, the flow becomes completely chaotic and all symmetries are broken. Nevertheless, looking at the flow at smaller scales l far from the boundaries, all the symmetries of the equations seem to be restored in a statistical sense. This state of flow is called fully developed turbulence.

However at the smallest scales of the flow l_k, the flow will "behave" laminar again. This means that the Reynolds number becomes smaller on smaller scales and implies that the Reynolds number is scale dependent

$$Re(l) = \frac{\rho v(l) l}{\eta}. \tag{2.8}$$

How the Reynolds number depends on the scales of the flow is explained by the Kolmogorov theory of incompressible turbulence.

---

[6] Actually the streamlines also show z-invariance (along the axes of the cylinder) and time-invariance, but they do not show cylindrical symmetry as the direction of the fluid flow breaks this symmetry.

2.2 The Kolmogorov theory

Kolmogorov first described his theory of turbulence in 1941. Here we discuss the modern formulation of the Kolmogorov theory as explained in Frisch (1995) and Pope (2000).

According to Frisch, Kolmogorovs theory is based on three assumptions which are valid in the limit of infinite Reynolds numbers, at small scales l ($l_k \ll l \ll l_0$) and away from boundaries:

1. All the possible symmetries of the Navier-Stokes equation, usually broken by the mechanisms producing the turbulent flow, are restored in a statistical sense.

2. The turbulent flow is self-similar.

3. The turbulent flow has a finite nonvanishing mean rate of dissipation $\langle\epsilon\rangle$ per unit mass.

The mean rate of dissipation is defined as the mean rate of change of kinetic energy

$$\langle\epsilon\rangle = \langle\frac{d}{dt}e_{kin}\rangle \sim \frac{v_0^2}{l_0/v_0} = \frac{v_0^3}{l_0} = const. \tag{2.9}$$

Using this Kolmogorov derived, that for homogeneous and isotropic incompressible turbulence the third order structure function[7] $S_3(v(l))$ is equal to the mean rate of dissipation times minus four-fifths the length scale l of the structure function

$$S_3(v(l)) = -\frac{4}{5}\langle\epsilon\rangle l. \tag{2.10}$$

This is the famous four-fifths law of Kolmogorov. From it and the self similarity assumption, Kolmogorov deduces that the structure functions of order p scale like

$$S_p(v(l)) \sim \langle\epsilon\rangle^{p/3} l^{p/3}. \tag{2.11}$$

Because the second order structure function can be expressed as Fourier transform of the longitudinal velocity spectrum[8] $\left|V_{\|}(k)\right|^2 \sim e_{kin}(k)$ and the wave numbers k are related to length scales l via $k \sim l^{-1}$ it follows for the specific kinetic energy in Fourier space

$$e_{kin}(k) \sim \langle\epsilon\rangle^{2/3} k^{-2/3}. \tag{2.12}$$

---

[7] For a definition of structure functions see appendix D.4.

[8] Also see appendix D.4.

The energy spectrum $E(k)$ is the kinetic energy in the wave number interval between k and $k + dk$, which is then

$$E(k) \sim \frac{d}{dk} e_{kin}(k) = C_k \langle \epsilon \rangle^{2/3} k^{-5/3}. \tag{2.13}$$

This is the celebrated result of Kolmogorovs theory of incompressible turbulence. The constant C_k is therefore called the Kolmogorov constant and is experimentally and numerically found to be $C_k \approx 1.6$ (Yokokawa et al., 2002).

It should be noted that the rate of dissipation $\langle \epsilon \rangle$ is not the rate of conversion of kinetic energy into internal energy, rather it describes the amount of energy which is transfered from the bigger to the smaller scales, without the influence of viscosity. The kinetic energy is converted to internal energy only on scales smaller than the Kolmogorov scale l_k, where the Reynolds number becomes unity. From this and the relation $S_1(v(l)) \sim v(l) \sim \langle \epsilon \rangle^{1/3} l^{1/3}$ we can derive an expression for the Kolmogorov scale

$$Re(l_k) = 1 = \frac{\rho v_{l_k} l_k}{\eta} = \frac{\langle \epsilon \rangle^{1/3} l_k^{4/3}}{\nu} \Rightarrow l_k = \left(\frac{\nu^3}{\langle \epsilon \rangle} \right)^{1/4}. \tag{2.14}$$

Using the definition of the dissipation (2.9) in (2.14), we obtain for the ratio between the largest integral length l_0 and the Kolmogorov length l_k

$$\frac{l_0}{l_k} = \left(\frac{\nu^3}{l_0^3 v_0^3} \right)^{-1/4} = Re^{3/4}. \tag{2.15}$$

We can use this to estimate the number of degrees of freedom of a three-dimensional fluid flow at a point of time

$$N_f = \left(\frac{l_0}{l_k} \right)^3 = Re^{9/4}. \tag{2.16}$$

One consequence of this is that the storage requirement of a fully resolved numerical simulation grows as $Re^{9/4}$. [9] Since the time step must usually be taken proportional to the spatial mesh, the total number of operations to integrate the equations for a fixed number of dynamical times is

$$N = \left(\frac{l_0}{l_k} \right)^4 = Re^3. \tag{2.17}$$

As the typical Reynolds numbers in astrophysical context are of the order of 10^8 (Kritsuk et al., 2007) up to 10^{14} (Schmidt et al., 2006a) we would need a computer with at least 10^{18} Bytes (1 Exabyte) of memory and 10^{16} FLOPS[10] (10 PetaFLOPS) running for a year to resolve fully an astrophysical simulation. And even if we could efficiently make use of the fact, that turbulence is not volume filling at a point of time, it remains intractable to resolve completely the turbulent fluid dynamics encountered in astrophysics (Schmidt et al., 2006a).

---

[9] Using this to estimate the Reynolds number from the biggest direct numerical simulation today by Yokokawa et al. (2002) on the Earth simulator with a resolution of 4096^3 grid cells yields $Re \approx 65536$.

Therefore we can only treat explicitly a limited number of degrees of freedom, which correspond to the largest scales of the system. The influence of the turbulent dynamics from smaller scales onto larger scales has to be treated in a statistical way. How the dynamics on small scales and the dynamics on large scales are interconnected, can be seen by explicitly filtering the equations of fluid dynamics.

---

[10] Floating point operations per second.

3 Filter formalism

Next we present a very general filter formalism, which is useful when dealing with the compressible equations of fluid dynamics. We collect the most important rules[1], which are necessary to filter the compressible equations of fluid dynamics.

3.1 Reynolds filter

In general filtering means splitting some quantity a in a mean value $\langle a\rangle$ generated by the filter procedure and some deviation a' from the mean value. If a filter fulfills the following relations,

$$\langle A+B\rangle = \langle A\rangle + \langle B\rangle, \tag{3.1}$$

$$\langle C\rangle = C, \text{ if } C = \text{const.}, \tag{3.2}$$

$$\langle\langle A\rangle B\rangle = \langle A\rangle\langle B\rangle, \tag{3.3}$$

it is called a Reynolds filter or Reynolds operator. From equation (3.2) and (3.3) we see that for $B = C = const.$

$$\langle\langle A\rangle C\rangle = \langle A\rangle C. \tag{3.4}$$

From this relation (3.4) it follows for $C = 1$

$$\langle\langle A\rangle\rangle = \langle A\rangle. \tag{3.5}$$

From the last equation ((3.5)) and (3.3) we get for $B = \langle D\rangle$

$$\langle\langle A\rangle\langle D\rangle\rangle = \langle A\rangle\langle\langle D\rangle\rangle = \langle A\rangle\langle D\rangle. \tag{3.6}$$

If we split a quantity a in a sum of some kind of mean value $\langle a\rangle$ (computed by a filter that satisfies the Reynolds criteria (3.1)-(3.3)) and some deviations a'

$$a = \langle a\rangle + a' \tag{3.7}$$

it follows from equation (3.5) for the mean of the deviations

$$\langle a'\rangle = \langle a - \langle a\rangle\rangle = \langle a\rangle - \langle\langle a\rangle\rangle = \langle a\rangle - \langle a\rangle = 0. \tag{3.8}$$

---

[1] These rules have already been used implicitely by Canuto (1997); Schmidt et al. (2006a), but our work is the first to summarize them explicitly.

One can show that the so called central moments of this quantity ($\langle a'b' \rangle$, $\langle a'b'c' \rangle$, $\langle a'b'c'd' \rangle$, $\ldots$) can be expressed in terms of the classical moments ($\langle ab \rangle$, $\langle abc \rangle$, $\langle abcd \rangle$, $\ldots$) like[2]

$$\langle a'b' \rangle = \langle ab \rangle - \langle a \rangle \langle b \rangle \tag{3.9}$$

$$\begin{aligned} \langle a'b'c' \rangle = {} & \langle abc \rangle - \langle a \rangle \langle b \rangle \langle c \rangle \\ & - \langle a \rangle \langle b'c' \rangle - \langle b \rangle \langle a'c' \rangle - \langle c \rangle \langle a'b' \rangle \end{aligned} \tag{3.10}$$

$$\begin{aligned} \langle a'b'c'd' \rangle = {} & \langle abcd \rangle - \langle a \rangle \langle b \rangle \langle c \rangle \langle d \rangle \\ & - \langle a \rangle \langle b'c'd' \rangle - \langle b \rangle \langle a'c'd' \rangle - \langle c \rangle \langle a'b'd' \rangle - \langle d \rangle \langle a'b'c' \rangle \\ & - \langle a \rangle \langle b \rangle \langle c'd' \rangle - \langle a \rangle \langle c \rangle \langle b'd' \rangle - \langle a \rangle \langle d \rangle \langle b'c' \rangle \\ & - \langle b \rangle \langle c \rangle \langle a'd' \rangle - \langle b \rangle \langle d \rangle \langle a'c' \rangle - \langle c \rangle \langle d \rangle \langle a'b' \rangle \end{aligned} \tag{3.11}$$

$$\langle a'b'c'd'e' \rangle = \ldots \tag{3.12}$$

3.2 Germano formalism

Germano (1992) postulates that the relations between moments and central moments for non-Reynolds operators[3] are of similar form as for Reynolds operators. Therefore he introduces the so called generalized central moments $\tau(a,b), \tau(a,b,c), \ldots$ for non-Reynolds operators. These should fulfill in analogy to equation (3.9)-(3.12) the following relations[4]

$$\tau(a,b) = \langle ab \rangle - \langle a \rangle \langle b \rangle \tag{3.13}$$

$$\begin{aligned} \tau(a,b,c) = {} & \langle abc \rangle - \langle a \rangle \langle b \rangle \langle c \rangle \\ & - \langle a \rangle \tau(b,c) - \langle b \rangle \tau(a,c) - \langle c \rangle \tau(a,b) \end{aligned} \tag{3.14}$$

$$\begin{aligned} \tau(a,b,c,d) = {} & \langle abcd \rangle - \langle a \rangle \langle b \rangle \langle c \rangle \langle d \rangle \\ & - \langle a \rangle \tau(b,c,d) - \langle b \rangle \tau(a,c,d) \\ & - \langle c \rangle \tau(a,b,d) - \langle d \rangle \tau(a,b,c) \\ & - \langle a \rangle \langle b \rangle \tau(c,d) - \langle a \rangle \langle c \rangle \tau(b,d) - \langle a \rangle \langle d \rangle \tau(b,c) \\ & - \langle b \rangle \langle c \rangle \tau(a,d) - \langle b \rangle \langle d \rangle \tau(a,c) - \langle c \rangle \langle d \rangle \tau(a,b) \end{aligned} \tag{3.15}$$

$$\langle a'b'c'd'e' \rangle = \ldots \tag{3.16}$$

For the generalized central moments the following rules apply:

1. They are symmetric in their arguments

$$\tau(a,b) = \tau(b,a); \tau(a,b,c) = \tau(b,a,c), \ldots \tag{3.17}$$

---

[2] See for example (Monin and Yaglom, 1971).

[3] Non-Reynolds operators do not fulfill 3.8, so their mean of the deviations is unequal zero.

[4] It seems to be very difficult to prove these relations even in case of very simple non-Reynolds operators.

2. The generalized central moment of a constant is zero

$$\tau(a,c) = 0, \tau(a,b,c) = 0, \text{ if } c = \text{const.} \tag{3.18}$$

3. In case of a static (time independent) filter operator it permutes with the time derivative and the chain rule applies

$$\frac{\partial}{\partial t}\tau(a,b) = \tau\left(\frac{\partial}{\partial t}a, b\right) + \tau\left(a, \frac{\partial}{\partial t}b\right) \tag{3.19}$$

4. If the filter operator is isotropic (independent of position in space) then it applies

$$\frac{\partial}{\partial x_i}\tau(a,b) = \tau\left(\frac{\partial}{\partial x_i}a, b\right) + \tau\left(a, \frac{\partial}{\partial x_i}b\right) \tag{3.20}$$

5. Additionally the following relation can be proved

$$\tau(a, Cb) = C \cdot \tau(a,b), \text{ if } C = \text{const.} \tag{3.21}$$

$$\tau(a, b+c) = \tau(a,b) + \tau(a,c) \tag{3.22}$$

$$\tau(a, bc) = \tau(a,b,c) + \langle b\rangle\tau(a,c) + \langle c\rangle\tau(a,b) \tag{3.23}$$

3.3 Favre-Germano formalism

In the case of compressible fluid dynamics, the moments appearing in the filtered equations are one order higher than in non-compressible fluid dynamics (eg. $\langle \rho u_i u_j\rangle$ instead of $\langle u_i u_j\rangle$). If we would adopt the Germano relations (3.13) to (3.16) in this case, we would get many terms which are difficult to interpret physically. But if we use density weighted quantities[5] similar to Favre (1969) and develop relations in analogy to the Germano relations for these density weighted quantities, we can write the filtered compressible equations of fluid dynamics in a much simpler way (Canuto, 1997; Schmidt et al., 2006a).

We define density weighted quantities according to Favre like

$$\langle \rho a\rangle = \langle \rho\rangle \hat{a} \Rightarrow \hat{a} = \frac{\langle \rho a\rangle}{\langle \rho\rangle}. \tag{3.24}$$

In analogy to Germano we postulate the following relations:

$$\hat{\tau}(a,b) = \langle \rho ab\rangle - \langle \rho\rangle \hat{a}\hat{b} \tag{3.25}$$

$$\begin{aligned}\hat{\tau}(a,b,c) = {} & \langle \rho abc\rangle - \langle \rho\rangle \hat{a}\hat{b}\hat{c} \\ & - \hat{a}\hat{\tau}(b,c) - \hat{b}\hat{\tau}(a,c) - \hat{c}\hat{\tau}(a,b)\end{aligned} \tag{3.26}$$

$$\hat{\tau}(a,b,c,d) = \ldots \tag{3.27}$$

---

[5] For a modern review of this procedure see Veynante and Vervisch (2002).

For the quantities $\hat{\tau}(\ldots)$ the same rules apply as for the generalized central moments $\tau(\ldots)$ introduced by Germano:

1. $\hat{\tau}(a,b) = \hat{\tau}(b,a); \hat{\tau}(a,b,c) = \hat{\tau}(b,a,c), \ldots$
2. $\hat{\tau}(a,c) = 0, \hat{\tau}(a,b,c) = 0$, if $c = \text{const.}$
3. $\frac{\partial}{\partial t}\hat{\tau}(a,b) = \hat{\tau}\big(\frac{\partial}{\partial t}a, b\big) + \hat{\tau}\big(a, \frac{\partial}{\partial t}b\big)$ for static filter.
4. $\frac{\partial}{\partial x_i}\hat{\tau}(a,b) = \hat{\tau}\Big(\frac{\partial}{\partial x_i}a, b\Big) + \hat{\tau}\Big(a, \frac{\partial}{\partial x_i}b\Big)$ for isotropic filter.
5. a) $\hat{\tau}(a, Cb) = C \cdot \hat{\tau}(a,b)$, if $C = \text{const.}$
   b) $\hat{\tau}(a, b+c) = \hat{\tau}(a,b) + \hat{\tau}(a,c)$
   c) $\hat{\tau}(a, bc) = \hat{\tau}(a,b,c) + \langle b\rangle\hat{\tau}(a,c) + \langle c\rangle\hat{\tau}(a,b)$

If we compare the Favre relations to the Germano relations we see:

$$\text{Germano: } \langle\rho a\rangle = \langle\rho\rangle\langle a\rangle + \tau(\rho, a) \tag{3.28}$$

$$\text{Favre: } \langle\rho a\rangle = \langle\rho\rangle\hat{a} \tag{3.29}$$

$$\Rightarrow \hat{a} = \langle a\rangle + \frac{\tau(\rho, a)}{\langle\rho\rangle} \tag{3.30}$$

$$\Rightarrow \hat{a} = \langle a\rangle, \text{ if } \rho = \text{const.} \tag{3.31}$$

This means in the case of a constant density, the formalism with Favre density weighted quantities is equivalent to the Germano formalism. [6]

3.4 Explicit filtering

The rules for filtering described in the last sections do not depend on an explicit form of a filter procedure. However we now want to introduce a commonly used representation of a filter procedure, namely the convolution filter. Using a convolution filter the mean value $\langle a\rangle$ of some quantity $a(x)$ is defined as

$$\langle a(x)\rangle = \int_{-\infty}^{\infty} G(x - x')a(x')dx', \tag{3.32}$$

where $G(x - x')$ is called the convolution kernel, and is associated with some cutoff length l_Δ. The deviation of the mean value is then defined as

$$a' = a(x) - \langle a(x)\rangle = a(x) - \int_{-\infty}^{\infty} G(x - x')a(x')dx'. \tag{3.33}$$

---

[6] This can also be proved for the higher moments.

The importance of the convolution filter stems from the fact that it can be used to generalise discrete operators, e.g. we can write the well-known second-order central difference formula for the derivative of a continuous variable like[7]

$$\begin{aligned}\frac{a(x+h)-a(x-h)}{2h} &= \frac{d}{dx}\left(\frac{1}{2h}\int\limits_{x-h}^{x+h} a(x')dx'\right) \\ &= \frac{d}{dx}\int\limits_{-\infty}^{\infty} G(x-x')a(x')dx' \\ &= \frac{d}{dx}\langle a\rangle\end{aligned}$$

with

$$G(x-x') = \begin{cases} \frac{1}{2h} & \text{if } |x-x'| \leq h \\ 0 & \text{otherwise} \end{cases} . \tag{3.34}$$

The convolution kernel (3.34) is also called a box or top-hat filter and is most often used for performing explicit spatial scale separation.

---

[7] See Rogallo and Moin (1984).

4 Favre-filtered equations of fluid dynamics

4.1 Basic equations

Using the Favre-Germano formalism developed in 3.3 to filter the equations of compressible selfgravitating fluid dynamics (2.1)-(2.3) leads to

$$\frac{\partial}{\partial t}\langle\rho\rangle + \frac{\partial}{\partial r_j}\hat{v}_j\langle\rho\rangle = 0 \tag{4.1}$$

$$\frac{\partial}{\partial t}\langle\rho\rangle\hat{v}_i + \frac{\partial}{\partial r_j}\hat{v}_j\langle\rho\rangle\hat{v}_i = -\frac{\partial}{\partial r_i}\langle p\rangle + \frac{\partial}{\partial r_j}\langle\sigma'_{ij}\rangle + \langle\rho\rangle\hat{g}_i - \frac{\partial}{\partial r_j}\hat{\tau}(v_i, v_j) \tag{4.2}$$

$$\begin{aligned}\frac{\partial}{\partial t}\langle\rho\rangle\hat{e} + \frac{\partial}{\partial r_j}\langle\rho\rangle\hat{v}_j\hat{e} = &-\frac{\partial}{\partial r_j}\langle v_j p\rangle + \frac{\partial}{\partial r_j}\langle v_i\sigma_{ij}\rangle + \langle\rho\rangle\hat{v}_i\hat{g}_i \\ &+ \hat{\tau}(v_i, g_i) - \frac{\partial}{\partial r_j}\hat{\tau}(v_j, e)\end{aligned} \tag{4.3}$$

with

$$\hat{e} = \hat{e}_{int} + \frac{1}{2}\hat{v}_i\hat{v}_i + \frac{1}{2}\frac{\hat{\tau}(v_i, v_i)}{\langle\rho\rangle} \tag{4.4}$$

and

$$\hat{\tau}(v_j, e) = \hat{\tau}(v_j, e_{int}) + \frac{1}{2}\hat{\tau}(v_j, v_i, v_i) + \hat{v}_i\hat{\tau}(v_j, v_i) \tag{4.5}$$

Filtering the equation for the kinetic energy and the internal energy alone we get:

$$\begin{aligned}\frac{\partial}{\partial t}\langle\rho\rangle\hat{e}_k + \frac{\partial}{\partial r_j}\hat{v}_j\langle\rho\rangle\hat{e}_k) = &-\langle v_i\frac{\partial}{\partial r_i}p\rangle + \langle v_i\frac{\partial}{\partial r_j}\sigma'_{ij}\rangle + \langle\rho\rangle\hat{v}_i\hat{g}_i \\ &+ \hat{\tau}(v_i, g_i) - \frac{\partial}{\partial r_j}\hat{\tau}(v_j, e_k)\end{aligned} \tag{4.6}$$

$$\frac{\partial}{\partial t}\langle\rho\rangle\hat{e}_{int} + \frac{\partial}{\partial r_j}\hat{v}_j\langle\rho\rangle\hat{e}_{int} = -\langle p\frac{\partial}{\partial r_j}v_j\rangle + \langle\sigma'_{ij}\frac{\partial}{\partial r_j}v_i\rangle - \frac{\partial}{\partial r_j}\hat{\tau}(v_j, e_{int}) \tag{4.7}$$

with

$$\hat{e}_k = \frac{1}{2}\hat{v}_i\hat{v}_i + \frac{1}{2}\frac{\hat{\tau}(v_i, v_i)}{\langle\rho\rangle} \tag{4.8}$$

and

$$\hat{\tau}(v_j, e_k) = \frac{1}{2}\hat{\tau}(v_j, v_i, v_i) + \hat{v}_i\hat{\tau}(v_j, v_i) \tag{4.9}$$

4.2 Resolved energy and turbulent energy equations

Multiplying the filtered equation for the momentum (4.2) with the Favre-filtered velocity $\hat{v}_i$ yields the balance equation for the resolved kinetic energy:

$$\begin{aligned}\frac{\partial}{\partial t}\langle\rho\rangle\frac{1}{2}\hat{v}_i\hat{v}_i + \frac{\partial}{\partial r_j}\hat{v}_j\langle\rho\rangle\frac{1}{2}\hat{v}_i\hat{v}_i =& - \hat{v}_i\frac{\partial}{\partial r_i}\langle p\rangle + \hat{v}_i\frac{\partial}{\partial r_j}\langle\sigma'_{ij}\rangle + \langle\rho\rangle\hat{v}_i\hat{g}_i \\ & - \hat{v}_i\frac{\partial}{\partial r_j}\hat{\tau}(v_i, v_j)\end{aligned} \tag{4.10}$$

Adding the equation for the resolved kinetic energy (4.10) to the equation for the filtered internal energy (4.7) one gets the equation for the total resolved energy $e_{res} = \hat{e}_{int} + \frac{1}{2}\hat{v}_i\hat{v}_i$:

$$\begin{aligned}\frac{\partial}{\partial t}\langle\rho\rangle e_{res} + \frac{\partial}{\partial r_j}\hat{v}_j\langle\rho\rangle e_{res} =& - \hat{v}_i\frac{\partial}{\partial r_i}\langle p\rangle + \hat{v}_i\frac{\partial}{\partial r_j}\langle\sigma'_{ij}\rangle + \langle\rho\rangle\hat{v}_i\hat{g}_i \\ & - \langle p\frac{\partial}{\partial r_i}v_i\rangle + \langle\sigma'_{ij}\frac{\partial}{\partial r_j}v_i\rangle - \hat{v}_i\frac{\partial}{\partial r_j}\hat{\tau}(v_i, v_j) \\ & - \frac{\partial}{\partial r_j}\hat{\tau}(v_j, e_{int})\end{aligned} \tag{4.11}$$

The arising four terms $\langle p\frac{\partial}{\partial r_i}v_i\rangle, \langle\sigma'_{ij}\frac{\partial}{\partial r_j}v_i\rangle, \hat{\tau}(v_i, v_j), \hat{\tau}(v_j, e_{int})$ in the total resolved energy represent the coupling of the unresolved fluctuations to the filtered resolved flow. We could now try to find equations based on quantities of the resolved flow, to model each of these terms independent of each other. Nevertheless we will see that the first three of these four terms can be connected by an equation for another quantity, called the turbulent energy ε_t. From solving the equation for this quantity we get the three terms $\langle p\frac{\partial}{\partial r_i}v_i\rangle, \langle\sigma'_{ij}\frac{\partial}{\partial r_j}v_i\rangle, \hat{\tau}(v_i, v_j)$. Only the fourth term $\hat{\tau}(v_j, e_{int})$ is not connected with the turbulent energy and has to be modeled separately.

We get the balance equation for the turbulent energy[1] $\varepsilon_t = \langle\rho\rangle e_t = \frac{1}{2}\hat{\tau}(v_i, v_i)$ by subtracting the balance equation for the resolved kinetic energy (4.10) from the balance equation of the filtered kinetic energy (4.6) :

---

[1] Interpreting the quantity $\hat{\tau}(v_i, v_i) = \hat{\tau}_{ii}$ as an energy is only possible, if $\hat{\tau}_{ii} \geq 0$. This is only guaranteed, if the filter convolution kernel is a semi-positive function in position space (Vreman et al., 1994; Sagaut, 2006).

$$\begin{aligned}\frac{\partial}{\partial t}\langle\rho\rangle e_t + \frac{\partial}{\partial r_j}\hat{v}_j\langle\rho\rangle e_t = &- \left[\langle v_i\frac{\partial}{\partial r_i}p\rangle - \hat{v}_i\frac{\partial}{\partial r_i}\langle p\rangle\right]\\ &+ \left[\langle v_i\frac{\partial}{\partial r_j}\sigma'_{ij}\rangle - \hat{v}_i\frac{\partial}{\partial r_j}\langle\sigma'_{ij}\rangle\right]\\ &+ \hat{\tau}(v_i,g_i) - \frac{1}{2}\frac{\partial}{\partial r_j}\hat{\tau}(v_j,v_i,v_i) - \hat{\tau}(v_j,v_i)\frac{\partial}{\partial r_j}\hat{v}_i\end{aligned} \tag{4.12}$$

For a better comparison with Schmidt et al. (2006a) we will transform the following terms like

$$\langle v_i\frac{\partial}{\partial r_i}p\rangle = \frac{\partial}{\partial r_i}\langle v_i p\rangle - \langle p\frac{\partial}{\partial r_i}v_i\rangle \tag{4.13}$$

$$\hat{v}_i\frac{\partial}{\partial r_i}\langle p\rangle = \frac{\partial}{\partial r_i}\hat{v}_i\langle p\rangle - \langle p\rangle\frac{\partial}{\partial r_i}\hat{v}_i \tag{4.14}$$

$$\langle v_i\frac{\partial}{\partial r_j}\sigma'_{ij}\rangle = \frac{\partial}{\partial r_j}\langle v_i\sigma'_{ij}\rangle - \langle\sigma'_{ij}\frac{\partial}{\partial r_j}v_i\rangle \tag{4.15}$$

$$\hat{v}_i\frac{\partial}{\partial r_j}\langle\sigma'_{ij}\rangle = \frac{\partial}{\partial r_j}\hat{v}_i\langle\sigma'_{ij}\rangle - \langle\sigma'_{ij}\rangle\frac{\partial}{\partial r_j}\hat{v}_i \tag{4.16}$$

and rewrite the balance equation for the turbulent energy:

$$\begin{aligned}\frac{\partial}{\partial t}\langle\rho\rangle e_t + \frac{\partial}{\partial r_j}\hat{v}_j\langle\rho\rangle e_t = &- \frac{\partial}{\partial r_j}\left[\frac{1}{2}\hat{\tau}(v_j,v_i,v_i) + \langle v_i p\rangle - \hat{v}_i\langle p\rangle - \langle v_i\sigma'_{ij}\rangle + \hat{v}_i\langle\sigma'_{ij}\rangle\right]\\ &- \left[\langle p\rangle\frac{\partial}{\partial r_i}\hat{v}_i - \langle p\frac{\partial}{\partial x_i}v_i\rangle\right] + \left[\langle\sigma'_{ij}\rangle\frac{\partial}{\partial r_j}\hat{v}_i - \langle\sigma'_{ij}\frac{\partial}{\partial r_j}v_i\rangle\right]\\ &+ \hat{\tau}(v_i,g_i) - \hat{\tau}(v_j,v_i)\frac{\partial}{\partial x_j}\hat{v}_i\end{aligned} \tag{4.17}$$

If we introduce now in analogy to Schmidt et al. (2006a) the following definitions

$$-\mu = \langle v_i p\rangle - \hat{v}_i\langle p\rangle \tag{4.18}$$

$$-\kappa = \langle v_i\sigma'_{ij}\rangle - \hat{v}_i\langle\sigma'_{ij}\rangle \tag{4.19}$$

$$\mathbb{D} = -\frac{\partial}{\partial r_j}\left[\frac{1}{2}\hat{\tau}(v_j,v_i,v_i) - \mu + \kappa\right] \tag{4.20}$$

$$\langle\rho\rangle\lambda = \left[\langle p\rangle\frac{\partial}{\partial r_i}\hat{v}_i - \langle p\frac{\partial}{\partial r_i}v_i\rangle\right] \tag{4.21}$$

$$\langle\rho\rangle\epsilon = -\left[\langle\sigma'_{ij}\rangle\frac{\partial}{\partial r_j}\hat{v}_i - \langle\sigma'_{ij}\frac{\partial}{\partial r_j}v_i\rangle\right] \tag{4.22}$$

$$\Gamma = \hat{\tau}(v_i,g_i) \tag{4.23}$$

we can write the balance equation for the turbulence energy like

$$\frac{\partial}{\partial t}\langle\rho\rangle e_t + \frac{\partial}{\partial r_j}\hat{v}_j\langle\rho\rangle e_t = \mathbb{D} + \Gamma - \langle\rho\rangle(\lambda+\epsilon) - \hat{\tau}(v_j, v_i)\frac{\partial}{\partial r_j}\hat{v}_i. \tag{4.24}$$

With the help of equations (4.13) to (4.16) and the definitions (4.21) and (4.22) we can also rewrite the equation (4.11) for the total resolved energy:

$$\begin{aligned}\frac{\partial}{\partial t}\langle\rho\rangle e_{res} + \frac{\partial}{\partial r_j}\hat{v}_j\langle\rho\rangle e_{res} =& -\frac{\partial}{\partial r_i}\hat{v}_i\langle p\rangle + \frac{\partial}{\partial r_j}\hat{v}_i\langle\sigma'_{ij}\rangle + \langle\rho\rangle\hat{v}_i\hat{g}_i \\ &+ \langle\rho\rangle(\lambda+\epsilon) - \hat{v}_i\frac{\partial}{\partial r_j}\hat{\tau}(v_i, v_j) - \frac{\partial}{\partial r_j}\hat{\tau}(v_j, e_{int}).\end{aligned} \tag{4.25}$$

4.3 Summary

The last two equations (4.24) and (4.25) together with equation (4.1) and (4.2) (and additionally the Poisson equation for the gravity term and the equation of state) form a complete system of partial differential equations for fluid dynamics

$$\frac{\partial}{\partial t}\langle\rho\rangle + \frac{\partial}{\partial r_j}\hat{v}_j\langle\rho\rangle = 0, \tag{4.26}$$

$$\frac{\partial}{\partial t}\langle\rho\rangle\hat{v}_i + \frac{\partial}{\partial r_j}\hat{v}_j\langle\rho\rangle\hat{v}_i = -\frac{\partial}{\partial r_i}\langle p\rangle + \frac{\partial}{\partial r_j}\langle\sigma'_{ij}\rangle + \langle\rho\rangle\hat{g}_i - \frac{\partial}{\partial r_j}\hat{\tau}(v_i, v_j), \tag{4.27}$$

$$\begin{aligned}\frac{\partial}{\partial t}\langle\rho\rangle e_{res} + \frac{\partial}{\partial r_j}\hat{v}_j\langle\rho\rangle e_{res} =& -\frac{\partial}{\partial r_i}\hat{v}_i\langle p\rangle + \frac{\partial}{\partial r_j}\hat{v}_i\langle\sigma'_{ij}\rangle + \langle\rho\rangle\hat{v}_i\hat{g}_i \\ &+ \langle\rho\rangle(\lambda+\epsilon) - \hat{v}_i\frac{\partial}{\partial r_j}\hat{\tau}(v_i, v_j) - \frac{\partial}{\partial r_j}\hat{\tau}(v_j, e_{int}),\end{aligned} \tag{4.28}$$

$$\frac{\partial}{\partial t}\langle\rho\rangle e_t + \frac{\partial}{\partial r_j}\hat{v}_j\langle\rho\rangle e_t = \mathbb{D} + \Gamma - \langle\rho\rangle(\lambda+\epsilon) - \hat{\tau}(v_j, v_i)\frac{\partial}{\partial r_j}\hat{v}_i, \tag{4.29}$$

where it is often useful to split the equation for resolved energy into an equation for the resolved kinetic energy and internal energy respectively

$$\begin{aligned}\frac{\partial}{\partial t}\langle\rho\rangle\hat{e}_k + \frac{\partial}{\partial r_j}\hat{v}_j\langle\rho\rangle\hat{e}_k) =& -\hat{v}_i\frac{\partial}{\partial r_i}\langle p\rangle + \hat{v}_i\frac{\partial}{\partial r_j}\langle\sigma'_{ij}\rangle + \langle\rho\rangle\hat{v}_i\hat{g}_i \\ &- \hat{v}_i\frac{\partial}{\partial r_j}\hat{\tau}(v_i, v_j),\end{aligned} \tag{4.30}$$

$$\begin{aligned}\frac{\partial}{\partial t}\langle\rho\rangle\hat{e}_{int} + \frac{\partial}{\partial r_j}\hat{v}_j\langle\rho\rangle\hat{e}_{int} =& -\langle p\rangle\frac{\partial}{\partial r_j}\hat{v}_j + \langle\sigma'_{ij}\rangle\frac{\partial}{\partial r_j}\hat{v}_i + \langle\rho\rangle(\lambda+\epsilon) \\ &- \frac{\partial}{\partial r_j}\hat{\tau}(v_j, e_{int}).\end{aligned} \tag{4.31}$$

The explicit forms of the quantities $\mathbb{D}, \lambda, \epsilon, \Gamma$ and $\hat{\tau}(v_i, v_j)$ are unknown and have to be modeled in terms of the turbulence energy e_t. The term $\hat{\tau}(v_j, e_{int})$ has to be modeled independently of e_t. The models for all these terms represent our turbulence or subgrid model.

5 LES and SGS model

5.1 The concept of LES

The idea behind large eddy simulations (LES) is to solve the filtered equations of fluid dynamics (FE) (4.26) - (4.29) instead of the unfiltered ones (UE) (2.1)-(2.3). There are two reasons for this:

1. The FE represent a system with a smaller number of resolved degrees of freedom (DOF) compared with the UE. This is a necessary restriction, because the numerical discretization itself acts as a filter[1] and limits the number of DOF which we can resolve in a high Reynolds number flow. In effect this leads to the problem that the outcome of a simulation of turbulence using the UE depends on the numerical scheme used. If instead we solve the FE using a certain subgrid model with a characteristic cutoff length higher than the numerical cutoff length, the outcome of the turbulence simulation is only dependent on our subgrid model and not on the numerical scheme used (Mason and Brown, 1999). From this point of view, we should call a turbulence model simply a filter model.
2. Using the numerical cutoff as an explicit filter in an energy conserving numerical scheme converts kinetic into internal energy. But the back reaction of the internal energy on the kinetic energy can only be via the pressure term, which is presumably not right. With an explicit turbulence model, we can model the backscattering of small scale fluctuations on the resolved kinetic energy in a much better way (Schmidt, 2004). To model the backscattering we have to know explicitly the amount of energy on the scales between the cutoff scale and the Kolmogorov scale. This is what we call subgrid energy or turbulent energy and that is why the term subgrid scale (SGS) model is appropriate for the unknown terms in the FE.

Unfortunately there is a substantial variety of SGS models in the literature and no agreement on a standard model. An extensive overview of SGS models for incompressible flows can be found for example in the book by Sagaut (2006). There are fewer models explicitly for compressible flows. A simple one, that was first introduced by Schmidt (2004); Schmidt et al. (2006b), will be described in the next sections. This *Schmidt model*[2], together with some corrections due to Sarkar (1992), which will be outlined later, is the model we use to describe the influence of turbulence on the resolved scales in our work.

---

[1] See section 3.4.

5.2 Schmidt model

As we interpret the trace of the generalized central moment of the velocity $\langle\tau\rangle_{ij}$ as a turbulent energy, we can define a velocity of the turbulent motions[3] $q = \sqrt{2e_t}$, which is used as characteristic velocity of the subgrid terms in the Schmidt model. As a characteristic length scale the size of one grid cell l_Δ is used [4].

The Schmidt model neglects the convective flux term $\hat{\tau}(v_j, e_{int})$ and the gravitational effects Γ on the subgrid scales. The models for the other terms are described in the following sections.

5.2.1 Transport term $\mathbb{D}$

The transport or diffusion term is modeled by a gradient hypothesis, by stating that the non-linear term is proportional to the turbulent velocity q^2 gradient (Kolmogorov-Prandl relation, see Sagaut (2006, p.97))

$$\mathbb{D} = \frac{\partial}{\partial r_i} C_{\mathbb{D}} \langle\rho\rangle l_\Delta q^2 \frac{\partial}{\partial r_i} q. \tag{5.1}$$

The constant $C_{\mathbb{D}}$ is calibrated to $C_{\mathbb{D}} \approx 0.4 = \frac{2}{5}$ by numerical experiments (Schmidt et al., 2006a).

5.2.2 Pressure dilatation λ

For λ an estimate is used that is presumably only valid in the subsonic (nearly incompressible) regime:

$$\lambda = C_\lambda q^2 \frac{\partial}{\partial r_i} \hat{v}_i. \tag{5.2}$$

The constant $C_\lambda = -\frac{1}{5}$ as found by numerical experiments (Schmidt et al., 2006a).

---

[2] Actually the original implementation of the SGS model proposed by Schmidt et al. (2006b) had severe problems with energy conservation and was notoriously difficult to implement in an AMR code. The version of the *Schmidt model* described in this work is a simplified version, but it conserves energy and proved to be sufficient for our work.

[3] This is based on an analogy to kinetic energy in the sense, that $\frac{1}{2}\rho q^2 = \rho e_t$.

[4] As mentioned, the implicit cutoff of our subgrid = filter model should be greater than the numerical cutoff, so one might object, that l_Δ is too small for that. But every term in the subgrid model is multiplied by some dimensionless constant, which is set to a value high enough to make numerical cutoff effects insignificant.

5.2.3 Turbulent dissipation ϵ

The turbulent dissipation accounts for effects of viscosity on subgrid scales. These effects convert turbulent energy to internal energy even if, on the larger scales, the effect of viscosity can be neglected. The most simple expression which can be built from the characteristic turbulent velocity and length scale for the dissipation is

$$\epsilon = C_\epsilon \frac{q^3}{l_\Delta}. \tag{5.3}$$

For our simulations we will set $C_\epsilon = 0.5$.[5]

5.2.4 Turbulence production tensor $\hat{\tau}(v_i, v_j)$

The turbulence production term is symmetric in its arguments and can therefore be written as follows

$$\hat{\tau}(v_i, v_j) = \hat{\tau}_{ij} = \frac{1}{2}(\hat{\tau}_{ij} + \hat{\tau}_{ij}) = \frac{1}{2}(\hat{\tau}_{ij} + \hat{\tau}_{ji}). \tag{5.4}$$

By subtracting the trace of this tensor

$$\hat{\tau}_{ij} = \frac{1}{2}(\hat{\tau}_{ij} + \hat{\tau}_{ji}) - \frac{1}{n}\delta_{ij}\hat{\tau}_{kk} + \frac{1}{3}\delta_{ij}\hat{\tau}_{kk} \tag{5.5}$$

and recognizing that $\hat{\tau}_{kk} = \langle\rho\rangle q^2$ we can split the tensor in a symmetric, tracefree part $\hat{\tau}^*_{ij} = \frac{1}{2}(\hat{\tau}_{ij} + \hat{\tau}_{ji}) - \frac{1}{3}\delta_{ij}\hat{\tau}_{kk}$ and the trace

$$\hat{\tau}_{ij} = \hat{\tau}^*_{ij} + \frac{1}{3}\delta_{ij}\langle\rho\rangle q^2 = \hat{\tau}^*_{ij} + p_t, \tag{5.6}$$

where the trace is commonly called turbulent pressure p_t.

A model for $\hat{\tau}^*_{ij}$ is based on the turbulent viscosity hypothesis. There it is assumed, that $\hat{\tau}^*_{ij}$ is of the same form like S^*_{ij} for a newtonian fluid, so

$$\hat{\tau}^*_{ij} = -2\eta_t S^*_{ij} \tag{5.7}$$

with a turbulent dynamic viscosity $\eta_t = \langle\rho\rangle\nu_t = \langle\rho\rangle C_\nu l_\Delta q$ and

$$S^*_{ij} = \frac{1}{2}\left(\frac{\partial}{\partial r_j}\hat{v}_i + \frac{\partial}{\partial r_i}\hat{v}_j\right) - \frac{1}{3}\delta_{ij}\frac{\partial}{\partial r_k}\hat{v}. \tag{5.8}$$

The turbulence production term is therefore modeled as

$$\hat{\tau}(v_i, v_j) = -2\langle\rho\rangle C_\nu l_\Delta q S^*_{ij} + \frac{1}{3}\delta_{ij}\langle\rho\rangle q^2. \tag{5.9}$$

---

[5] Suggested by W. Schmidt, personal communication.

It should be noted, that in general the old idea of turbulent viscosity (which was first forumlated by Boussinesq (1877)) is incorrect. As Pope (2000) shows, it is only true when the ratio of production of turbulent energy $\Sigma^* = \hat{\tau}^*_{ij} \frac{\partial v_i}{\partial r_j}$ to dissipation ϵ is $\frac{\Sigma^*}{\epsilon} \sim 1$. If this ratio is much greater or much smaller than one the turbulent viscosity hypothesis is incorrect.

Nevertheless since it is the most common idea used to model the turbulent production tensor it is also used in the Schmidt model. Setting the constant $C_\nu = 0.05$ seems to be a rational choice (Schmidt et al., 2006a).

5.2.5 Summary of the Schmidt model

Using the Schmidt model, the FE form the following system of equations

$$\frac{\partial}{\partial t}\langle\rho\rangle + \frac{\partial}{\partial r_j}\hat{v}_j\langle\rho\rangle = 0, \tag{5.10}$$

$$\frac{\partial}{\partial t}\langle\rho\rangle\hat{v}_i + \frac{\partial}{\partial r_j}\hat{v}_j\langle\rho\rangle\hat{v}_i = -\frac{\partial}{\partial r_i}(\langle p\rangle + p_t) + \langle\rho\rangle\hat{g}_i - \frac{\partial}{\partial r_j}\hat{\tau}^*_{ij}, \tag{5.11}$$

$$\begin{aligned}\frac{\partial}{\partial t}\langle\rho\rangle e_{res} + \frac{\partial}{\partial r_j}\hat{v}_j\langle\rho\rangle e_{res} = &-\frac{\partial}{\partial r_i}\hat{v}_i(\langle p\rangle + p_t) + \langle\rho\rangle\hat{v}_i\hat{g}_i \\ &+ \langle\rho\rangle(\lambda + \epsilon) - \hat{v}_i\frac{\partial}{\partial r_j}\hat{\tau}^*(v_i, v_j),)\end{aligned} \tag{5.12}$$

$$\frac{\partial}{\partial t}\langle\rho\rangle e_t + \frac{\partial}{\partial r_j}\hat{v}_j\langle\rho\rangle e_t = \mathbb{D} - \langle\rho\rangle(\lambda + \epsilon) - \hat{\tau}^*(v_j, v_i)\frac{\partial}{\partial r_j}\hat{v}_i - p_t\frac{\partial}{\partial r_i}\hat{v}_i. \tag{5.13}$$

Again it is often useful to split the equation for resolved energy into an equation for the resolved kinetic energy and internal energy respectively

$$\frac{\partial}{\partial t}\langle\rho\rangle\hat{e}_k + \frac{\partial}{\partial r_j}\hat{v}_j\langle\rho\rangle\hat{e}_k) = -\hat{v}_i\frac{\partial}{\partial r_i}(\langle p\rangle + p_t) + \langle\rho\rangle\hat{v}_i\hat{g}_i - \hat{v}_i\frac{\partial}{\partial r_j}\hat{\tau}^*(v_i, v_j), \tag{5.14}$$

$$\frac{\partial}{\partial t}\langle\rho\rangle\hat{e}_{int} + \frac{\partial}{\partial r_j}\hat{v}_j\langle\rho\rangle\hat{e}_{int} = -(\langle p\rangle + p_t)\frac{\partial}{\partial r_j}\hat{v}_j + \langle\rho\rangle(\lambda + \epsilon). \tag{5.15}$$

5.3 Impact of the Schmidt SGS on the fluid equations

5.3.1 General observations

In this section we want to investigate the influence of the Schmidt model on the equations of fluid dynamics. This can be done most easily in a graphical way.

One can see in figure 5.1 the energy transfer between potential, kinetic, and internal energy for the UE. We see that it is possible to convert potential energy

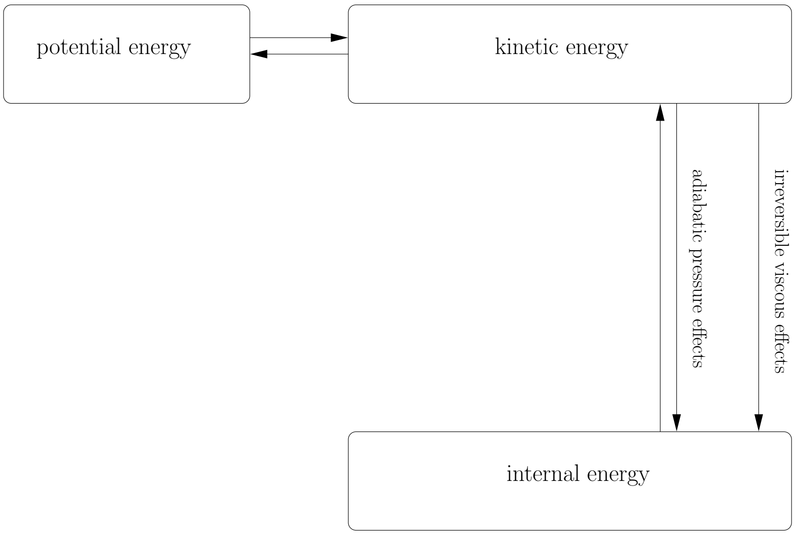

Figure 5.1: Energy transfer in the unfiltered equations of fluid dynamics.

into kinetic energy and vice versa, and also kinetic energy into internal energy and vice versa via adiabatic pressure effects. On the other side, irreversible changes of state due to viscous effects can only lead to an increase of internal energy and not(!) vice versa.

In figure 5.2 the energy transfer for the FE with the Schmidt model is depicted in the same schematical way. We see that the kinetic energy is now split into two parts: the filtered kinetic energy on resolved scales and the turbulent energy on unresolved scales. From this picture it becomes clear that the turbulent energy is converted to internal energy by the same processes as the filtered kinetic energy. Also it could be converted to potential energy[6], but as already mentioned, this effect is neglected in the Schmidt model and therefore not depicted here, as well as the effects due to the convective flux term.

One very important assumption that has not yet been discussed, but is also depicted in figure 5.2, is that conversion of resolved kinetic energy into internal energy due to viscous effects is neglected. Basically all SGS models that make use of the turbulent viscosity hypothesis, and therefore also the Schmidt model, assume that for high Reynolds numbers the turbulent viscosity is much greater than the real viscosity. Why this assumption can be made will be explained in section 5.3.2.

The last conclusion that can be drawn from this pictures is that certain quantities are related to the cutoff scale (Σ^*, p_t) and others are related to the dissipation

---

[6] Drawing the analogy from the conversion of kinetic into internal energy one might ask if there could be something like irreversible conversion of potential energy into kinetic energy or perhaps vice versa. But from general relativity we know that there is no gravity, there is only curvature of space time. It seems very strange to imagine something like irreversible curvature of space time.

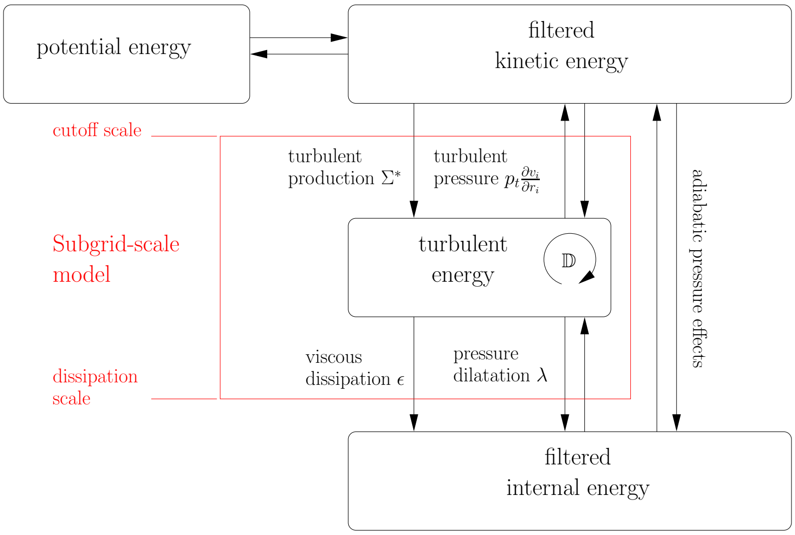
potential energy
filtered
kinetic energy
cutoff scale
turbulent
production Σ^*
turbulent
pressure $p_t\frac{\partial v_i}{\partial r_i}$
adiabatic pressure effects
Subgrid-scale
model
turbulent
energy
$\mathbb{D}$
viscous
dissipation ϵ
pressure
dilatation λ
dissipation
scale
filtered
internal energy

Figure 5.2: Energy transfer in the filtered equations of fluid dynamics with Schmidt SGS.

scale (ϵ,λ). Nevertheless we find that the turbulent dissipation ϵ in the Schmidt model (and also in most other SGS models) is modeled depending on the cutoff scale l_Δ, although it should ultimately only depend on the dissipation scale. As we shall see later this is a point of major concern in the development of a SGS model for an adaptive grid code.

5.3.2 Dimensional analysis

In complete analogy to the UE[7] we can do a dimensionless analysis for the FE with the Schmidt model.

Momentum equation

Introducing the dimensionless quantities

$$e_t^* = \frac{e_t}{q_0^2},\ p_t^* = \frac{p_t}{\rho_0 q_0^2},\ \tau_{ij}^{**} = \frac{\tau_{ij}}{\eta v_0/l_0} = \frac{\tau_{ij}}{\rho_0 q_0 v_0} \tag{5.16}$$

the momentum equation can be written as

$$\frac{l_0}{t_0 v_0}\frac{\partial}{\partial t^*}\langle\rho^*\rangle\hat{v}_i^* + \frac{\partial}{\partial r_j^*}\hat{v}_j^*\langle\rho^*\rangle\hat{v}_i^* = +\frac{\rho_0 g_0 l_0}{\rho_0 v_0^2}\langle\rho^*\rangle\hat{g^*}_i - \frac{p_0}{\rho_0 v_0^2}\frac{\partial}{\partial r_i^*}\langle p^*\rangle - \frac{q_0^2}{v_0^2}\frac{\partial}{\partial r_i^*}p_t \tag{5.17}$$

$$+\frac{\eta_0}{\rho_0 l_0 v_0}\frac{\partial}{\partial r_j^*}\langle\sigma_{ij}'^{*}\rangle - \frac{q_0}{v_0}\frac{\partial}{\partial r_j^*}\hat{\tau}_{ij}^{**} \tag{5.18}$$

---

[7] See appendix A.

From this we can estimate, that the turbulent pressure will become important, when

$$\frac{q_0^2}{v_0^2} \geq \frac{p_0}{\rho_0 v_0^2} \Rightarrow \frac{q_0^2}{p_0/\rho_0} \geq 1 \tag{5.19}$$

If we now introduce the turbulent Mach number

$$M_t = \frac{q_0}{c_s} \tag{5.20}$$

and use $\frac{p_0}{\rho_0} = \frac{c_s^2}{\gamma}$ we see that the turbulent pressure will dominate over the thermal pressure, if

$$M_t^2 \geq \gamma. \tag{5.21}$$

The turbulence production tensor $\hat{\tau}^*_{ij}$ becomes important compared to the stress tensor, if

$$\rho_0 q_0 l_0 \geq \eta_0. \tag{5.22}$$

So we see that if the turbulent viscosity is greater than the physical viscosity the turbulent production tensor will dominate over the stress tensor in the FE. The physical viscosity is

$$\eta_0 \sim \rho_0 \sqrt{u_0} l_\lambda \tag{5.23}$$

where u_0 is the mean thermal energy and l_λ the mean free path of a particle, so we see that the turbulent viscosity is greater than the physical viscosity, if

$$\frac{q_0^2}{u_0} \geq \left(\frac{l_\lambda}{l_0}\right)^2 \Rightarrow \frac{q_0^2}{u_0} \geq (Kn)^2, \tag{5.24}$$

which means the ratio of turbulent energy to internal energy must be greater than the square of the Knudsen number $Kn = \frac{l_\lambda}{l_0}$. Since in any case the Knudsen number must be much smaller than one for the continuum approximation to hold, we can practically always assume that the turbulent production tensor will dominate over the stress tensor.[8] This justifies our assumption in the Schmidt model to neglect the influence of the stress tensor completely in the momentum equation and therefore also in the kinetic energy equation.

For completeness we also compare the gravitational force to the turbulent pressure, which yields

$$\frac{\rho_0 q_0^2}{\rho_0 g_0 l_0} \geq 1. \tag{5.25}$$

Turbulence will thus dominate over gravity in the momentum equation, if the average turbulent energy is greater than the gravitational energy.

---

[8] Of course this analysis is restricted to $l_0 > l_k$, since if we resolve the fluid up to the Kolmogorov length l_k the turbulent energy will be zero. For scales smaller than the Kolmogorov length we cannot neglect the influence of the physical viscosity.

Internal energy equation

The internal energy equation can be analyzed in the same way as the momentum equation using the additional dimensionless quantities

$$e^*_{int} = \frac{e_{int}}{u_0},\ \lambda^* = \frac{\lambda}{\lambda_0} = \frac{\lambda}{q_0^2 v_0/l_0},\ \epsilon^* = \frac{\epsilon}{\epsilon_0} = \frac{\epsilon}{q_0^3/l_0}. \tag{5.26}$$

This results in

$$\begin{aligned}\frac{l_0}{t_0 u_0}\frac{\partial}{\partial t^*}\langle\rho^*\rangle\hat{e}^*_{int} + \frac{\partial}{\partial r_j^*}\hat{v}_j^*\langle\rho^*\rangle\hat{e}^*_{int} = &- \frac{p_0}{\rho_0 v_0^2}\langle p^*\rangle\frac{\partial}{\partial r_j^*}\hat{v}_j^* + \frac{\eta_0 v_0}{\rho_0 u_0 l_0}\langle{\sigma'}^*\rangle\frac{\partial}{\partial r_j^*}\hat{v}_j^* \\ &- \frac{q_0^2}{u_0}p_t\frac{\partial}{\partial r_j^*}\hat{v}_j^* + \frac{q_0^2}{u_0}\langle\rho^*\rangle\lambda^* + \frac{q_0^3}{v_0 u_0}\langle\rho^*\rangle\epsilon^*.\end{aligned} \tag{5.27}$$

We see that the pressure dilatation λ will dominate over the pressure term if

$$M_t^2 \geq \gamma \tag{5.28}$$

and that the turbulent dissipation ϵ will dominate over the viscous dissipation, if

$$\rho_0 l_0 q_0 \left(\frac{q_0}{v_0}\right)^2 \geq \eta_0 \Rightarrow \left(\frac{q_0}{v_0}\right)^2 \geq \frac{\eta_0}{\eta_t}. \tag{5.29}$$

As shown in section 5.3.2 $\eta_0 \ll \eta_t$, so we can always neglect the influence of the stress tensor in the internal energy equation. This also leads to the conclusion, that turbulence will be the only source of entropy in the equations, since the only irreversible conversion of energy into internal energy is via turbulent dissipation ϵ.

Turbulent energy equation

For the dimensional analysis of the turbulent energy equation we need the additional dimensionless quantity

$$\mathbb{D}^* = \frac{\mathbb{D}}{\rho_0 q_0^3/l_0}. \tag{5.30}$$

Inserting it together with the dimensionless quantities introduced in the former sections yields

$$\frac{l_0}{t_0 u_0}\frac{\partial}{\partial t^*}\langle\rho^*\rangle e_t^* + \frac{\partial}{\partial r_j^*}\hat{v}_j^*\langle\rho^*\rangle e_t^* = \frac{q_0}{v_0}(\mathbb{D}^* - \langle\rho^*\rangle\epsilon^*) - \frac{v_0}{q_0}\hat{\tau}_{ji}^{**}\frac{\partial}{\partial r_j^*}\widehat{v_i^*} - p_t^*\frac{\partial}{\partial r_i^*}\widehat{v_i^*} - \langle\rho^*\rangle\lambda^*. \tag{5.31}$$

This analysis shows that the behavior of turbulent energy equation can be completely characterized by the ratio $\frac{q_0}{v_0}$. If $\frac{q_0}{v_0} \gg 1$, then only diffusion $\mathbb{D}$ and dissipation ϵ are relevant. If $\frac{q_0}{v_0} \ll 1$ then the equation is dominated by the turbulent production term $\Sigma^* = \hat{\tau}_{ji}^*\frac{\partial}{\partial r_j}\hat{v}_i$ and only if $\frac{q_0}{v_0} \approx 1$ do all terms contribute to the equation.

5.4 Sarkar model

The effect of compressibility on the structure of turbulence is an important but difficult topic in turbulence modeling and is not really taken into account by the Schmidt model. Sarkar (1992) performed simulations of simple compressible flows and investigated the influence of the mean Mach number of the flow on the turbulent dissipation ϵ and the pressure dilatation λ. Based on this analysis he suggested different models for these terms, which we will describe in the following sections. These modifications have been proven to yield good results[9] and that's why we use them in the course of this work, when we reach the limitations of the original Schmidt model with our simulations.

5.4.1 Turbulent dissipation ϵ

As a major effect of compressibility from direct numerical simulation Sarkar (1992) identifies that the growth rate of kinetic energy decreases when the initial turbulent Mach number increases. This means that the dissipation of kinetic energy (and therefore also for the turbulent energy) increases with the turbulent Mach number M_t and Sarkar (1992) suggests accounting for this effect by using

$$\epsilon = C_\epsilon \frac{q^3}{l_\Delta}(1 + \alpha_1 M_t^2) \tag{5.32}$$

with $\alpha_1 = 0.5$ as a model for the dissipation of turbulent energy.

5.4.2 Pressure dilatation λ

Based on a decomposition of all variables of the equation for instantaneous pressure[10]

$$\frac{\partial^2}{\partial r_i^2} p = \frac{\partial^2}{\partial t^2} \rho - \frac{\partial^2}{\partial r_i \partial r_j}(\rho v_i v_j - \sigma'_{ij}) \tag{5.33}$$

into a mean and a fluctuating part and comparisons with direct numerical simulations of simple compressible flows Sarkar (1992) proposed a different model for the pressure dilatation

$$\lambda = \alpha_2 M_t \hat{\tau}^*_{ij} \frac{\partial \hat{v}_i}{\partial r_j} - \alpha_3 M_t^2 C_\epsilon \frac{q^3}{l_\Delta} - 8\alpha_4 M_t^2 p_t \frac{\partial \hat{v}_k}{\partial r_k} \tag{5.34}$$

with $\alpha_2 = 0.15$,$\alpha_3 = 0.2$ obtained from a curve fit of the model with DNS simulation. Unfortunately Sarkar (1992) does not specify a value for α_4, so there is some confusion in the literature about it. For example Shyy and Krishnamurty (1997) set $\alpha_4 = 0$ and still found the Sarkar model in good agreement with their DNS simulation. In this work, we adopt a value of $\alpha_4 = \alpha_2^2/2$, which was suggested in a work by Schmidt (2007).

---

[9] See Shyy and Krishnamurty (1997).

[10] For a derivation see appendix E.

6 AMR and LES

As mentioned in the last chapter, in LES we try to solve the FE instead of the UE and treat the unresolved scales with a subgrid scale model, which acts like a filter with a characteristic length l_Δ for the UE. However we can only model the subgrid scales in an averaging sense, which can only be correct, if the fluid motions on the subgrid scales are nearly isotropic. This limits the LES methodology to flows where we can resolve all anisotropies, which stem from large-scale features like boundary conditions or external forces. Therefore the ideal numerical method for LES would include adaptive gridding to ensure automatically that the grid, and hence the filter, are everywhere sufficiently fine to resolve the energy-containing motions (Pope, 2000, p. 636).

6.1 Adaptive mesh refinement

The most powerful technique for grid-based solvers to resolve localized and anisotropic structures in a flow is adaptive mesh refinement (AMR). Using AMR the grid will be refined[1], depending on a refinement criterion, only at the defined "interesting" areas of the flow field. This allows for treating a much bigger range of dynamic scales of the fluid with the same number of grid cells compared to a static grid.

The grid structure can thereby be understood as a hierarchy of grid patches (see figure 6.1) that approximate the flow on various levels of resolution (Berger and Oliger, 1984; Berger and Colella, 1989). But not only the spatial resolution, also the time resolution is adaptive. All grids on a given level are advanced simultaneously with a maximum timestep such that the Courant condition is satisfied by all the cells on that level. This results in a hierarchy of timesteps: a coarse, parent grid on level l is advanced by $\Delta t^{\mathrm{coarse}}$, and then its finer, subgrid(s) on level $l+1$ are advanced by one or more timesteps Δt^{fine} until they reach the same physical time as their parent grid. At this point, the coarse grid values u^{coarse} are replaced by the

---

[1] Refined means that the values from a coarse parent grid are interpolated onto a finer child grid and then integrated independently from the coarse grid. However, the way how to interpolate the values from coarse to fine grid is not discussed in the literature and most often not described by the developers of AMR fluid codes. Although outside the scope of our work, the dependence of the solution and the spectrum of the solution on this interpolation routines should be investigated in the future.

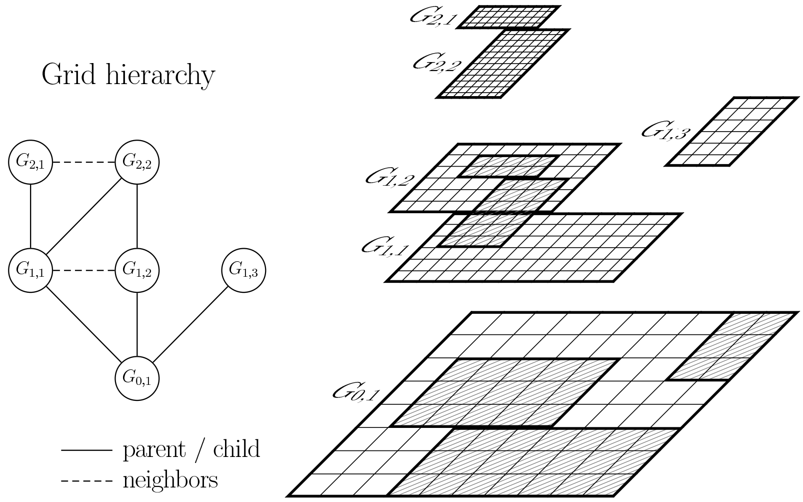

Figure 6.1: Hierarchy of rectangular subgrids in blockstructured AMR (Deiterding, 2003).

underlying fine grid values u_i^{fine} using mass weighted, conservative averaging[2]

$$u^{\text{coarse}} = \frac{1}{M}\sum_i \rho_i u_i^{\text{fine}} V_i, \tag{6.1}$$

where $M = \sum_i \rho_i V_i$ is the total mass of the underlying subgrid cells and V_i is the volume of a fine grid cell.

To completely ensure mass conservation, however, one not only has to replace the coarse grid values with averaged fine grid values, but also must correct coarse grid cells, which abut fine grid cells, but are not themselves covered by any fine grid. This can be understood, by writing the underlying, conservative, explicit finite difference scheme as

$$u_n(t + \Delta t^{\text{coarse}}) = u(t) - \frac{\Delta t^{\text{coarse}}}{\delta x}\left(F_{n+1/2}^{\text{coarse}} - F_{n-1/2}^{\text{coarse}}\right), \tag{6.2}$$

where $F_{n\pm1/2}$ are the fluxes on the left and right hand side of the cell number n respectively. If the left hand side of cell n abuts on a fine grid, the flux $F_{n-1/2}^{\text{coarse}}$ has to be replaced by the fluxes of the neighboring fine grid cells

$$F_{n-1/2}^{\text{fine}} = \sum_i F_{i+1/2}(t + i\Delta t^{\text{fine}}), \tag{6.3}$$

where the sum is due to the refinement in time. This flux replacement is most often implemented as a correction pass after a grid has been integrated using equation 6.2

$$u_n(t + \Delta t^{\text{coarse,corr}}) = u_n(t + \Delta t^{\text{coarse}}) + \Delta F \tag{6.4}$$

---

[2] Density itself is not weighted by mass but only by volume $\rho^{\text{coarse}} = \frac{1}{V}\sum_i \rho_i^{\text{fine}} V_i$.

with

$$\Delta F = -F^{\mathrm{coarse}}_{n-1/2} + \sum_i F_{i+1/2}(t + i\Delta t^{\mathrm{fine}}). \tag{6.5}$$

This "Flux Correction" step is the most difficult and error-prone part of an AMR implementation, since one has to track all the fluxes of the time varying boundaries of coarse and fine grids, and correctly maintain them between processors, if the simulation is run in parallel on several CPUs.

Nevertheless, if done correctly, this technique has proven to be very well suited for astrophysical problems which include strong shocks or gravitational collapse (Bryan et al., 2001) among many other applications. However, in the case of astrophysically relevant Reynolds numbers[3] even with AMR we cannot hope to resolve all relevant scales down to the dissipative scales (Schmidt et al., 2006b).

But as mentioned in the introduction, we do not have to resolve all scales if we use a SGS model. We only need to resolve energy-containing motions. That's the reason why combining LES and AMR offers the possibility of treating turbulence in astrophysical simulations in a much better way. Though there is one big problem, when trying to combine LES with AMR. Most of the terms of a SGS model like the Schmidt model do depend on the cutoff scale l_Δ of the grid and this cutoff scale varies in time and space if one uses AMR. But when filtering the fluid dynamic equations, we assumed our filter operation to commute with time and spatial derivatives and hence be static and isotropic, in direct contradiction to the methods of AMR. Therefore combining LES and AMR seem to pose a big challenge and only few attempts have been made so far.

6.2 Attempts to combine LES and AMR

Although proposals to combine LES and AMR are frequently made (e.g Pope (2004)), literature on the topic is still rare.

Probably the first attempt to combine LES and AMR is due to Sullivan et al. (1996). They used a kind of zero-filling to interpolate the solution between the coarse and fine grid. But their simulation of planetary boundary layers only used one static nested fine grid within a coarse grid and was therefore of limited use for more general problems. Boersma et al. (1997) came to the conclusion, using the methods of Sullivan et al. (1996), that with respect to statistics, the nested grid simulations are clearly superior to the results obtained with a simulation on a coarse grid in the whole flow domain. They also found that their solution of a 2d Kelvin-Helmholtz instability improves even in the area only covered by the coarse grid, an encouraging fact. Another approach to large eddy simulations using AMR was put forward by Cook (1999). He presented a method for computing a fine grid solution given a coarse grid solution and vice versa using a deconvolution with a gaussian filter. He showed how to avoid commutation errors with this technique, and that boundary errors are usually small. He also emphasized the advantage of using several nested grids instead of one stretched grid. He came to the conclusion, however, that shocks and other high-frequency phenomena should not be allowed to cross grid boundaries, which renders his method invalid for simulating compressible flows in astrophysics.

---

[3] See section 2.2.

A sophisticated approach is the multilevel algorithm for large-eddy simulation of turbulent flow by Terracol et al. (2001, 2003). [4] But although they use a time-dependent number of grids, the finer grids in their simulations always cover the whole computational domain and and are only used to improve the overall LES performance. Also methods based on wavelets have been proposed by Goldstein and Vasilyev (2004) and Léonard et al. (2006) and even for adaptive, unstructured grids (Mitran, 2001; Nägele and Wittum, 2003), but seem to be rarely used. The newest method to combine LES and blockstructured AMR comes from Pantano et al. (2007), but they use a very different SGS-model compared to the Schmidt model considered in our work and therefore it is unclear if their method is of general use.

Finally in an astrophysical context Falle (1994) claims to use a k-ϵ subgrid scale model build into the hierarchical adaptive grid code μCobra to treat the effect of turbulence on the large structure of radio jets. However the specific problems due to adaptive gridding are not mentioned in this paper and Falle (1994) himself comes to the conclusion that his treatment of turbulence is rather dubious. Nevertheless, the same model seems to be used in a recent paper by Pope et al. (2008) on the generation of optical emission-line filaments in galaxy clusters.

6.3 ϵ-based approach to combine AMR and LES

In this chapter, we want to present a new simple method to address the problem of combination of AMR and LES. It is based on the finding of section 5.3, that the turbulent dissipation ϵ is related to the dissipation scale, but in the Schmidt model (and most other SGS models) modeled depending on the cutoff scale. This is no problem, if we use a static grid in our fluid dynamic simulation, but it poses a problem in AMR simulations. The reason is that the time and spatial variance of l_Δ in an adaptive simulation leads to an artificial dependence of ϵ on the grid structure of the simulation. But as we now from Kolmogorovs theory of turbulence the average rate of dissipation should be independent of the length scale in fully developed turbulence. This would not be the case in a AMR simulation of fully developed turbulence, if ϵ depends on the cutoff scale, since the average turbulent energy and therefore the turbulent velocity q is independent of the lengthscale in a conservative AMR code. So our idea is to try to enforce the independence of ϵ on the grid patches of different cutoff scale in our AMR simulations of turbulence. Explicitely this can be written as

---

[4] Also see the book of Sagaut et al. (2006).

$$\epsilon(l_{\Delta,1}) = \epsilon(l_{\Delta,2}),\ l_{\Delta,1} > l_{\Delta,2} \tag{6.6}$$

where $\epsilon(l_{\Delta,1})$ is the value of the turbulent dissipation in one grid cell of the coarse grid and $\epsilon(l_{\Delta,2})$ is the average value of the turbulent dissipation after interpolation on a overlapping fine grid patch. Inserting our model for epsilon (5.3) we get

$$C_{\epsilon,1}\frac{q_1^3}{l_{\Delta,1}} = C_{\epsilon,2}\frac{q_2^3}{l_{\Delta,2}}. \tag{6.7}$$

Assuming $C_{\epsilon,1} = C_{\epsilon,2}$ this leads to

$$\frac{q_1^2}{q_2^2} = \left(\frac{l_{\Delta,1}}{l_{\Delta,2}}\right)^{2/3}, \tag{6.8}$$

which is a scaling relation for the turbulent energy. This scaling relation should hold between the turbulent energy on grid patches of different cutoff scale. But on the other side, the total energy must be locally conserved

$$\frac{1}{2}v_1^2 + \frac{1}{2}q_1^2 + u_1 = \frac{1}{2}v_2^2 + \frac{1}{2}q_2^2 + u_2. \tag{6.9}$$

Since in a conservative AMR code $u_1 = u_2$ and using the scaling relation (6.8) to eliminate q_2 we get

$$v_2^2 = v_1^2 + q_1^2\bigl(1 - r^{-2/3}\bigr), \tag{6.10}$$

where we introduced the refinement factor $r = \frac{l_{\Delta,1}}{l_{\Delta,2}}$. If we divide (6.10) by v_1^2 and assume isotropy, we can derive a relation for the components of velocity

$$v_{2,i} = v_{1,i}\sqrt{1 + \frac{q_1^2}{v_1^2}(1 - r^{-2/3})}. \tag{6.11}$$

If we write equation (6.8) like

$$q_2^2 = q_1^2 - q_1^2\bigl(1 - r^{-2/3}\bigr) \tag{6.12}$$

we see, that for infinite refinement $r \to \infty$ the turbulent velocity q_2 is zero as expected.

7 Numerical testing

7.1 The Enzo code

Enzo is a multiphysics, parallel AMR application for simulating the cosmological evolution and star formation written in a mixture of C++ and Fortran, making use of the message-passing interface (MPI) libaries and the HDF5 data format. Norman et al. (2007) describes the newest version of the code in detail. In the following we summarize the most important features of the code.

Enzo simulates the evolution of dark and baryonic matter in a self-consistent way on cosmological scales. Baryonic matter is evolved using a finite volume discretization of the compressible fluid dynamic equations in comoving coordinates[1]. The Piecewise Parabolic Method (PPM) in dual energy formalism for high Mach number flows is used to integrate these equations (Bryan et al., 1995). Energy source and sink terms due to radiative heating and cooling processes are included, but not used in our work. Also we do not use the multi-species (H, H+, He, He+, He++ and e-) capabilities of Enzo; instead we always set the gas to be fully ionized with a mean molecular weight $m_\mu = 0.6\,\mathrm{u}$. Dark matter is assumed to behave as collisionless fluid, obeying the Vlasov-Poisson system of equations[2]. Its evolution is solved using particle-mesh algorithms for collisionless N-body dynamics; specifically a second order accurate Cloud-in-Cell (CIC) formulation with leapfrog time integration is used. Dark matter and baryonic matter interact through their gravitational potential. The gravitational potential is computed by solving the Poisson equation on the adaptive grid hierarchy using Fast Fourier Transform and multigrid techniques. In generic terms, Enzo is a fluid solver for the baryonic matter coupled to a particle-mesh solver for the dark matter via a Poisson solver. The coordinates of the simulation domain are given as comoving coordinates in an expanding universe with a scale factor $a(t)$, which is computed as a solution of the Friedman equation.

The code uses blockstructured adaptive mesh refinement (as described in section 6.1) to achieve high resolution. To parallelize the computation, a concept of ghost grids is used. The root grid is split into a number of grid patches, at least as many as the number of processors. Then, as grids are added, each grid is placed by default on the same processor as its parent. Once the rebuild of the hierarchy has been completed on a given level, the load balancing ratio between processors is computed

---

[1] See appendix H.3.

[2] See appendix F.

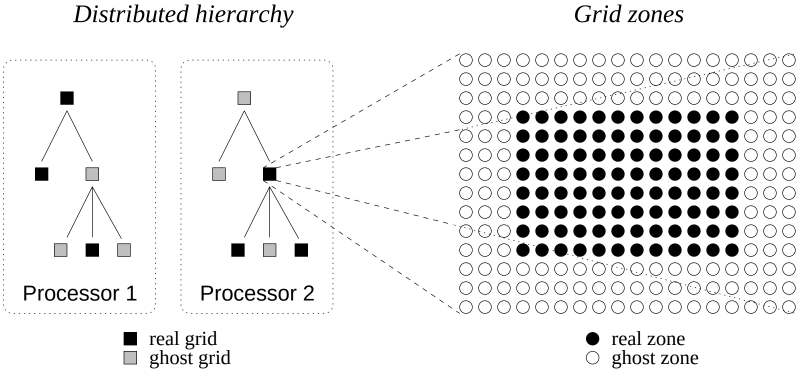

Figure 7.1: Real and ghost grids in a hierarchy; real and ghost zones in a grid (Norman et al., 2007).

and grids are transfered between processors in an attempt to even the load. However, the structure of the grid patch hierarchy is stored redundantly on every processor to ease communication. To allow for this, each real grid, which resides on only one processor, is represented by a ghost grid (which is a grid patch without data) on every other processor. This structure is shown graphically in figure 7.1.

Enzo is publicly available from http://lca.ucsd.edu/software/enzo/. However to integrate and test our SGS model several modifications to the public version were necessary.

7.2 Modifications to Enzo

7.2.1 Turbulent energy as a color field

To implement the Schmidt model into Enzo, it was necessary to introduce a new field for the turbulent energy, which is advected by the PPM solver. To achieve this, we used the capability of Enzo to incorporate an arbitrary number of color fields[3] into the simulation. Thus the turbulent energy field is implemented as another color field. Nevertheless it was necessary to change the default behavior of color fields in Enzo. By default, Enzo treats a color like a density. But since we want turbulent energy to be treated in analogy to the internal energy, which is implemented as specific quantity, we changed the treatment of color fields in our version of Enzo as to behave like a specific quantity.

---

[3] See appendix I.

7.2.2 Coupling of turbulent energy and time step restriction

The source/sink terms in the turbulent energy equation and the terms arising in the internal energy equation and the momentum equation due to our subgrid model are coupled to the fields in first order, which means for some arbitrary field f at timestep t_n, the source terms $s_1, s_2, \ldots$ are added in the following way

$$f_{n+1} = f_n + s_{1,n}\Delta t + s_{2,n}\Delta t + \ldots \tag{7.1}$$

where $\Delta t = t_{n+1} - t_n$ is the chosen timestep. But due to the low accuracy of the scheme, it might happen, that for a big timestep the value of one of the energy fields in a cell drops below zero, which is unphysical and numerically unstable. To account for that, we had to restrict the timestep in the code. We do this by applying the following estimator

$$\Delta t_{turb} = C_{turb} \min\left(\sqrt{\frac{l_\Delta}{|\boldsymbol{a}_{turb}|}}\right), \tag{7.2}$$

where the minimum is taken over all cells of all grids on one level of refinement, the turbulent acceleration is $\boldsymbol{a}_{turb} = \frac{1}{\langle\rho\rangle}\frac{\partial}{\partial r_j}\hat{\tau}(v_i, v_j)$ and $C_{turb} = 0.05$. If the so-estimated minimal allowed timestep due to our turbulent model Δt_{turb} is smaller than the timestep computed by the other estimators in the code (e.g. estimator based on the CFL-criterion, for gravity and so on) it will be chosen as the timestep for the next iteration. This procedure ensures that even for big turbulent acceleration (which also means big source/sink terms) due to our turbulent model, our computation is numerically stable. Of course, there is one drawback to this procedure: if the turbulent acceleration becomes really huge, the timestep of the simulation will be extremely small, effectively stopping the simulation. This can only be circumvented by either using a higher accuracy scheme for coupling the sink/source terms to the equations or by using a different subgrid model, which does not produce numerically instable huge values of $|\boldsymbol{a}_{turb}|$. The Sarkar corrections are a step in this direction, but further steps may be necessary in the future.

7.2.3 Transfer of turbulent energy at grid refinement/derefinement

By default, when a new finer grid gets created in Enzo, the values on the finer grid are generated by interpolating them from the coarser grid using a conservative interpolation scheme. At each timestep of the coarse grid, the values from the fine grid are averaged and replace the values computed on the coarse grid in the region where fine and coarse grid overlap. As already mentioned in section 6.3 these procedures must be modified in our approach to combine LES and AMR.

So at refinement we do the following:

1. Interpolate the values from the coarse to the fine grid using standard interpolation scheme from Enzo.

2. On the finer grid, correct the values of specific kinetic energy $e_k = \frac{1}{2}v^2$, velocity components v_i and specific turbulent energy $e_t = \frac{1}{2}q^2$ as follows

$$e_k' = e_k + e_t\big(1 - r^{-2/3}\big), \tag{7.3}$$

$$v_i' = v_i\sqrt{1 + \frac{e_t}{e_k}(1 - r^{-2/3})}, \tag{7.4}$$

$$e_t' = e_t - e_t\big(1 - r^{-2/3}\big), \tag{7.5}$$

   where primed quantities are the final values on the fine grid.

At derefinement we reverse this procedure:

1. Average the values from the fine grid and replace the corresponding values on the coarse grid

2. On the coarse grid, correct the averaged values of kinetic energy, velocity components and turbulent energy

$$e_t' = e_t + e_t\big(r^{2/3} - 1\big), \tag{7.6}$$

$$v_i' = v_i\sqrt{1 - \frac{e_t}{e_k}(r^{2/3} - 1)}, \tag{7.7}$$

$$e_k' = e_k - e_t\big(r^{2/3} - 1\big). \tag{7.8}$$

   Here primed quantities denote the final values on the coarse grid.

It should be noted that derefinement with this procedure is only possible if there is enough kinetic energy on the fine grid, because on the coarse grid, we must have $e_k' \geq 0$. This is only the case for

$$\frac{e_t}{e_k} \leq \big(r^{2/3} - 1\big). \tag{7.9}$$

For example for a refinement ratio $r = 2$ this yields $e_k \geq 0.58 e_t$. So if this criterion is not satisfied, we do not correct the values of the energies and velocities at derefinement.[4]

---

[4] One might ask, why not do the correction step before the interpolation/averaging step, since that might produce less noise. The reason for our choice was, that otherwise we would had to introduce an additional temporary field into the code, which would lower the performance.

7.2.4 Random forcing

To simulate driven turbulent flow, a random forcing mechanism was implemented into our version of Enzo. The forcing field is generated by a stochastic differential equation called Ornstein-Uhlenbeck process (Schmidt, 2004). This process generates a temporally and spatially varying force field which acts on the fluid. The components of the force are generated in Fourier space, because there it is easier to split the force field into a solenoidal and a dilatational (compressive) part.[5] Hence the force field is characterized by a weight ζ, which is zero, if the force field is purely compressive (which means it will not directly generate any vorticity), and one, if the force field is purely solenoidal (which means it will not directly generate any divergence in the velocity field). The strength of the force field is characterized by a forcing Mach number M_f, which is loosely connected to the mean Mach number reached in the simulation after one integral time

$$t_{int} = \frac{l_0}{M_f \langle c_s \rangle}, \tag{7.10}$$

where l_0 is the mean driving length scale size and $\langle c_s \rangle$ is the mean sound speed. The force field is adjusted to drive the fluid only on length scales around the characteristic forcing length $l_0 = \frac{l_{box}}{\alpha_f}$ with $\alpha_f = 2$ to allow for an undisturbed generation of the energy dissipation cascade down to smaller scales.

7.2.5 Statistics tool

To be able to extract and analyze statistical quantities from the simulation, sophisticated routines have been implemented, which allow us to compute mass weighted and normal mean values, standard deviations and root mean square values at every cycle for each quantity and for each level of an AMR simulation. We make heavy use of these routines in the following sections.

7.3 Energy conservation

Global conservation of energy in a fluid code with a SGS model like the Schmidt model is not achieved easily. This is because of the nonlocal features of this model. As shown in chapter 4, the equation of turbulent energy (4.29) is generated by subtracting the equation of resolved kinetic energy (4.30) from the filtered equation of turbulent energy 4.6. In other words, the sum of turbulent energy equation and resolved energy equation must yield the filtered kinetic energy equation. In particular, the sum of turbulent production term $\hat{\tau}(v_j, v_i)\frac{\partial}{\partial r_j}\hat{v}_i$ and resolved kinetic energy reduction term $\hat{v}_i \frac{\partial}{\partial r_j}\hat{\tau}(v_i, v_j)$ must add up to the corresponding flux term in the filtered equation of kinetic energy

---

[5] Also called Helmholtz decomposition, see Schmidt (2004).

$$\frac{\partial}{\partial r_j}\hat{v}_i\hat{\tau}(v_i, v_j) = \hat{v}_i\frac{\partial}{\partial r_j}\hat{\tau}(v_i, v_j) + \hat{\tau}(v_j, v_i)\frac{\partial}{\partial r_j}\hat{v}_i. \tag{7.11}$$

This is important, since we know that the integral of the flux term over the whole volume must be zero

$$\int \frac{\partial}{\partial r_j}\hat{v}_i\hat{\tau}(v_i, v_j)dV = \oint \hat{v}_i\hat{\tau}(v_i, v_j)dA = 0. \tag{7.12}$$

But this is not guaranteed numerically, if we compute the turbulent production term and the kinetic energy reduction term independent of each other, since small numerical errors might lead to a violation of equation (7.11) locally, which leads to a big violation of equation (7.12) globally.

We therefore compute the resolved kinetic energy reduction term indirectly as

$$\hat{v}_i\frac{\partial}{\partial r_j}\hat{\tau}(v_i, v_j) = \frac{\partial}{\partial r_j}\hat{v}_i\hat{\tau}(v_i, v_j) - \hat{\tau}(v_j, v_i)\frac{\partial}{\partial r_j}\hat{v}_i, \tag{7.13}$$

since this will guarantee, that equation (7.12) is fullfilled globally. We found that the global energy is thus much better conserved.

In the following we present our results on energy conservation. The analyzed simulation of driven turbulence has a static grid of size 1.0 (in code units) with a resolution of 256^3 grid points and periodic boundary conditions. At time $t = 0$ the baryonic fluid is at rest. The fluid is driven by random forcing as described in section 7.2.4 with $\zeta = 1.0$ and $M_f = 0.68$. The simulation is adiabatic (the adiabatic index $\gamma = \frac{5}{3}$) and uses none of the features necessary for a cosmological simulation (comoving coordinates, selfgravity, dark matter ...) except dual energy formalism. The mean sound speed of the simulation is $c_s = \sqrt{\gamma}$, since the mean pressure and density are set to one in code units.

The plots 7.2(a) and 7.2(b) show the typical time development of the mass weighted mean energies in our simulation including the energy injected into the system by random forcing. It is evident from the curve of the turbulent energy, that after one integral time scale, our simulation reaches a equilibrium between production and dissipation of turbulent energy.

In figure 7.3 we plotted the time development of the relative error $\frac{\Delta e(t)}{e(0)}$ of the mean total energy, which is the sum of the mass weighted means of internal energy, kinetic energy, turbulent energy minus the injected energy due to the forcing

$$\hat{e}_{tot} = \hat{e}_{int} + \hat{e}_{kin} + \hat{e}_t - \hat{e}_f, \tag{7.14}$$

where $\hat{e} = \frac{\langle \rho e \rangle}{\langle \rho \rangle}$. It demonstrates, that with our Schmidt model, the relative error in energy is comparable to the error without SGS model and is around 1%. Also the energy conserving properties of the Sarkar model are equally good.

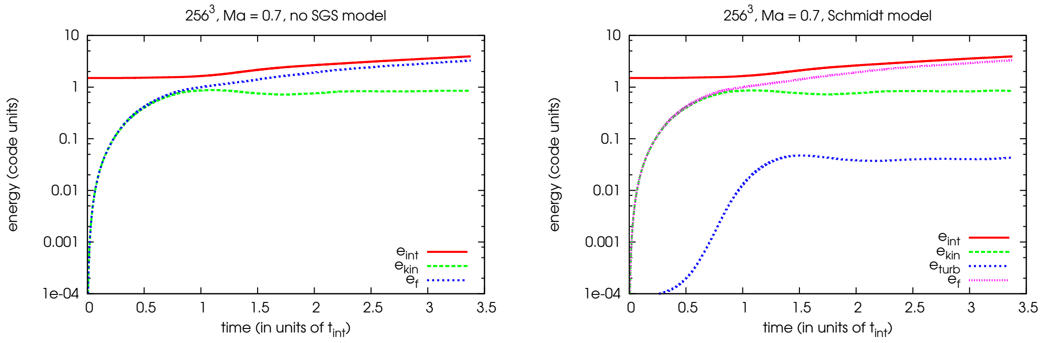

(a) No SGS model.

(b) Schmidt model.

Figure 7.2: Mass weighted mean energies over time in driven turbulence simulation.

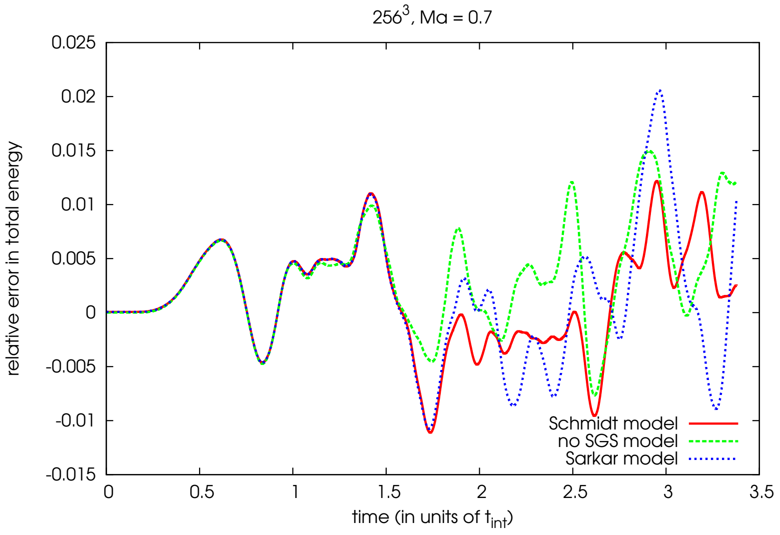

Figure 7.3: Relative error of total energy in the simulation.

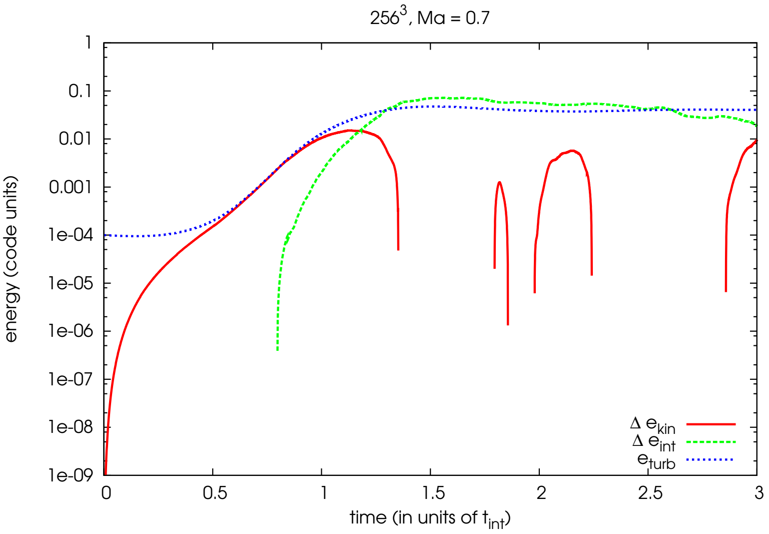

Figure 7.4: Differences in energies between simulation with and without SGS model, compared to the time development of the turbulent energy.

It is also instructive to plot the difference between internal energy of the simulation without the SGS model and the internal energy with the Schmidt model and the difference between the kinetic energies of both simulations. These differences are shown in figure 7.4. One can conclude from this figure, that, at the beginning of the turbulent driving, the turbulent energy produced in our simulation with SGS is found in the kinetic energy of the simulation without SGS. From $t = 1.2\ t_{int}$ on most of the turbulent energy can be found in the internal energy of the simulation without SGS. Turbulent energy can therefore be interpreted as a kind of buffer, which prevents the kinetic energy in our simulation to be converted instantly into thermal energy.

7.4 Scaling of turbulent energy

In our ϵ-based approach to combine AMR and LES we assumed that the turbulent energy scales according to equation (6.8) like $q^2 \sim l^{2/3}$. We conducted several simulations of driven turbulence to check the validity of this assumption.

The simulations were done on a static grid in a computational domain of size 1.0 with periodic boundary conditions. At time $t = 0$ the baryonic fluid is at rest. The fluid is driven by random forcing as described in section 7.2.4 with $\zeta = 0$ (purely solenoidal forcing). The simulations were done for nearly isothermal gas ($\gamma = 1.01$) with mean pressure and density set to 1.0 in code units. We used forcing Mach numbers of $M_f = 0.2$ and $M_f = 0.68$ and varied the resolution from 32^3 to 256^3 grid points. For $M_f = 0.68$ the simulations were transonic reaching reaching a Mach

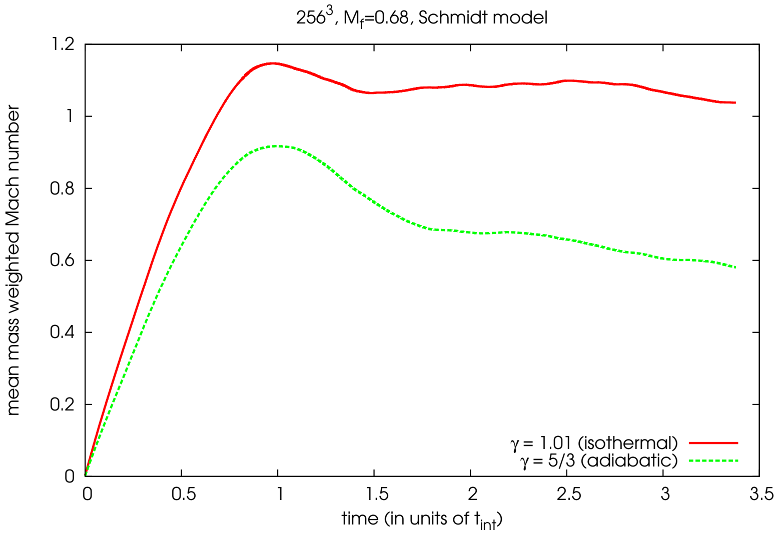

Figure 7.5: Mean Mach number for adiabatic and isothermal simulation using an equal forcing Mach number $M_f = 0.68$.

number around one (see figure 7.5).

The characteristic time development of the turbulent energy dependent on the resolution of the simulation can be seen in figures 7.6(a) - 7.6(d).

We compute mean turbulent energies by averaging the turbulent energy from $t = 3.0\ t_{int}$ to the end of the simulation and plot them against the resolution of the simulation. The results together with a power-law fit are shown in figures 7.7(a) and 7.7(b). From this we see that for a low Mach number forcing our assumption $q^2 \sim l^{2/3}$ (l is indirect proportional to the resolution) is fulfilled indeed. Nevertheless for high Mach number flows the scaling of turbulent energy becomes steeper and is $q^2 \sim l^{0.77}$ for the Schmidt model and $q^2 \sim l^{0.71}$ for the Sarkar model. In other words for higher Mach number flows, our correction of turbulent energy at grid refinement/derefinement based on relation (6.8) should probably be seen only as a good guess of the initial values of turbulent energy on the finer/coarser grid. Also we conclude that for higher Mach number flows one should use the Sarkar corrections to the Schmidt model, since this leads to a scaling of turbulent energy more similar to the incompressible low Mach number case.

7.5 Comparison of static grid to AMR turbulence simulations

To be consistent the results of an AMR simulation in the limit of complete refinement of the whole computational domain should resemble the results of a corresponding

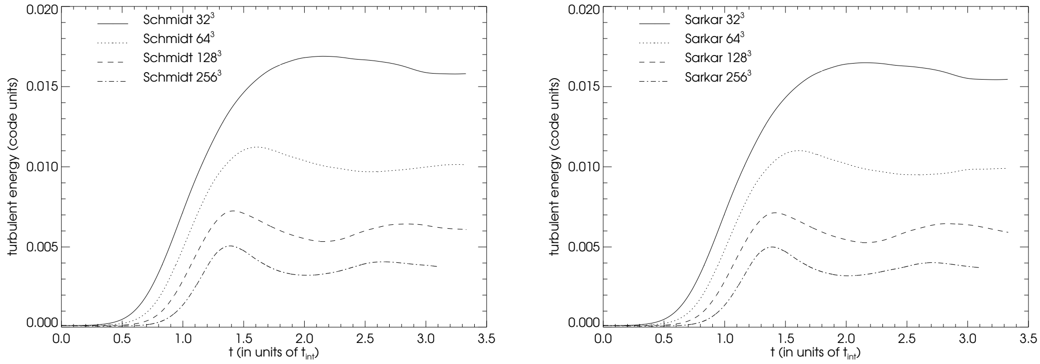

(a) Schmidt model, $M_f = 0.2$. (b) Sarkar model, $M_f = 0.2$.

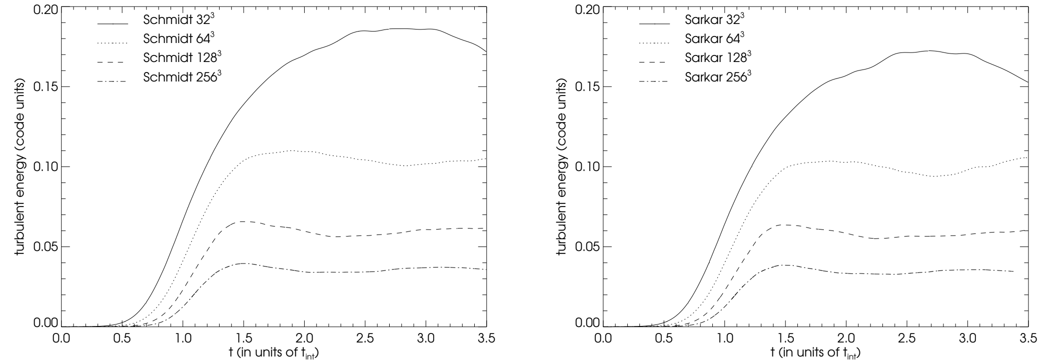

(c) Schmidt model., $M_f = 0.7$ (d) Sarkar model, $M_f = 0.7$.

Figure 7.6: Mass weighted mean turbulent energies over time in driven turbulence simulation, for resolutions 32^3 to 256^3 with forcing Mach number $M_f = 0.2$ and $M_f = 0.68$.

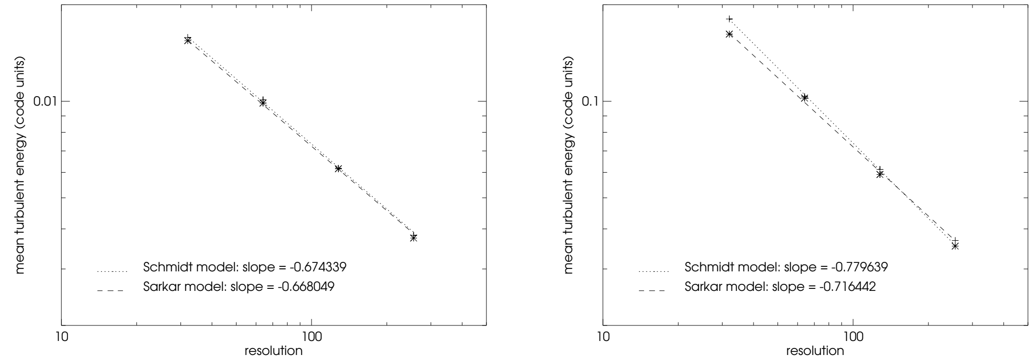

(a) $M_f = 0.2$. (b) $M_f = 0.68$.

Figure 7.7: Scaling of turbulent energy dependent on resolution for different strength of the forcing.

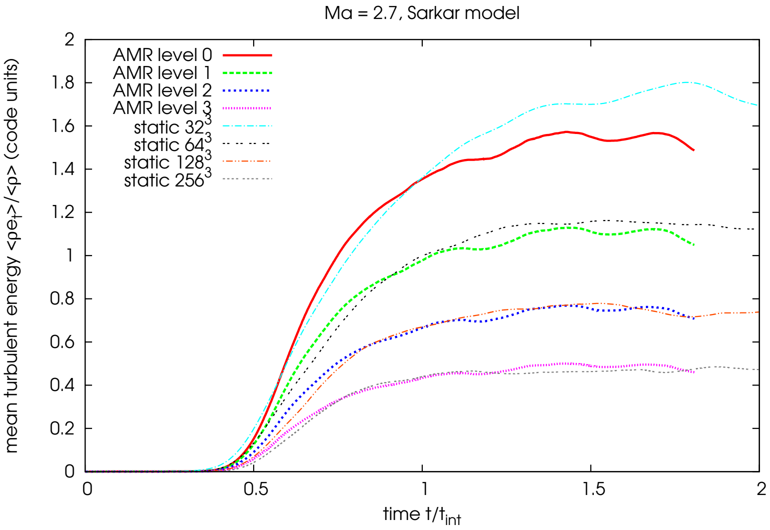

Figure 7.8: Thick lines: mean mass weighted turbulent energy for each level of the AMR simulation using our procedure of transferring turbulent energy at grid refinement/derefinement. Thin lines: the corresponding development of turbulent energy of the static grid simulations.

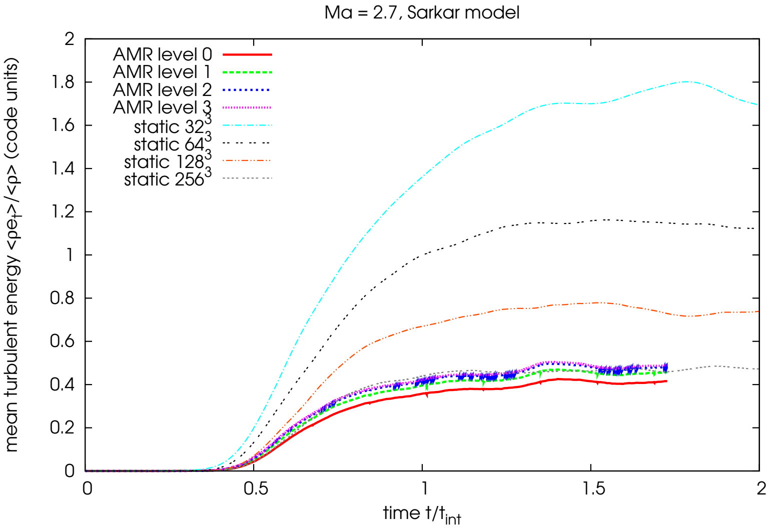

Figure 7.9: Thick lines: mean mass weighted turbulent energy for each level of the AMR simulation without transferring turbulent energy at grid refinement/derefinement. Thin lines: the corresponding development of turbulent energy of the static grid simulations.

static grid simulation. To test this, we compared an AMR simulation with a 32^3 root grid resolution and three additional levels with a refinement factor of 2 between each level, covering the whole domain, with the corresponding static grid simulations of driven turbulence with resolutions of $32^3, 64^3, 128^3$ and 256^3.

Again the simulations were done in a computational domain of size 1.0 with periodic boundary conditions. At time $t = 0$ the baryonic fluid is at rest. The fluid is driven by random forcing as described in section 7.2.4 with $\zeta = 0$ (purely solenoidal forcing). The simulations were done for nearly isothermal gas ($\gamma = 1.01$) with mean pressure and density set to 1.0 in code units. We used a forcing Mach number of $M_f = 2.7$ and therefore used the SGS model with Sarkar corrections.

The results of this consistency check can be seen in figure 7.8. We observe that the time development of the mean turbulent energy in this simulation of supersonic driven turbulence simulation is very similar on the different levels of the AMR simulation compared with the static grid simulations, except for some deviations at the root level. But comparing these results to a simulation without correcting turbulent energy at grid refinement/derefinement (figure 7.9), it is evident that our ϵ-based approach of turbulent energy transfer is much more consistent with the static simulations of driven turbulence.

8 Cluster physics

In the following we want to review some basic theoretical and observational facts of cluster physics. The presentation in this section has been inspired by Pfrommer (2005), Sarazin (1988), Voit (2005) and Plionis et al. (2008).

8.1 Cluster formation

8.1.1 Initial density fluctuations

On very large scales the universe appears homogeneous and isotropic. However the existence of stars, galaxies, and galaxy clusters demonstrates that the universe is not perfectly homogeneous. The early universe must have been slightly clumpy. These perturbations away from the mean density $\langle\rho\rangle$ can be characterized as a overdensity field

$$\delta(\boldsymbol{x}) = \frac{\rho(\boldsymbol{x}) - \langle\rho\rangle}{\langle\rho\rangle} \tag{8.1}$$

with Fourier transform

$$\delta(\boldsymbol{k}) == \frac{1}{(2\pi)^{3/2}} \iiint\limits_{-\infty}^{\infty} \delta(\boldsymbol{x}) e^{-i\boldsymbol{k}\boldsymbol{x}} dV. \tag{8.2}$$

In case that $\delta(\boldsymbol{x})$ is isotropic, it can be specified by an isotropic power spectrum

$$P(k) = \delta^*(k)\delta(k) = |\delta(k)|^2 . \tag{8.3}$$

If we assume, that the power spectrum has a power-law form $P(k) \sim k^n$, one can show (Peebles and Yu, 1970), that the gravitational potential fluctuations $\delta\Phi$ scale as

$$\delta\Phi \sim k^{(n-1)/2}. \tag{8.4}$$

Therefore the magnitude of these fluctuations diverges on either the small scale or the high scale end, except in the case of $n = 1$. This special property makes $P(k) \sim k$ the most natural power-law spectrum and it also appears to be a good approximation to the true power spectrum of density fluctuations in the early universe.

8.1.2 Hierarchical growth of density fluctuations

Once the universe has been seeded with density perturbations, they begin to grow, because the gravity of the overdense regions attracts matter away from neighboring underdense regions. The gravitational pull of the density perturbations on the smallest scales causes them to collapse first, because, as shown in the last section, the density perturbations have larger amplitude on smaller mass scales. That's why the standard model of cosmology envisions structure formation as a hierarchical process in which gravity is drawing matter together to form increasingly larger structures. Clusters of galaxies are believed to be the largest structures formed by this process nowadays. Since it is assumed in the standard model that most of the matter in the universe is cold, collisionless dark matter[1], the evolution of clusters is basically governed by the collisionless build-up of dark matter from small to successively larger haloes. In the course of this evolution, small structures merge to form larger structures. A full understanding of this hierarchical merging process requires numerical simulations, although its basic concepts can be obtained by means of the analytical spherical collapse model (Gunn and Gott, 1972; Bertschinger, 1985).

However, the accretion process in real clusters is not symmetric. Gravitational forces between merging matter clumps produce a time-varying collective potential which randomizes the velocities of the infalling particles yielding a Maxwellian velocity distribution. This process is known as violent relaxation (Lynden-Bell, 1967) and leads to a state of virial equilibrium. The final outcome of such a virialized, collisionless system would be a self-gravitating isothermal sphere, in which the velocity dispersion σ_v is constant and isotropic at every point and the density profile is

$$\rho(r) = \frac{\sigma_v^2}{2\pi G r^2}. \tag{8.5}$$

But this model leads to the unfortunate result of infinite mass and energy for a galaxy cluster, and so it can never exist in nature.

Numerical N-body simulations instead find that the profile of dark matter haloes is described by a universal law (Navarro et al., 1997)

$$\rho_{dm}(r) = \frac{\rho_{dm,0}}{r(r+r_0)^2}, \tag{8.6}$$

where ρ_0 is the central density and r_0 a characteristic scale radius. But even with this more sophisticated density profile mass diverges logarithmically with radius. Thus, the cluster's mass and relations linking that mass to observables depend crucially on the definition of the outer boundary of the cluster. It turns out, that their is no unique definition for the boundary of a cluster, however a common definition, also used in the analysis tools for this work, is the scale radius r_{200} within which the mean matter density is 200 times the critical density $\rho_{cr} = \frac{3H(z)^2}{8\pi G}$ of the universe [2].

---

[1] The evolution of cold, collisionless dark matter can be described by the Vlasov-Poisson system of equations, see appendix F.

8.2 Intracluster medium

It is widely assumed that the total matter density profile of the galaxy clusters follows the NFW dark matter profile (equation (8.6)), because the dark matter accounts for the biggest part of the total mass. The profile of the baryonic density will also follow the NFW profile on the larger scales, because the baryons follow the gravitational potential of the dark matter. Only in the core, significant deviations from the NFW profile can be expected for the baryonic density, since the baryons are not collisionless and pressure effects should lead to a different profile. This can be tested by measurements of the extended x-ray emissions of the intracluster medium and by numerical fluid dynamical simulations, if the mean free path of the very hot, but dilute ICM is small enough.

8.2.1 Mean free path of the ICM

To determine if the fluid assumption holds for the ICM, it is important to estimate the mean free path. The mean free path of electrons and protons in a plasma is determined by coulomb collisions. The electrons in a Maxwellian plasma undergo Coulomb collisions in a time which is a factor of $\sim \sqrt{m_e/m_p}$ shorter than the protons. On the other hand, the electrons move faster by the inverse of this factor. Thus, the mean free paths of electrons and protons are essentially equal, with (Plionis et al., 2008)

$$\lambda_e = \lambda_p \approx 23 \left(\frac{T}{10^8\,\mathrm{K}} \right)^2 \left(\frac{n_e}{10^{-3}\,\mathrm{cm}^{-3}} \right)^{-1} \mathrm{kpc}. \tag{8.7}$$

So for typical values of temperature and density of the ICM, we have mean free paths of the order of 10 kpc, which is roughly the scale of a galaxy.

However the ICM contains a significant magnetic field (Plionis et al., 2008), with typical values of $B = 1\,\mu\mathrm{G}$, which might be not dynamically relevant on large scales, but it alters the microscopic motions of the electrons and protons. In a magnetic field, charged particles follow helical orbits, gyrating about magnetic field lines. For example the gyroradius of a typical electron is

$$r_g \approx 9.72 \cdot 10^{-11} \left(\frac{T}{10^8\,\mathrm{K}} \right)^{1/2} \left(\frac{B}{1\,\mu\mathrm{G}} \right) \mathrm{kpc}. \tag{8.8}$$

---

[2] Although not precisely equivalent, we will call r_{200} the virial radius and the mass inside this radius the virial mass in our work.

These very small gyroradii probably ensure that the ICM acts as a fluid even when the Coulomb mean free paths are long.

8.2.2 Magnetic fields

The general consensus is that no mechanism can produce significant magnetic fields in the ICM prior to the formation of galaxies and large scale structures (Kulsrud and Zweibel, 2008). So where do the significant magnetic fields in the ICM mentioned in chapter 8.2.1 come from? It is assumed, that weak seed fields were created early in the universe by the so-called Biermann battery mechanism (Biermann and Schlüter, 1951), which predicts fields of a strength $\approx 10^{-20}\,$G. Several theories (e.g. Kulsrud and Anderson (1992)) expect that these seed fields were amplified by Kolmogorov turbulence by a factor of $10^{14} - 10^{15}$, which yields a magnetic field strength of $\approx 1\,\mu$G nowadays, a value which is observationally found in cores of galaxy clusters (Carilli and Taylor, 2002).

But what is the driving mechanism that generates the turbulence amplifying the magnetic field in cluster cores? One process is merger events. Roettiger et al. (1999) found that the field energy after a merger is found to increase by nearly a factor of three (and locally up to a factor of 20) with respect to a non-merging cluster. Since it is quite likely that a galaxy cluster experiences more than one of these events, the amplification will be even larger. Nevertheless the most significant process one can think of is the Kelvin-Helmholtz (KH) instability driven by shear flows, which are common during the formation of cosmic structures. When applied to a cluster core environment, the core dimensions basically define the injection scale and the KH timescale turns out to be 10^7 years, which makes this instability an interesting process to amplify weak magnetic fields (Dolag et al., 2008).

However although numerical simulations could show that the amplification of magnetic fields by shear flows is significant (Dolag et al., 2005a; Brüggen et al., 2005), they still have problems explaining the large amplification factors of the initial magnetic fields. Dolag et al. (2005a), who used a Magnetic Smoothed Particle Hydrodynamic code, had to assume a initial seed field of $10^{-11}\,$G at a redshift $z = 20$ to achieve realistic magnetic field strengths at $z = 0$. But these problems might be due to the numerical method used. Only recently it has been shown by Agertz et al. (2007), that Smoothed Particle Hydrodynamic (SPH) codes have severe problems describing Kelvin-Helmholtz instabilities. Although a solution to these problems has already been proposed by Price (2007), we have to assume, that up to now basically all SPH simulations of turbulence driven by flow instabilities are questionable. Hence a better treatment of turbulence is necessary to be able to study the evolution of magnetic fields in galaxy clusters.

8.2.3 X-ray observations of the ICM

X-ray observations are the most accurate source of information about galaxy clusters today. Observables in the X-ray band include the overall X-ray luminosity of a cluster, emitted by the hot plasma trapped in the cluster's gravitational potential and the cluster's temperature inferred from the X-ray spectrum of that plasma. From these data, one can reconstruct density, temperature and entropy profiles. Of course, projection effects, cluster substructure, and deviations from spherical symmetry complicate the generation of these profiles. However only recently Nagai et al. (2007) could demonstrate using data from cosmological simulations, that the methods used by Vikhlinin et al. (2006) for analyzing X-ray data of the the X-ray satellite CHANDRA can reliably recover the distribution of density and temperature of the hot ICM. So given these three-dimensional models for the gas density and temperature profiles, the total gravitational mass within the radius r can be estimated from the hydrostatic equilibrium equation in the form[3]

$$M(r) = -\frac{R_s T_g r}{G}\left(\frac{\partial \ln T_g}{\partial \ln r} + \frac{\partial \ln \rho_g}{\partial \ln r}\right). \tag{8.9}$$

Given $M(r)$, one can then calculate the total matter density profile

$$\rho(r) = \frac{1}{4\pi r^2}\frac{dM}{dr}. \tag{8.10}$$

The result of such an analysis (Vikhlinin et al., 2006) can be seen in figure 8.1. It is apparent, that the NFW profile provides a good fit for the density profile of the total mass of the clusters. The scatter in the baryonic density profiles is significantely larger and for lower temperature clusters the profiles are flatter towards the center of the cluster. The temperature profiles also show signs of self-similarity, at least for the higher temperature clusters $T > 2.5\,\mathrm{keV}$, which are fitted by

$$\frac{T(r)}{T_{mg}} = 1.35\frac{(x/0.045)^{1.9} + 0.45}{(x/0.045)^{1.9} + 1}\frac{1}{[1 + (x/0.6)^2]} \tag{8.11}$$

where $x = r/r_{500}$ according to (Vikhlinin et al., 2006). Also visible from the temperature fit are a isothermal plateau at $r \approx 0.2\,\mathrm{r}_{500}$ and the significant decrease of temperature towards the center. This behavior is often explained by assuming some cooling mechanism. Theoretically cooling should lead to lower pressure in the center of the cluster, thereby leading to an even denser core to maintain hydrostatic equilibrium. But, because cooling is even more effective at lower densities, this process is instable leading to catastrophic cooling of the core, which is not observed, giving rise to the so-called "cluster cooling flow problem". Observationally emissions from the central cluster gas can be detected for gas temperatures between the

---

[3] For a derivation see appendix G.

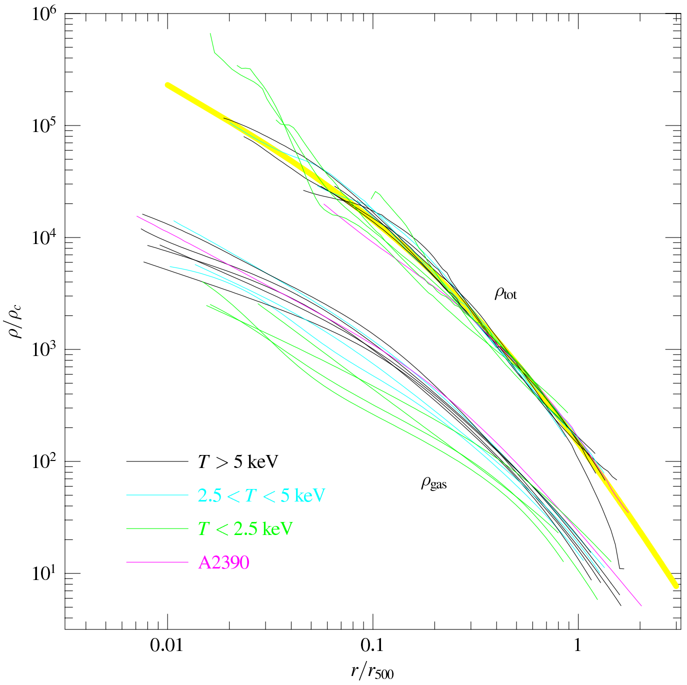

(a) Density profiles for gas density ρ_{gas} and total density ρ_{tot}.

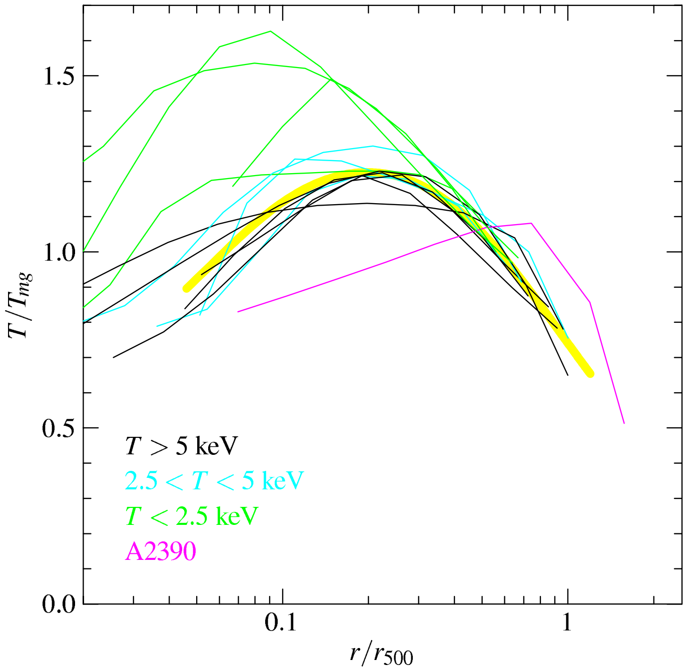

(b) Temperature profiles.

Figure 8.1: Scaled density and temperature profiles for galaxy clusters observed with CHANDRA by (Vikhlinin et al., 2006). The yellow line are a NFW fit to the total gas density and a average fit to the temperature profiles.

ambient temperature T_0 and $\sim T_0/2$, but not below $< T_0/3$ (Peterson et al., 2003), so some sort of heating mechanism seems to be inhibiting the cooling below this temperature. There are plenty of candidates for this - supernovae, outflows from active galactic nuclei, thermal conduction and turbulent mixing - but there is still no consensus on the relative importance of these mechanisms. Turbulence is especially interesting because it was also suggested by Nagai et al. (2007) as mechanism, which might explain some deviations in the computation of the total mass, based on the assumption of hydrostatic equilibrium, without taking turbulent pressure into account.

8.2.4 Turbulence in the ICM

The “bottom-up” model or hierarchical model of cosmological structure formation (eg., Ostriker, 1993) explains the build up of clusters through a sequence of mergers of lower-mass systems (stars → galaxies → groups → clusters). In particular, mergers of galaxies play a fundamental role in determining the structure and dynamics of massive clusters of galaxies. It is found that major mergers induce temperature inhomogeneities and bulk motions with velocities $> 1000\,\mathrm{km\ s}^{-1}$ in the intracluster medium (ICM) (Norman and Bryan, 1999). This results in complex hydrodynamic flows where most of the kinetic energy is quickly dissipated to heat by shocks, but some part may in principle also excite long-lasting turbulent gas motions.

In numerical simulations of merging clusters (Schindler and Mueller, 1993; Roettiger et al., 1997; Ricker and Sarazin, 2001; Takizawa, 2005) it has been shown that infalling subclusters generate a laminar bulk flow, but inject turbulent motions via Kelvin-Helmholtz instabilities at the interfaces between the bulk flows and the primary cluster gas. Such eddies redistribute the energy of the merger through the cluster volume and decay with time into more and more random and turbulent velocity fields, eventually developing a turbulent cascade with a spectrum of fluctuations expected to be close to a Kolmogorov spectrum (Dolag et al., 2005b).

The turbulent nature of the flow could be directly confirmed with the help of high-resolution X-ray spectroscopy of emission line broadening of lines of heavy ions. It has been suggested (Sunyaev et al., 2003), that the X-ray microcalorimeters (XRS) on board of the X-ray satellite ASTRO-E2[4] should be able to detect this broadening. But due to a critical flaw discovered in the XRS instrument in August 2005, this test has to be postponed until future instruments like XEUS are available. Nevertheless other observations have revealed some signature for turbulence in the ICM. For example Schuecker et al. (2004) analyzed the pressure fluctuation spectrum of the Coma cluster claiming that it scales according to Kolmogorov-Obukhov theory (see figure 8.2).

Vogt and Enßlin (2005) makes use of the Faraday rotation effect to investigate the

---

[4] Also called *Suzaku*.

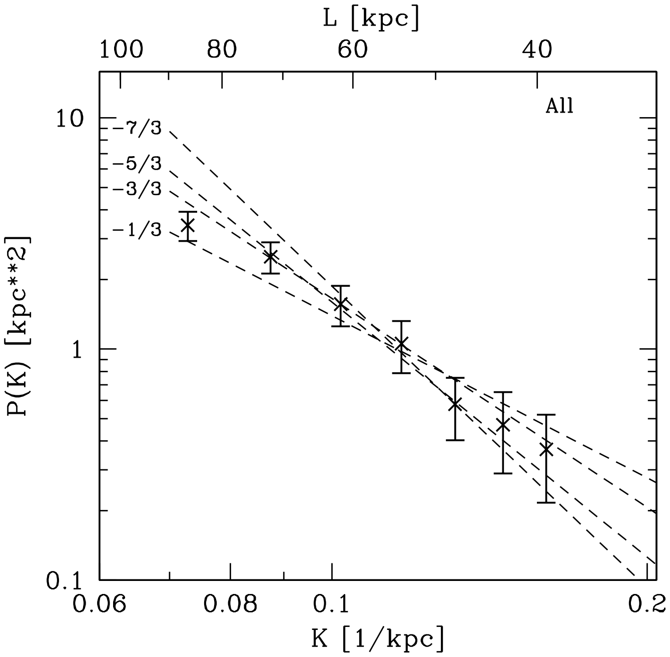

Figure 8.2: Observed projected shot-noise-subtracted power spectral densities (dots with 1σ error bars) compared with model predictions (dashed lines). From Schuecker et al. (2004).

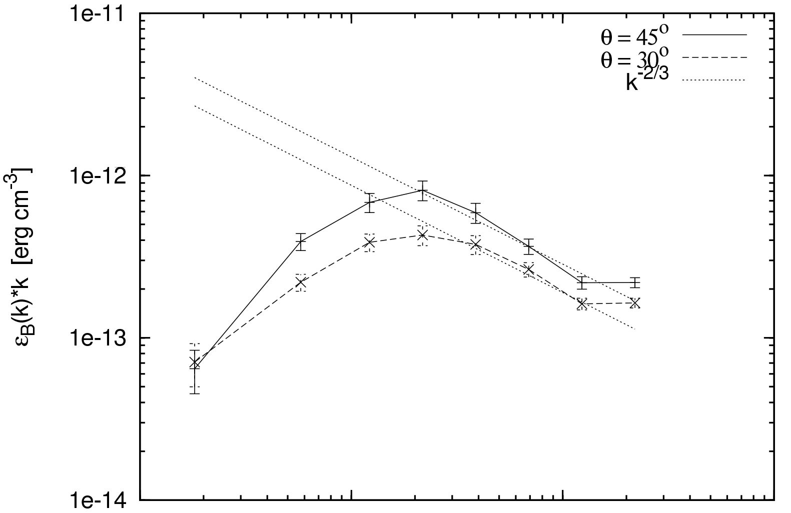

Figure 8.3: Power spectra for two different inclination angles $\theta = 30°$ and $\theta = 45°$. For comparison a Kolmogorov-like power spectrum is plotted as a straight dashed line. One can see that the calculated power spectra follow such a power spectrum over at least one order of magnitude. From Vogt and Enßlin (2005).

magnetic field structure of the ICM in the Hydra cluster. They extract magnetic field strength power spectra from their data and find a Kolmogorov scaling behavior below a length scale of 1 kpc (see figure 8.3) .

Furthermore the broadening of the iron abundance profile in the core of the Perseus cluster (Rebusco et al., 2005) and other galaxy clusters (Rebusco et al., 2006) and the lack of resonant scattering in the 6.7 keV He-like iron K_α line in the Perseus cluster (Churazov et al., 2004) can also be interpreted as evidence for the turbulent state of the ICM.

9 Simulations of galaxy clusters

9.1 Details of the simulations

We performed two simulations of cluster formation with Enzo following Iapichino and Niemeyer (2008). One simulation was done with the Schmidt SGS model including the Sarkar corrections and some additional modifications described below. For comparsion we conducted a second simulation without SGS model. In the following section we describe the common features of these two simulations, in section 9.1.2 we describe some additional numerical issues, which had to be taken into account when doing a cluster simulation with SGS model in comoving coordinates.

9.1.1 Common features

The simulations were done using a flat (critical density $\Omega = 1$) cold dark matter (CDM) background cosmology with a dark energy density $\Omega_\Lambda = 0.7$, a total (including baryonic and dark matter) matter density $\Omega_m = 0.3$, a baryonic matter density $\Omega_b = 0.04$, the Hubble parameter set to $h = 0.7$, a galaxy fluctuation amplitude $\sigma_8 = 0.9$, and a scalar spectral index $n = 1$. Both simulations were started with the same initial conditions at redshift $z_{ini} = 60$, using the Eisenstein and Hu (1999) transfer function, and evolved to $z = 0$. The simulations were adiabatic with a heat capacity ratio $\gamma = 5/3$ assuming a fully ionized gas with a mean molecular weight $m_\mu = 0.6\,\mathrm{u}$. Cooling physics, magnetic fields, feedback, and transport processes are neglected.

The simulation box had a comoving size of $128\,\mathrm{Mpc\ h^{-1}}$. It was resolved with a root grid (level $l = 0$) of 128^3 cells and 128^3 N-body particles. A static child grid ($l = 1$) was nested inside the root grid with a size of 64 Mpc/h, 128^3 cells and 128^3 N-body particles. The mass of each particle in this grid was $9 \times 10^9\,\mathrm{M_\odot\ h^{-1}}$. Inside this grid, in a volume of $38.4\,\mathrm{Mpc\ h^{-1}}$, adaptive grid refinement from level $l = 2$ to $l = 6$ was enabled using a overdensity refinement criteria as described in Iapichino and Niemeyer (2008) with an overdensity factor $f = 4.0$. The refinement factor between two levels was set to $r = 2$, allowing for a effective resolution of 8196^3 cells or $15.6\,\mathrm{kpc\ h^{-1}}$.

The static and dynamically refined grids were nested around the place of formation of a galaxy cluster, identified by Iapichino and Niemeyer (2008) using the HOP algorithm (Eisenstein and Hut, 1998). The cluster had a virial mass of $M_{vir} =$

$5.49 \times 10^{14}\,\mathrm{M}_\odot\ \mathrm{h}^{-1}$ and a virial radius of $R_{vir} = 1.33\,\mathrm{Mpc\ h}^{-1}$ for both simulations.

9.1.2 Numerical issues

Running robust simulations including a SGS model like the Schmidt or Sarkar model in a comoving cosmological background requires some additional techniques not yet discussed. Apart from the additional terms due to comoving coordinates in the filtered equations, these techniques help to handle the extreme high turbulent Mach numbers, which appear on the coarsest grids in these simulations and are briefly described in the following sections.

Filtered equations of fluid dynamics in comoving coordinates

Filtering the equations of fluid dynamics in comoving coordinates (H.25)-(H.27) can be done in the same way as filtering the equations in cartesian coordinates as shown in chapter 4. As a result we get

$$\frac{\partial}{\partial t}\langle\tilde{\rho}\rangle + \frac{1}{a}\frac{\partial}{\partial x_j}\hat{u}_j\langle\tilde{\rho}\rangle = 0, \tag{9.1}$$

$$\begin{aligned}\frac{\partial}{\partial t}\langle\tilde{\rho}\rangle\hat{u}_i + \frac{1}{a}\frac{\partial}{\partial x_j}\hat{u}_j\langle\tilde{\rho}\rangle\hat{u}_i =& -\frac{1}{a}\frac{\partial}{\partial x_i}\langle\tilde{p}\rangle + \frac{1}{a}\frac{\partial}{\partial x_j}\langle\sigma'_{ij}\rangle + \langle\tilde{\rho}\rangle\hat{g}^*_i - \frac{1}{a}\frac{\partial}{\partial x_j}\hat{\tau}(u_i,u_j)\\ &-\frac{\dot{a}}{a}\langle\tilde{\rho}\rangle\hat{u}_i,\end{aligned} \tag{9.2}$$

$$\begin{aligned}\frac{\partial}{\partial t}\langle\tilde{\rho}\rangle e_{res} + \frac{1}{a}\frac{\partial}{\partial x_j}\hat{u}_j\langle\tilde{\rho}\rangle e_{res} =& -\frac{1}{a}\frac{\partial}{\partial x_i}\hat{u}_i\langle\tilde{p}\rangle + \frac{1}{a}\frac{\partial}{\partial x_j}\hat{u}_i\langle\sigma'_{ij}\rangle + \frac{1}{a}\langle\tilde{\rho}\rangle\hat{u}_i\hat{g}^*_i\\ &-\frac{\dot{a}}{a}\left(\langle\tilde{\rho}\rangle e_{res} + \frac{1}{3}\langle\tilde{\rho}\rangle\hat{u}_i\hat{u}_i + \langle\tilde{p}\rangle\right)\\ &+\langle\tilde{\rho}\rangle(\lambda+\epsilon) - \frac{1}{a}\hat{u}_i\frac{\partial}{\partial x_j}\hat{\tau}(u_i,u_j) - \frac{1}{a}\frac{\partial}{\partial x_j}\hat{\tau}(u_j,e_{int}),\end{aligned} \tag{9.3}$$

$$\frac{\partial}{\partial t}\langle\tilde{\rho}\rangle e_t + \frac{1}{a}\frac{\partial}{\partial x_j}\hat{u}_j\langle\tilde{\rho}\rangle e_t = \mathbb{D} + \Gamma - \langle\tilde{\rho}\rangle(\lambda+\epsilon) - \frac{1}{a}\hat{\tau}(u_j,u_i)\frac{\partial}{\partial x_j}\hat{u}_i - 2\frac{\dot{a}}{a}\langle\tilde{\rho}\rangle e_t. \tag{9.4}$$

In the source code of Enzo the derivatives are always taken with respect to $r_i = ax_i$ and the additional terms due to comoving coordinates in momentum and resolved energy equation are already implemented. So the only term we had to implement additionally compared to the non-comoving case was the term $2\frac{\dot{a}}{a}\langle\tilde{\rho}\rangle e_t$ in the equation of turbulent energy. Furthermore for the subgrid model terms it is necessary to take into account that the Jacobian of the velocity in comoving coordinates is[1]

$$J_{ij} = \frac{\partial}{\partial r_i} v_j = \frac{1}{a} \frac{\partial}{\partial x_i} u_j + \frac{\dot{a}}{a} \delta_{ij}. \tag{9.5}$$

The tracefree rate of strain tensor in comoving coordinates for example can then be easily expressed in terms of the Jacobian of the velocity field

$$S^*_{ij} = \frac{1}{2}(J_{ij} + J_{ji}) - \frac{1}{3} \delta_{ij} J_{kk}. \tag{9.6}$$

Basically all terms in the subgrid model using derivatives of the resolved velocity are therefore written in terms of the Jacobian of the velocity.

Turbulent energy cutoff and lower limit for temperature

High turbulent Mach numbers occur in cosmological simulations especially in the very cold, low-density voids of the computational domain. To make sure that in our adiabatic simulation the temperature and therefore the sound speed doesn't drop to unphysical low values we introduced a lower limit of the temperature $T_{min} = 10\,\mathrm{K}$. This value is reasonable, since no gas in the universe can have a temperature lower than the cosmic microwave background temperature of 2.7 K for a longer time. Since there are presumably more heating mechanisms like UV-heating, choosing 10 K as a lower limit seems to be a rational choice.

On the other side, low density gas can be accelerated very quickly in a gravitating field, leading to high velocity gradients, which lead to production of high amounts of turbulent energy according to the turbulent viscosity hypothesis. However the validity of the turbulent viscosity hypothesis has never been tested or verified in astrophysical flows. We are therefore free to assume that for flows with high velocity gradients, the production of turbulent energy is restricted and use as an upper limit of the turbulent Mach number $M_{t,max} = \sqrt{2}$. The exact value of this limit is based on the idea that in an isothermal gas (speed of sound $c_{\mathrm{s,iso}} = \frac{p_{th}}{\rho}$), the total pressure can be expressed as

$$p_{tot} = \rho c_{\mathrm{s,iso}}^2 + \frac{1}{3} \rho q^2 = \gamma_{\mathrm{eff}} \rho c_{\mathrm{s,iso}}^2. \tag{9.7}$$

If we assume that γ_{eff} is not allowed to be higher than the adiabatic value $\gamma = 5/3$, we have to limit the isothermal turbulent Mach number to $\frac{q}{c_{\mathrm{s,iso}}} \leq \sqrt{2}$.

Treatment of shocks

Shocks form unavoidably during cosmological structure formation due to infalling plasma which accretes onto filaments, sheets, and halos, as well as due to supersonic flows associated with merging substructures (Pfrommer et al., 2006). But shocks are the most localized and anisotropic features of a flow and therefore cannot be treated by an SGS model, which is based on the assumption of isotropy of the flow on the subgrid scales.[2] So in principle, shocks should be treated by the mechanisms of AMR alone and the SGS model should not influence the shocks. That's why we implemented a simple shock detector

---

[1] See equation (H.7) in the Appendix.

$$-\frac{\partial v_i}{\partial r_i} l_\Delta > c_s, \tag{9.8}$$

which marks all cells, where the velocity increments are greater than the speed of sound, as shocks. At these cells, we disable the SGS model, which means no production or dissipation of turbulence takes place. The turbulent energy is only advected in these cells.

9.2 Results

9.2.1 Energy conservation

Energy conservation is crucial for any adiabatic fluid dynamic simulation. However it is difficult to test for this directly in our setup, since we cannot extract easily the energy injected by gravity into the system. By plotting the time development of the mass weighted mean total energy in the system, which is for the simulation without SGS model the sum of mass weighted mean internal energy and mass weighted mean kinetic energy and for the simulation with Sarkar model the sum of mass weighted means of internal, kinetic and turbulent energy, we can still gain some insights into the differences between the two simulations.

This is what has been done in figure 9.1. From it we can see that the time development of the total energy is nearly identical, if we take the turbulent energy into account when computing the total energy of the simulation with Sarkar model. On the other side, the difference between the sum of kinetic and internal energy between the simulations seems to be again mostly accounted for by the turbulent energy, a result similar to what was already found in the simulations of driven turbulence.[3] We can also infer from figure 9.1, that the SGS model mainly changes the ratio of mean internal to mean kinetic energy and does not have much influence on the mean potential energy of the system. However, this is to be expected, since most of the gravitational potential is due to dark matter anyway, and we do not model the influence of gravity on subgrid scales and vice versa in our SGS model. This leads us to conclude that the general effects of our SGS model in a selfgravitating fluid are very similar to the effects found in the driven turbulence simulations without self gravity.

---

[2] Also see chapter 6.

[3] See section 7.3.

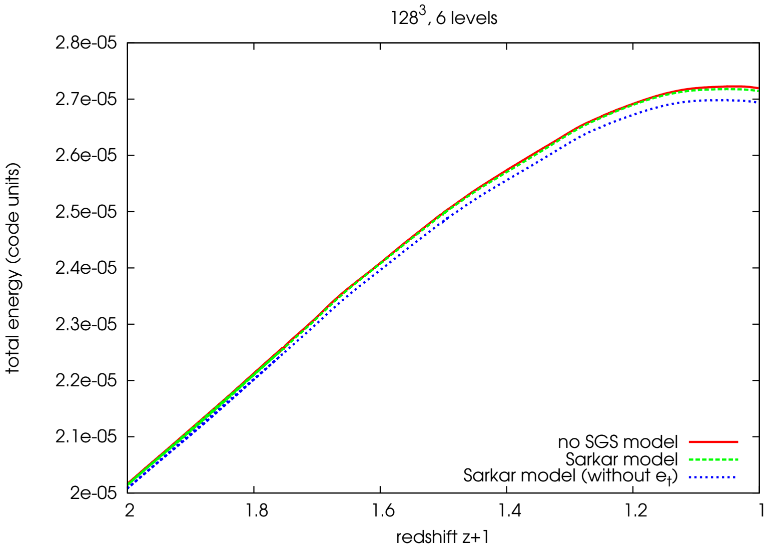

Figure 9.1: Time development of total energy in cluster simulation with and without SGS model.

9.2.2 Mass fractions of different gas phases

The IGM on large scales of the universe can be classified roughly into four phases according to gas temperature: the hot gas with $T > 10^7\,\mathrm{K}$ inside and around clusters; the warm-hot intergalactic medium (WHIM) with $10^5\,\mathrm{K} < T < 10^7\,\mathrm{K}$ found mostly in filaments; the low temperature WHIM with $10^4\,\mathrm{K} < T < 10^5\,\mathrm{K}$ distributed mostly as sheetlike structures; and the diffuse cold gas with $T < 10^4\,\mathrm{K}$ residing mostly in voids (Cen and Ostriker, 1999; Kang et al., 2005). To investigate the influence of the SGS model on these different gas phases, we plotted the time development of the mass fractions according to each of the phase for the simulation with and without SGS model (figure 9.2(a) and 9.2(b)). We also show the mass fractions of each gas phase at redshift $z = 0$ in table 9.1. The results seem to indicate that the SGS model leads to higher mass fraction of the voids and a lower mass fraction of the filaments compared to the simulation without SGS model. However our simulation domain is not very well resolved outside the central region, since we do not allow for adaptive refinement there. If we restrict our analysis to the adaptively refined

Run	$\frac{m_{\mathrm{cluster}}}{m_{\mathrm{all}}}$ [%]	$\frac{m_{\mathrm{filaments}}}{m_{\mathrm{all}}}$ [%]	$\frac{m_{\mathrm{sheets}}}{m_{\mathrm{all}}}$ [%]	$\frac{m_{\mathrm{voids}}}{m_{all}}$ [%]
no SGS	5.50	40.3	4.22	49.1
SGS	5.47	37.5	3.28	53.0

Table 9.1: Mass fractions of different gas phases at redshift $z = 0$.

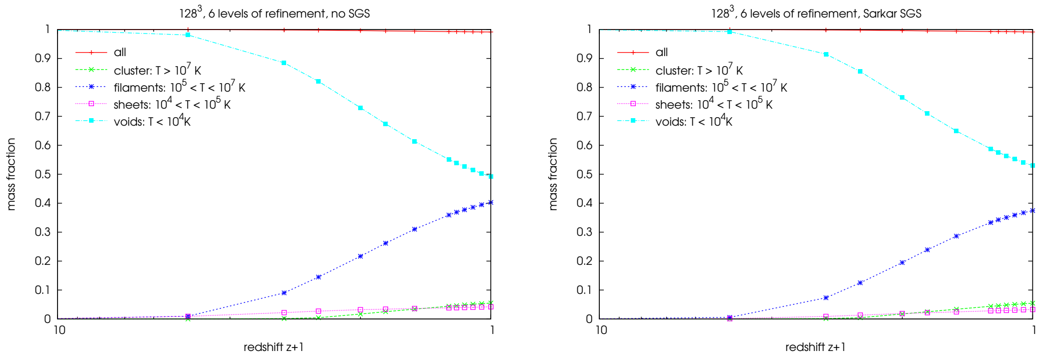

(a) No SGS model.
(b) SGS model.

Figure 9.2: Time development of mass fractions of different gas phases in the whole simulation box had with a comoving size of 128 Mpc h^{-1}.

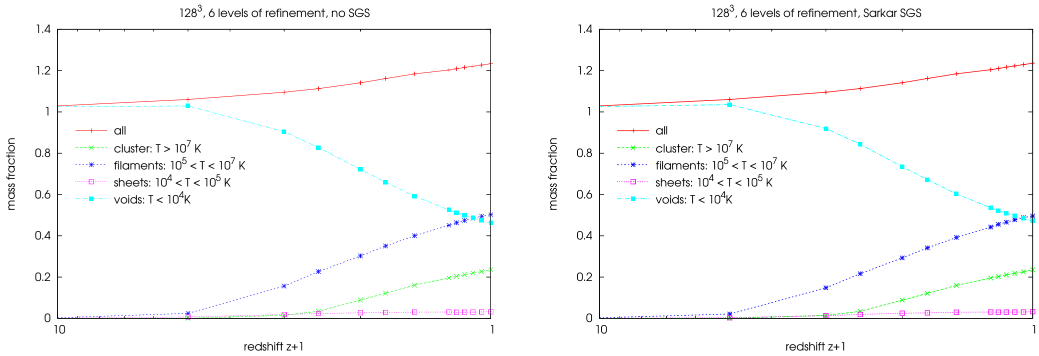

(a) No SGS model.
(b) SGS model.

Figure 9.3: Time development of mass fractions of different gas phases in the centered subset of the simulation box with a comoving size of 38.4 Mpc h^{-1}. One can see that the total mass in this open region is not conserved.

region in the box with a size of 38.4 Mpc h^{-1}, the differences between the simulation with SGS model and without SGS model vanish (figure 9.3(a) and 9.3(b)). This can also be seen from the mass fractions at redshift $z = 0$ normalized to the total mass in the central region in table 9.2. From these results we conclude that the SGS model has no or only very little influence on the mass fractions of the different gas phases in the simulations. For the important mass fraction of the WHIM we get $\approx 38\%$, which is higher than found by Davé et al. (2001, simulation B1) ($\approx 32\%$) with a lower resolution AMR simulation, but lower than found by Gottlöber et al. (2006) ($\approx 40\%$), who used smoothed particle hydrodynamic (SPH) with 2×1024^3 particles to simulate a box of size 500 Mpc h^{-1}; so we are also consistent with the literature in this respect.

Run	$\frac{m_{\mathrm{cluster}}}{m_{\mathrm{all}}}$ [%]	$\frac{m_{\mathrm{filaments}}}{m_{\mathrm{all}}}$ [%]	$\frac{m_{\mathrm{sheets}}}{m_{\mathrm{all}}}$ [%]	$\frac{m_{\mathrm{voids}}}{m_{all}}$ [%]
no SGS	19.2	40.8	2.61	37.5
SGS	19.0	40.1	2.64	38.2

Table 9.2: Mass fractions of different gas phases at redshift $z = 0$ for the adaptively refined region with a size of 38.4 Mpc h^{-1}.

9.2.3 Development of turbulence in different gas phases

The eddy turnover time t_l associated with a scale l

$$t(l) = \frac{l}{q(l)} \tag{9.9}$$

is the typical time for a structure of size $\sim l$ to undergo a significant distortion due to turbulent motions characterized by the typical turbulent velocity $q(l)$ at that scale (Frisch, 1995). So if we divide the age of the universe $t(z)$ by the eddy turnover time, we get the number of eddy turnovers

$$n(l, z) = \frac{t(z)}{t(l)} \tag{9.10}$$

at a given redshift z at a scale l. If $n > 1$, there has been enough time for eddies of size l to cascade down to smaller scales and we can call the fluid turbulent at scale l.

In static grid simulations one often chooses to use the grid resolution l_Δ as characteristic length scale and to compute a characteristic velocity and eddy turnover time for this scale. However in an AMR code it is not trivial to compute the turbulent velocity q_l associated with a characteristic length scale $l = l_\Delta$, since l_Δ is varying in time and space. To circumvent this difficulty, we assume that below the grid resolution at a certain position turbulent velocity scales according to Kolmogorov

$$q(l) \sim l^{1/3}. \tag{9.11}$$

We thereby assume that locally, the cascade starts at a different length scale characterized by the different resolution of our grid at that position. We also assume that our refinement criterion tracks and finds the regions inside the fluid, which do not scale according to Kolmogorov, and refines them until a Kolmogorov scaling is reached. Of course one might doubt that our refinement criterion based on overdensity will accomplish that. But since in cosmological simulations gravity is basically the energy-injecting force in the fluid and gravity is strongest in regions of high density, one can argue that in regions of high density, the Kolmogorov cascade starts at smaller length scales and the energy injecting scales in these regions have

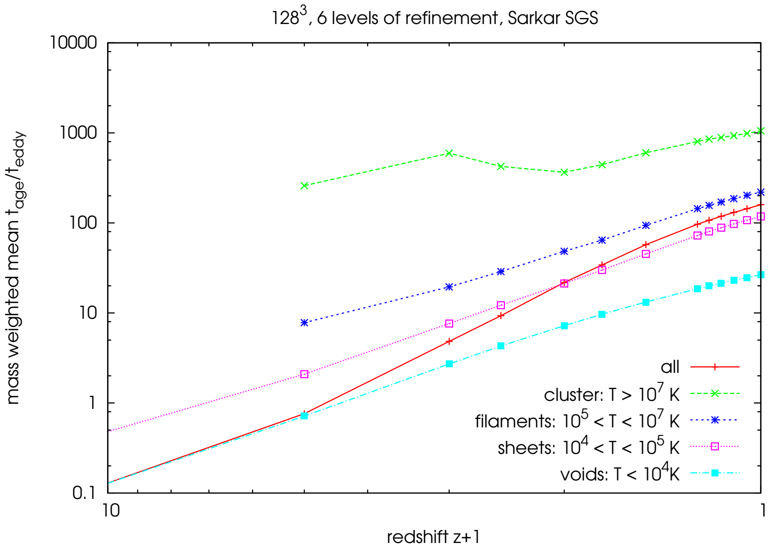

Figure 9.4: Mean number of eddy turnovers for gas phases of different temperature over time.

to be refined with a finer grid. Of course a criterion solely based on density might be necessary, but is not at all sufficient to track regions of Non-Kolmogorov scaling. More research needs to be done in this direction, but it is outside of the scope of this work.

For the analysis in our work, we adopt the hypothesis of local Kolmogorov scaling below the grid resolution. As a characteristic scale of our analysis, we choose the length scale of our highest resolved regions, which is $l_{min} = 15.6\,\mathrm{kpc\ h^{-1}}$. The turbulent velocity in the highest resolved regions can be directly computed from the values of the turbulent energy $q(l) = \sqrt{2e_t}$ on the grid; the turbulent velocity in less refined regions is scaled down according to our local Kolmogorov hypothesis as

$$q(l_{min}) = q(l_\Delta)\left(\frac{l_{min}}{l_\Delta}\right)^{1/3}. \tag{9.12}$$

Using this scaled turbulent velocity to compute the eddy turnover time, we plotted the mean mass weighted number of eddy turnovers at l_{min} with respect to redshift (see figure 9.2.3). We can clearly see from this graph, that starting from a redshift $z = 2$ all gas phases are turbulent at the scale $l_{min} = 15.6\,\mathrm{kpc\ h^{-1}}$. We also see that the amount of turbulence in terms of eddy turnover times is higher in regions of higher temperature and therefore highest in the cluster gas.

Another important measure for turbulence is the turbulent Mach number introduced in section 5.3.2. Like the eddy turnover time, the turbulent Mach number is

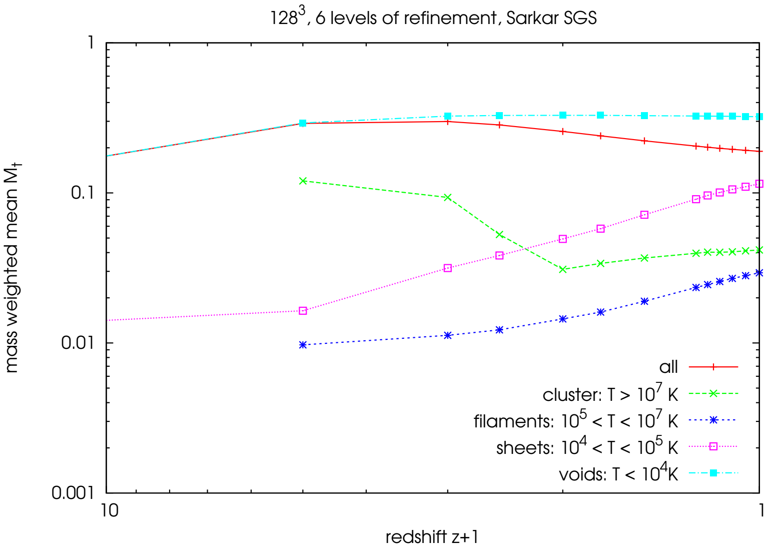

Figure 9.5: Mean turbulent Mach number at a scale $l_{min} = 15.6\,\mathrm{kpc\ h}^{-1}$ for gas phases of different temperature over time.

scale dependent

$$M_t(l) = \frac{q(l)}{c_s}. \tag{9.13}$$

In figure 9.5 we plot the mean mass weighted turbulent Mach number characteristic for the scale of our analysis $l_{min} = 15.6\,\mathrm{kpc\ h}^{-1}$ making again use of our local Kolmogorov hypothesis. It is evident that the turbulence at l_{min} is subsonic in all gas phases during the whole time of the simulation. At redshift $z = 0$ the average turbulent Mach number is ≈ 0.2. If the amount of turbulence would be equal in each gas phase one would expect the turbulent Mach number to scale $\sim 1/c_s \sim 1/\sqrt{T}$. However this is not the case. The cluster gas is much more turbulent than estimated by this simple scaling relation; in fact there is more turbulent energy compared to internal energy in the hottest gas phase than in the WHIM, although there is a substantial drop of the turbulent Mach number between redshift $z = 1 - 2$. The drop in turbulent Mach number is presumably due to heating of the cluster gas during a phase of major mergers at that time. In the next section, we will present some further evidence for this interpretation.

9.2.4 Scaling of turbulent energy

In chapter 7 we studied the scaling of the turbulent energy with the resolution and were able to show that the scaling of turbulent energy in our simulations of driven turbulence actually follows the Kolmogorov scaling law. In this section we repeat

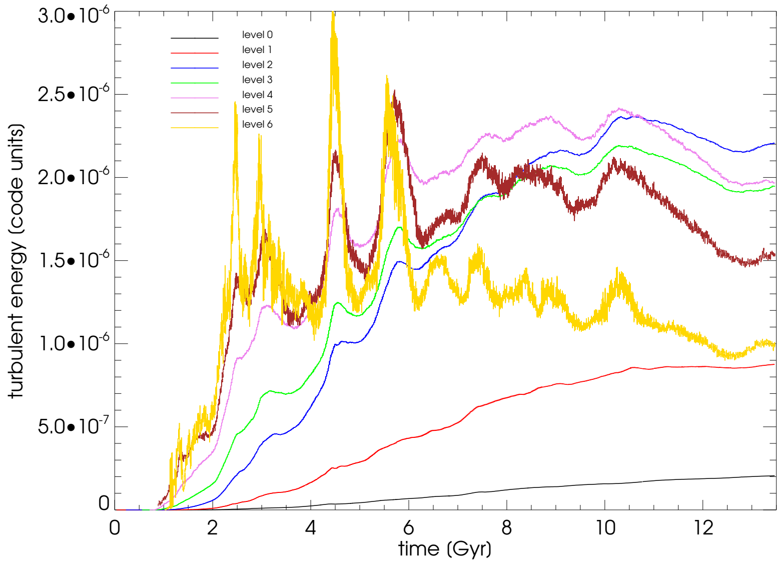

Figure 9.6: Time development of mean turbulent energy over time for each level of refinement.

this analysis for our cluster simulation. Figure 9.6 shows the time development of the mass weighted mean turbulent energy for every level of our AMR simulation. We see from the plot, that the turbulent energy on the higher levels (meaning at smaller scales) is higher at times $t < 6\,\mathrm{Gyr}$. Later this picture changes, but not completely. For example the turbulent energy on level 4 stays above the turbulent energy of level 3 for the whole simulation time. Also striking are the high fluctuations in the time $2\,\mathrm{Gyr} < t < 6\,\mathrm{Gyr}$, which correspond to a redshift $z = 3 - 1$ of the turbulent energy at the smaller scales. This is also the time when the turbulent Mach number inside the cluster drops significantly (see last section), so we can interpret these high fluctuations as further evidence for violent major mergers, that happen at that time, producing turbulent energy, which is then dissipated into internal energy heating up the cluster gas. However at the time $t > 13\,\mathrm{Gyr}$, the simulation seems to reach some kind of stable state, similar to what is found in driven turbulence simulations. We therefore can compute mean turbulent energies by averaging the turbulent energy from $t = 13\,\mathrm{Gyr}$ to the end of the simulation and plot them against the grid length scale of the associated level. The result (in terms of the turbulent velocity) can be seen in figure 9.7. It is obvious that this is no Kolmogorov scaling. However, we do not expect to see a Kolmogorov scaling again, since, as explained in the last section, we assume the resolved regions to be non-Kolmogorov anyway. Still the result is interesting, showing a peak in the turbulence around $100\,\mathrm{kpc\ h}^{-1}$ and a drop off towards higher and smaller scales. Also shown in the figure are power-law fits, which gave a scaling of $q \sim l^{-0.78}$ for scales bigger than $100\,\mathrm{kpc\ h}^{-1}$ and a scaling

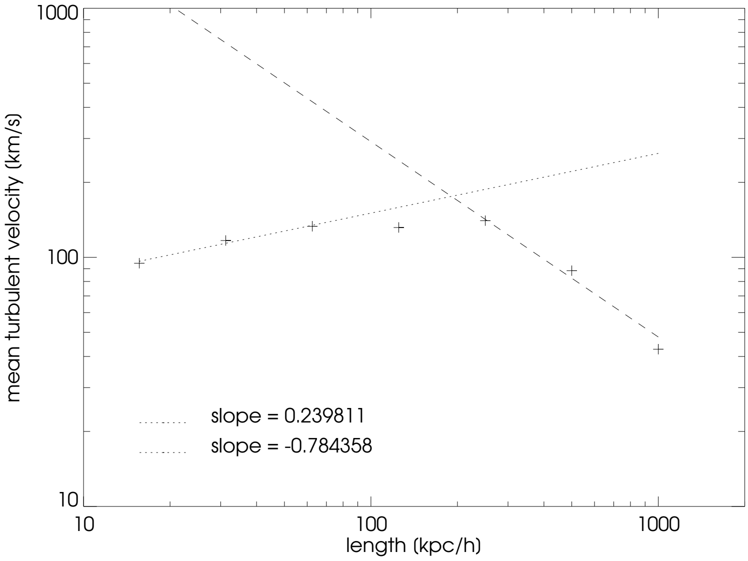

Figure 9.7: Scaling of mean turbulent energy. The dotted line is a fit showing the scaling behavior of turbulent energy below 100 kpc h^{-1}, the dashed line is a fit showing the scaling behavior above 100 kpc h^{-1}.

of $q \sim l^{0.24} \sim l^{1/4}$ for smaller scales. If one wants to interpret this result in terms of a turbulent cascade, one could say that up to a length scale of 100 kpc h^{-1}, energy is injected into the system, cascading down towards smaller scales with a scaling behavior $q \sim l^{1/4}$ flatter than expected for a Kolmogorov scaling with $q \sim l^{1/3}$. But, assuming our local Kolmogorov hypothesis holds, it would follow, that below the grid resolution of 15.7 kpc h^{-1} the cascade should be Kolmogorov again. Of course a interpretation like this is highly speculative; much more data on turbulence in cluster simulations is necessary to show that the observed power-law scalings are real indeed.

9.2.5 Radial profiles of the cluster

As mentioned in section 9.1.1, the simulation is centered around a galaxy cluster with a virial mass of $M_{vir} = 5.49 \times 10^{14}\,\mathrm{M}_\odot\ h^{-1}$ and a virial radius of $R_{vir} = 1.33\,\mathrm{Mpc}\ h^{-1}$ for both simulations, which center is identified using the HOP algorithm. In the following we present plots of radial profiles of several quantities around the center of this cluster (figure 9.8(a)-9.9(c)) obtained by using a modified version[4] of the `enzo_anyl` tool, which is part of the public Enzo release.

The plots show the mass weighted average values at radius r of temperature $T(r)$

---

[4] We modified `enzo_anyl` to allow plotting of SGS model quantities like the turbulent velocity.

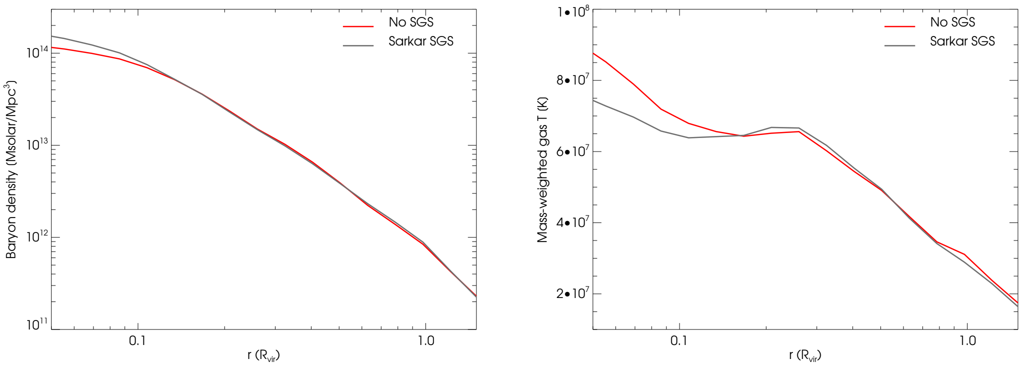

(a) Gas density. (b) Temperature.

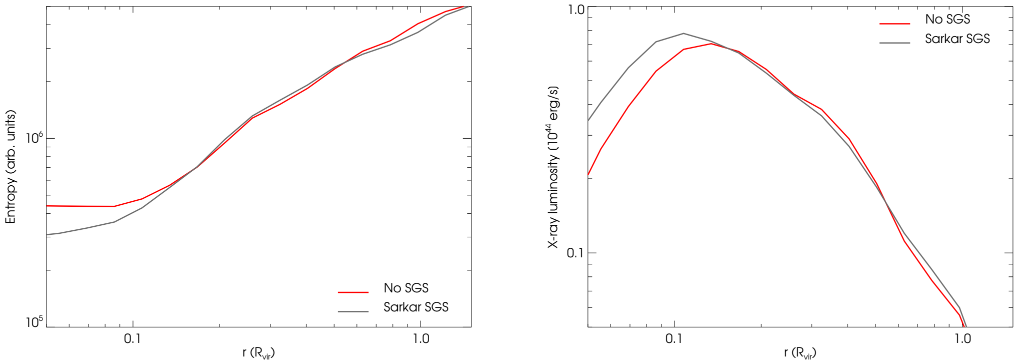

(c) Entropy. (d) X-ray luminosity.

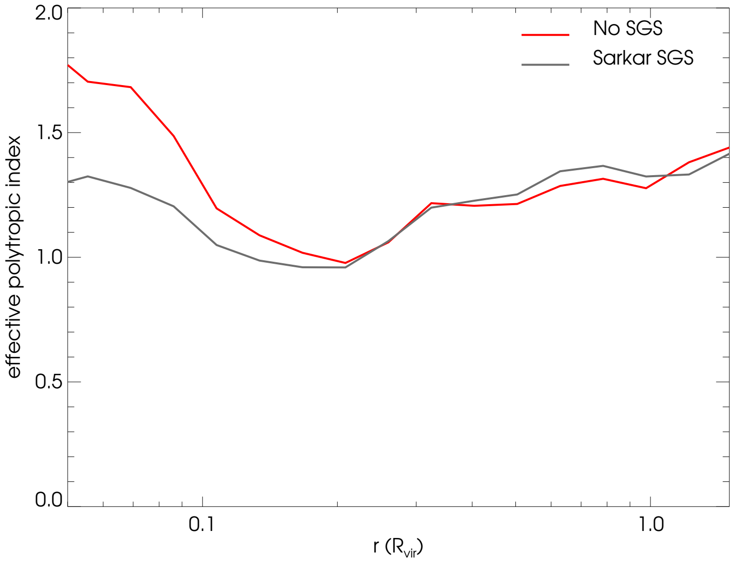

(e) Radial profile of effective polytropic index $n_{\mathrm{eff}}(r)$.

Figure 9.8: Radial profiles of several thermodynamic quantities around the center of the galaxy cluster. The results for the simulation with and without Sarkar SGS model are plotted in red and black respectively.

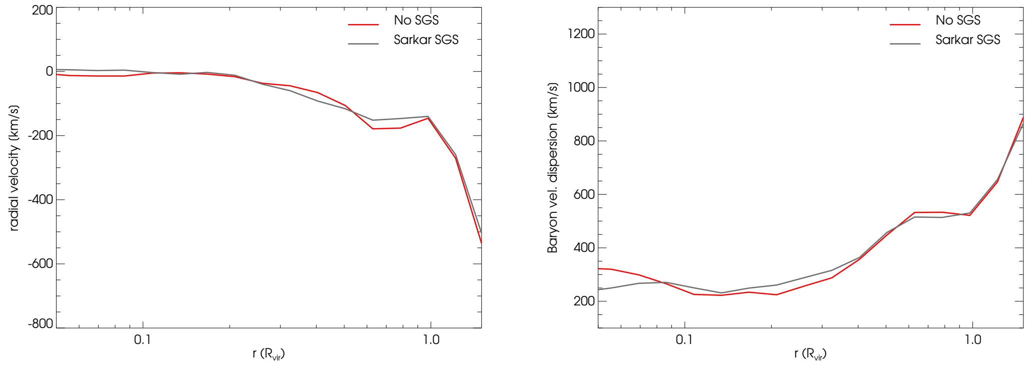

(a) Radial velocity. (b) Radial averaged velocity dispersion.

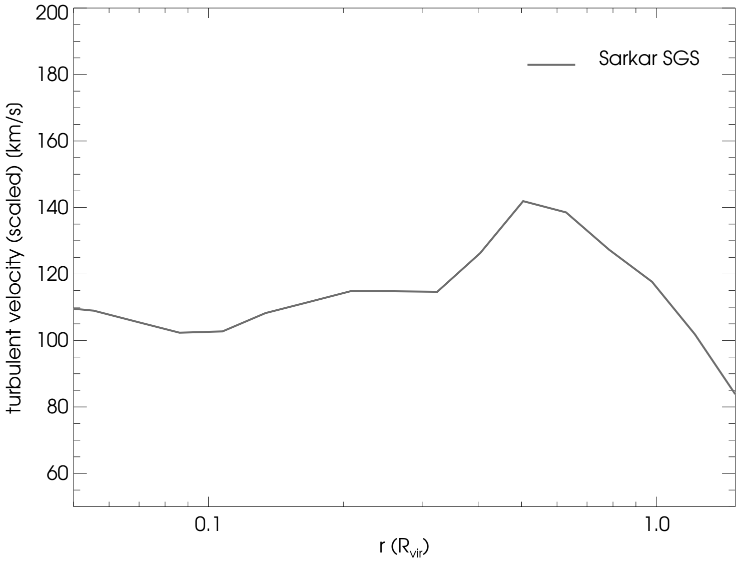

(c) Scaled turbulent velocity.

Figure 9.9: Radial profiles of several velocity related quantities around the center of the galaxy cluster. The results for the simulation with and without Sarkar SGS model are plotted in red and black respectively.

in Kelvin, the density[5] $\rho(r)$ in $\mathrm{M}_\odot/\mathrm{Mpc}^3$, the scaled turbulent velocity according to equation (9.12) $v_t(r)$ in km s^{-1}, the radial component of the resolved velocity $v_r(r)$ in km s^{-1}, the entropy K in code units, which is defined as[6]

$$K = \frac{T}{\rho^{\gamma-1}} \tag{9.14}$$

with $\gamma = 5/3$, the x-ray luminosity $L_X \sim \rho^2 T^{1/2}$ and the radially averaged velocity dispersion, which is defined as the standard deviation of the velocity averaged over a spherical shell as

$$\sigma(r) = \frac{\sum_i m_i (v_i - \langle v(r) \rangle)^2}{\sum_i m_i} \tag{9.15}$$

where $\langle v(r) \rangle = \frac{\sum_i m_i}{\sum_i m_i}$ is the mass weighted mean value of velocity in the spherical shell at radius $r \pm \delta r$.

At first it is apparent from these plots that, except for the radial component of the resolved velocity, the run with SGS model only shows significant deviations from the run without SGS model in the cluster core at $r < 0.1\ R_{vir}$. However since `enzo_anyl` proved not to be robust for $r < 0.07\ R_{vir}$ (Iapichino and Niemeyer, 2008), one cannot use the values obtained by these plots for a consistent analysis of the cluster core; this will be done in the next chapter using a different tool. Nevertheless the general trend from these plots is, that the SGS model lowers the entropy in the core, which leads to a higher density and a lower temperature in the center of the cluster. Since the X-ray luminosity is proportional to ρ^2, it is higher in the cluster core of the simulation with SGS model. Looking more precisely at the radial profile of entropy (fig. 9.8(c)), one can also see that in the simulation without the SGS model, the entropy inside the core of the cluster $r > 0.1\ R_{vir}$ is basically constant, which suggests that the gas is adiabatic there. With the SGS model this is not the case; the entropy is falling steadily towards the center of the core.

The last observation can be discussed more quantitatively in terms of polytropic processes. A polytropic process is defined as a process, where

$$\frac{T}{\rho^{n-1}} = const., \tag{9.16}$$

where n is called the polytropic index. By reversing that logic we can compute an effective polytropic $n_{\mathrm{eff}}(r)$ index by demanding that

$$\frac{d}{dr}\left(\frac{T}{\rho^{n_{\mathrm{eff}}(r)-1}}\right) = 0, \tag{9.17}$$

---

[5] The density is not mass weighted .

[6] This definition of entropy is often used in literature on galaxy clusters (Voit, 2005; Iapichino and Niemeyer, 2008).

which leads to

$$n_{\text{eff}}(r) = \frac{\rho}{T}\frac{\frac{dT}{dr}}{\frac{d\rho}{dr}} + 1 = \frac{d\ln\rho}{d\ln T} + 1. \tag{9.18}$$

In figure 9.8(e) we show a plot of the radial dependence of the effective polytropic index for our two simulations with and without SGS model. We see that the polytropic index in the simulation without SGS model is $n_{\text{eff}} \approx 1.7$, which is near to the adiabatic case $n_{\text{eff}} \approx 5/3$, as expected. The simulation with SGS model is clearly not adiabatic, with $n_{\text{eff}} \approx 1.3 \approx 4/3$ in the center. We also note that at a radius $r \approx 0.2\ R_{vir}$, the gas behaves basically isothermal, which can also be seen in the temperature profile (figure 9.8(b)). At an even bigger distance from the core $r > 0.2\ R_{vir}$, the cluster gas in both simulations behaves similarly, with a polytropic index rising from $n \approx 1.3$ to $n \approx 1.4$. If we compute an average polytropic index over the region $0.05\ R_{vir} < r < 1.0\ R_{vir}$ we get $n_{\text{eff}} = 1.27$ and $n_{\text{eff}} = 1.18$ for the simulation without and with SGS respectively. It is interesting to compare these values with results from observations. For example Markevitch et al. (1998) found that they could fit their measured temperature profiles with a polytropic index of $n = 1.2 - 1.3$, which would fit reasonably well to our average values. However, Pratt and Arnaud (2002) claim that $n = 1.07 \pm 0.1$ is the best fit to their observed temperature profile, and therefore state, that the whole cluster can be seen as nearly isothermal. But newer measurements by Vikhlinin et al. (2006) now reveal, that the temperature profile cannot be fitted by a single polytropic index in agreement with our analysis. Vikhlinin et al. (2006) also find a broad plateau of temperature at $r = 0.2\ R_{vir}$ in most of their clusters, however all their temperature profiles show a decline of temperature towards the center of the cluster at $r < 0.2\ R_{vir}$, a so-called "cool core". This feature could neither be reproduced by the simulation without SGS nor with SGS. It seems like including turbulence alone in a cluster simulation cannot be a solution to the "cool core" problem.

The radial resolved velocity is not changed significantely by the SGS model, but comparing this plot with the radial profile of the turbulent velocity the following picture emerges: From a radius $r > R_{vir}$ material is falling onto the cluster, being decelerated strongly at the virial radius $r = R_{vir}$ (see drop of radial velocity at this point in figure 9.9(a)). This deceleration leads to a steady rise in turbulent energy at $r < R_{vir}$ up to a peak at $r = 0.5\ R_{vir}$ followed by a drop of to a quite stable value of $\sim 110\,\text{kms}^{-1}$ in the region $r < 0.3\ R_{vir}$. One might want to compare these value to the velocity dispersion, however these values are not comparable directly. The turbulent velocity depicted in the plot is computed for the characteristic scale $15.7\,\text{kpc h}^{-1}$, which is constant with the radius. The velocity dispersion is the deviation of velocity in a spherical shell at radius r, so the characteristic scale of σ is basically the circumference of this shell $l = 2\pi r$, which is of course not independent of the radius. Therefore we cannot interpret the value of σ in the same local sense as we can do for the other quantities. We therefore doubt that it is useful to draw conclusions about the local nature of turbulence from a plot like fig. 9.9(b), as is often done in the literature (e.g. (Norman and Bryan, 1999)).

9.2.6 Spatial distribution of turbulent energy

To investigate the time development of the spatial distribution of turbulent energy, we generated slices of density and turbulent energy with the graphical analysis tool VisIt. The slices are taken around the place of formation of our main galaxy cluster and show a region of size $6.4 \times 6.4\,\mathrm{Mpc}\ \mathrm{h}^{-1}$. Overlayed onto the slices are density contour lines and a vector field showing the strength and direction of the velocity. In the density slice at redshift $z = 0.15$ (figure 9.10(a)), we can see from the velocity vectors that material is falling onto the cluster along filament from the lower left and from the upper right corner. But from the upper right corner we do not have a smooth inflow of matter, instead two small clumps are approaching. Over the course of the simulation these two clumps merge with the main cluster (figure 9.10(c)-9.10(c)) and are assimilated completely at redshift $z = 0$. Only the velocity field still shows some disturbance due to the infalling clumps.

In the slice of the turbulent energy (figure 9.10(b)) at $z = 0.15$, we see a hot spot of turbulent energy in the center of our cluster, which is due to a former major merger. The turbulent energy produced due to this merger is declining (figure 9.10(d)-9.11(d)) and at redshift $z = 0$ it is presumably dissipated into internal energy completely, so there is only little turbulent energy left at the center of the cluster.

However the two approaching clumps will drive turbulence again in the cluster. Thereby the left clump can be identified in the turbulent energy slice at $z = 0.15$ (figure 9.10(b)) as a ring-like structure, showing that turbulence is not produced in the center of the infalling clump, but is presumably produced at the front (behind a bow shock) and in the wake of the infalling material. But the right clump only shows some turbulence production in its wake, which might be due to its smaller size and smaller velocity. However, on their way towards the main cluster, both clumps develop a hot spot of turbulent energy (figure 9.10(d)-9.11(b)). The hot spot of turbulent energy can even be identified after the two clumps have merged with the main cluster (figure 9.11(d)) and are not visible in the density slice (figure 9.11(c)) anymore. In this sense, the distribution of turbulent energy traces the local merging history of a galaxy cluster until it is dissipated into heat completely. Also the merging of the two small clumps with the main cluster drives turbulence only in its outer rim, showing that smaller mergers might only be able to drive turbulence in the outer regions ($r > R_{vir}$) of a cluster. But turbulence is sustained for a longer time in a galaxy cluster than one might expect from just looking at density development.

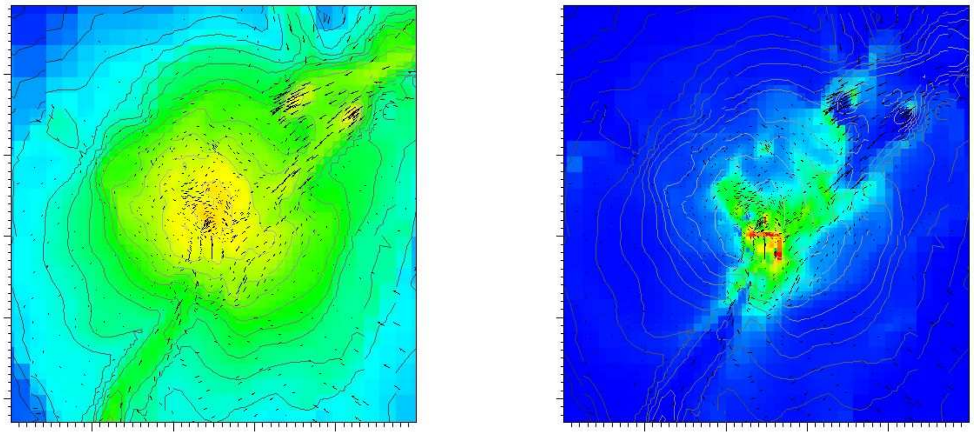

(a) $z = 0.15$.

(b) $z = 0.15$.

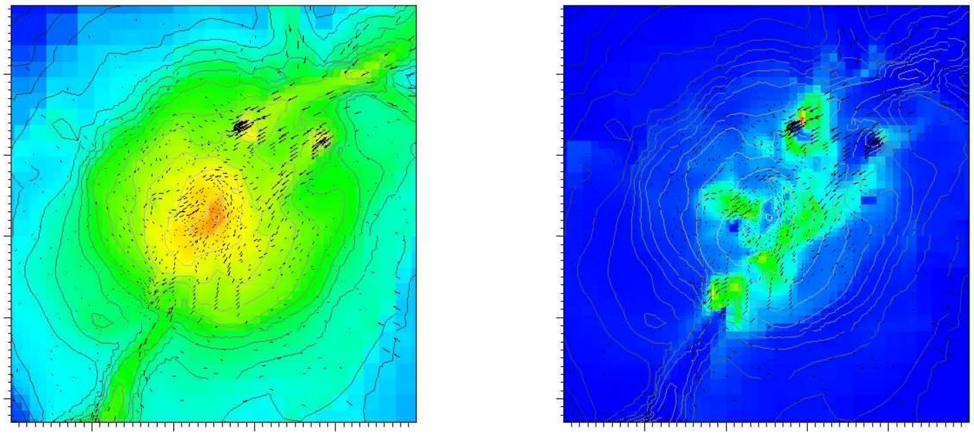

(c) $z = 0.1$.

(d) $z = 0.1$.

Figure 9.10: Slices of density (left) and turbulent energy at a length scale of 15.6 Mpc h^{-1} (right) at varying redshifts z. The color coding shows both quantities in code units using a logarithmic scaling. The overlayed contours show density and the overlayed vector field depicts the strength and direction of the baryonic velocity field in code units using a linear scale. The slices show a region of $6.4 \times 6.4\,\mathrm{Mpc}\ \mathrm{h}^{-1}$.

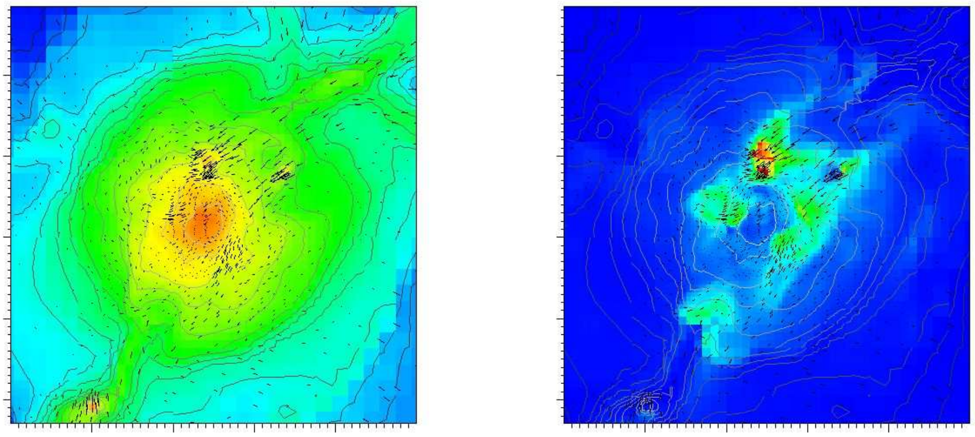

(a) $z = 0.05$.

(b) $z = 0.05$.

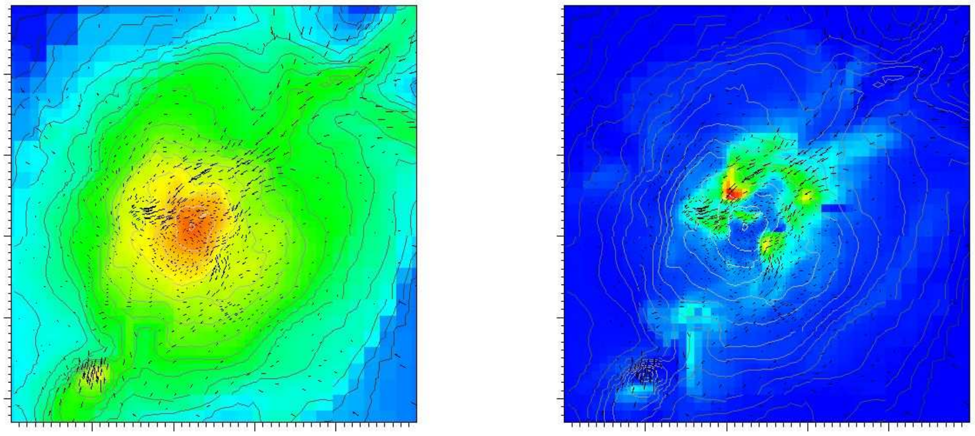

(c) $z = 0$.

(d) $z = 0$.

Figure 9.11: Slices of density (left) and turbulent energy at a length scale of 15.6 Mpc h^{-1} (right) at varying redshifts z. The color coding shows both quantities in code units using a logarithmic scaling. The overlayed contours show density and the overlayed vector field depicts the strength and direction of the baryonic velocity field in code units using a linear scale. The slices show a region of 6.4×6.4 Mpc h^{-1}.

(a) General quantities.

Run	m_{bar} [10^{12} M$_\odot$]	ρ [10^{14} M$_\odot$ Mpc^{-3}]	T [10^7 K]	K [$10^5 \times$ code units]	σ [km s^{-1}]
no SGS	2.73	0.996	7.88	4.40	200
SGS	3.37	1.29	6.99	3.38	257

(b) Resolved and thermal pressure.

Run	p_{th}/ρ [10^{16} cm^{2}s^{-2}]	p_{res}/ρ [10^{14} cm^{2}s^{-2}]	$\frac{p_{res}}{p_{th}+p_{res}}$ [%]
no SGS	1.05	1.34	1.25
SGS	0.936	2.20	2.30

(c) SGS quantities.

Run	p_{turb}/ρ [10^{14} cm^{2}s^{-2}]	ϵ [10^{-5} cm^{2}s^{-3}]	Σ [10^{-5} cm^{2}s^{-3}]
no SGS	0.0	0.0	0.0
SGS	0.380	3.06	2.92

Table 9.3: Mass weighted values of some quantities, calculated within a sphere with $R = 0.1\ R_{vir}$ centred at the cluster center at z=0.

9.2.7 Cluster core analysis

As mentioned we couldn't use the `enzo_anyl` tool to compute average values of thermodynamic quantities of the cluster core. Instead we analyzed the cluster core using the interactive parallel visualization and graphical analysis tool VisIt[7]. Using this tool we computed several mass-weighted averaged quantities within a sphere of radius $R = 0.1\ R_{vir}$, centered at the cluster center. The results of this analysis are summarized in tables 9.3(a)-9.3(c). The table lists as general quantities of the simulations the baryonic mass m_{bar} inside the chosen sphere, the density ρ, the temperature T, the entropy $K = \frac{T}{\rho^{\gamma-1}}$ with $\gamma = 5/3$ and the baryonic velocity dispersion $\sigma = \frac{\sum_i m_i (v_i - \langle v \rangle)^2}{m_{bar}}$ at the length scale $l = 0.1\ R_{vir} = 133\,\mathrm{kpc\ h^{-1}}$. According to Voit (2005) entropy is the most important quantity to look at, because it determines the structure of the intracluster medium and it records the thermodynamic history of the cluster's gas; the temperature and density are just manifestations of the entropy. We find that the ratio of the entropies in the cluster core of the two simulations (in the following 1 is used to subscript quantities of the run without SGS model, 2 subscripts quantities of the simulation with SGS model) is

---

[7] Freely available from https://wci.llnl.gov/codes/visit.

$$\frac{K_1}{K_2} = 1.30 = \left(\frac{\rho_1}{\rho_2}\right)^{-1} = \left(\frac{\sigma_1}{\sigma_2}\right)^{-1}. \tag{9.19}$$

Since $\frac{K_1}{K_2} = \left(\frac{T_1}{T_2}\right)\left(\frac{\rho_1}{\rho_2}\right)^{-2/3}$ by definition, this yields

$$\left(\frac{T_1}{T_2}\right) = \left(\frac{\rho_1}{\rho_2}\right)^{-1/3} = 1.09, \tag{9.20}$$

which is roughly fulfilled, since from the data directly we get $T_1/T_2 = 1.13$. So temperature and density are really just manifestations of entropy, but also the velocity dispersion of the baryonic gas in the cluster core seems to be directly connected to the entropy. Because of this, the velocity dispersion at a length scale of $l = 0.1\ R_{vir}$ in the simulation with the SGS model is significantely higher than in the simulation without SGS model.

In table 9.2(b) we list the thermodynamic pressure p_{th} and the resolved pressure, which is defined as

$$p_{res} = \frac{1}{3}\rho\sigma^2, \tag{9.21}$$

and the ratio between resolved and thermodynamic pressure. We see that, in the case of the SGS model simulation, the ratio of resolved to thermal pressure is nearly twice as high compared to the simulation without SGS model, since density and velocity dispersion are higher in the core when using the SGS model.

Listed in table 9.2(c) is also the turbulent pressure, defined as

$$p_{res} = \frac{1}{3}\rho q^2, \tag{9.22}$$

where q^2 is related to the velocity fluctuations at grid length scale $l = 15.7\,\mathrm{kpc\ h}^{-1}$. So directly comparing or adding the resolved pressure to the turbulent pressure is not useful, since both are related to the deviations of the velocity on different length scales. However, the ratio of turbulent production Σ to turbulent dissipation ϵ in the core of the cluster is interesting

$$\frac{\Sigma}{\epsilon} = 0.95, \tag{9.23}$$

showing that we are actually in a regime of near equilibrium of production and dissipation of turbulent energy, a sign that a turbulent cascade has established.

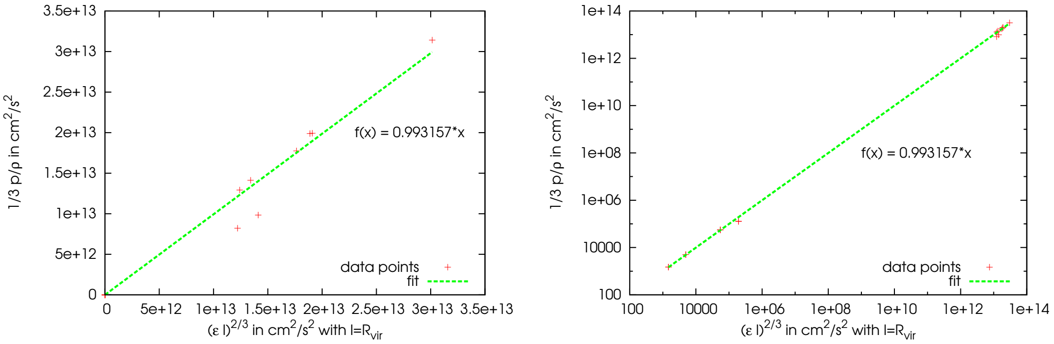

(a) Linear scaling.

(b) Logarithmic scaling.

Figure 9.12: Plot of turbulent pressure over density versus turbulent dissipation in the center of the cluster core for different parameters of the SGS model.

9.2.8 Influence of SGS parameters on cluster core

In an attempt to better understand the influence of the SGS model on the thermodynamic properties of the cluster core, we conducted a series of simulations with different parameters for the SGS model. Because of our restricted CPU budget we could not afford to do these simulations with the full 128^3 root grid resolution, rather we were only able to do these studies using a root grid resolution of 32^3 grid cells and 32^3 N-body particles. In analogy to the high resolution simulation, we also nested a static child grid inside the root grid, with 32^3 cells and 32^3 N-body particles. The mass of each particle in this grid was $5.8 \times 10^{11}\,\mathrm{M}_\odot\ \mathrm{h}^{-1}$, so the resolution of the gravitational potential due to dark matter was much lower in these runs. We allowed adaptive grid refinement from level $l = 2$ to $l = 8$ in a volume of $38.4\,\mathrm{Mpc\ h}^{-1}$ inside this grid, so the effective resolution of the baryonic component and all the other parameters were equal to the high resolution runs. The galaxy clusters that formed in these simulations had a virial mass of roughly $M_{vir} = 6.9 \times 10^{14}\,\mathrm{M}_\odot\ \mathrm{h}^{-1}$ and a virial radius of $R_{vir} = 1.27\,\mathrm{Mpc\ h}^{-1}$.

As parameters we chose all combination of $C_\nu = (0.0, 0.05)$, $C_\lambda = (0.0, -0.2)$, $C_{\mathbb{D}} = (0.0, 0.4)$ and $C_p = (0.0, 1.0)$[8], which gave use 16 combinations altogether. In complete analogy to the high resolution runs we analyzed the average values of thermodynamic quantities of the cluster core. Albeit one interesting preliminary result emerged. By plotting the average values of the turbulent pressure over the average value of turbulent dissipation in the cluster core (figures 9.12(a),9.12(b)), we found that they seem to be related as

$$\langle \frac{p_t(l_{min})}{\rho} \rangle = C(\langle \epsilon \rangle R_{vir})^{2/3}, \tag{9.24}$$

---

[8] Setting $C_p = 0.0$ means switching off the influence of the turbulent pressure in the momentum equation.

where $\langle\rangle$ means the mass weighted average over the cluster core $r < 0.1\ R_{vir}$, $l_{min} = 15.6\,\mathrm{kpc\ h^{-1}}$ and $R_{vir} = 1.27\,\mathrm{Mpc\ h^{-1}}$. The constant C can be found from a linear fit to be $C \approx 1$ (see fit in figures 9.12(a),9.12(b)). If we use again our scaling relation for the turbulent velocity (9.12), we get with $\langle \frac{p_t(l_{min})}{\rho} \rangle = \langle q^2(l_{min}) \rangle$ and $C = 1$

$$\langle q^2(l) \rangle = \left(\frac{R_{vir}}{l_{min}} \right)^{2/3} \langle \epsilon \rangle^{2/3} l^{2/3} \tag{9.25}$$

If we assume, that the value of $\frac{R_{vir}}{l_{min}}^{2/3} = 18.8$ is universal, we get for cluster core turbulence the relation

$$\langle q^2(l) \rangle = 18.8 \langle \epsilon \rangle^{2/3} l^{2/3}. \tag{9.26}$$

In this sense, we can interpret $C_{k,core} = 18.8$ as a Kolmogorov constant for the cluster core turbulence, which is more than 10 times higher than what is found for the Kolmogorov constant in simulations of incompressible turbulence.

10 Summary and Conclusions

Turbulence is often invoked in astrophysics to explain phenomena, which are not understood. However, studies that quantify the real impact of turbulence in astrophysical environments in general, or especially for the formation of galaxy clusters, are not available. One reason for this is obviously the lack of an accepted theory of compressible and/or supersonic and/or selfgravitating turbulence. A second reason is that the models used to describe numerically the influence of turbulence (so-called large-eddy-simulations) are based on the notion of filtering the fluid dynamic equations at a specific length scale, which is incompatible with adaptive grid codes used to study astrophysical phenomena.

The aim of this work was to address the second problem, thereby developing, implementing, and applying a new numerical scheme for modeling turbulent flows over a great range of length scales suitable to treat astrophysical flows in galaxy cluster cores or star forming regions. Because the cosmological fluid code Enzo uses blockstructured adaptive mesh refinement in combination with a low dissipative PPM-Solver, it was a natural choice to implement our ideas into this code.

Still, great technical and numerical difficulties had to be circumvented. Nevertheless, we could finally show that the idea of our ϵ-based approach to correct the velocity and energy fields at grid refinement/derefinement according to local Kolmogorov scaling can produce consistent results in simulations of driven turbulence. We demonstrated that energy conservation and the scaling of turbulent energy in our adaptive simulations is consistent with static grid simulations.

Motivated by these results, we then attempted to use our new numerical scheme in simulations of galaxy cluster formation. Two high resolution runs of galaxy cluster formation, one with and one without a turbulence model, have been conducted to explore the influence of turbulence modeled with our scheme on the formation of galaxy clusters. From the analysis of these simulations, we conclude the following:

- Our turbulence model seems to have no significant influence on the mass fractions of different gas phases of the ICM.

- The time development of turbulent energy in the simulation suggests that basically all gas phases of the intracluster medium had enough time to develop a turbulent cascade. In fact, we could show that our model seems to be near an equilibrium of production and dissipation of turbulence, especially in the cluster core.

- The turbulence at a length scale of galaxies ($\approx 10\,\mathrm{kpc\ h^{-1}}$) is subsonic, and the average turbulent Mach number at these scale is found to be 0.2 at redshift $z = 0$.

- In the beginning of galaxy cluster formation great fluctuations of turbulent energy can be seen, suggesting that violent merging can produce a substantial amount of turbulence.

- Minor mergers can drive turbulence only at the outer rim ($r > R_{vir}$) of the galaxy cluster. The spatial distribution of turbulent energy traces the local merging history of a galaxy cluster until the turbulent motions are dissipated into heat completely.

- From the scaling properties of turbulent energy it seems that energy is injected at a scale of $\approx 100\,\mathrm{kpc\ h^{-1}}$ cascading down to smaller scales. From the radial profile of our cluster we found a peak of turbulent energy at $r = 0.5\ R_{vir}$, probably produced by the infall and strong deceleration of material, when it hits the virial boundary of the cluster.

- From the radial profiles of several thermodynamical quantities of the galaxy cluster it is evident, that only inside the core ($r < 0.1\ R_{vir}$) can one find a significant influence of our turbulence model. The radial profile of the effective adiabatic index shows that the influence of the turbulent model can be described as a kind of cooling, leading to lower entropy, lower temperature, and therefore higher gas density and higher velocity dispersion in the core. "Cooling" due to turbulence does not lead to an overcooling problem, but it is not strong enough to explain the cool cores of galaxy clusters.

The last result begs the question of how turbulence would influence a simulation of cluster formation including cooling. If there is no nontrivial interaction between cooling and the turbulence model, our results indicate that turbulence would even enhance the overcooling problem in the core. So suggesting turbulence as a heating mechanism that prevents galaxy cluster cores from overcooling seems to be problematic. Nevertheless more simulations of galaxy clusters, including different physics have to be carried out to confirm our results.

Interestingly preliminary results from low resolution simulations suggest, that turbulent velocity in the cluster core obeys a Kolmogorov scaling law with a Kolmogorov constant more than 10 times higher than in incompressible simulations. Whether this finding is only a feature of our SGS model or a universal feature of turbulence in the cluster core should be investigated in the future.

More attention should also be given to the fact that turbulent energy and thus unresolved turbulent velocity fluctuations are scale dependent. It is often claimed in the astrophysical literature that the amount of turbulence is a certain fraction of thermal energy or kinetic energy, without specifying the length scale for which this statement was made. In the spirit of Kolmogorov theory of turbulence, such statements are incomplete. This is especially apparent in our adaptive grid simulations, where different grid length scales at the same time are used to describe a flow. However, we have to note that the idea of scale dependent velocity fluctuations poses difficult conceptual problems. For example, the mass inside a certain radius r from the equation of hydrostatic equilibrium is, including turbulent pressure, also scale dependent[1]

$$M(r,l) = -\frac{r}{G}\left[R_s T_g\left(\frac{\partial \ln T_g}{\partial \ln r} + \frac{\partial \ln \rho_g}{\partial \ln r}\right) + \frac{q^2(l)}{3}\left(\frac{\partial \ln q^2(l)}{\partial \ln r} + \frac{\partial \ln \rho}{\partial \ln r}\right)\right], \tag{10.1}$$

a fact, which is often overlooked. Arguing that turbulent pressure might explain deviation from the mass found by estimates based on the hydrostatic equilibrium, is therefore not advisable.

Nevertheless, it might also come out, that the ideas of Kolmogorov and scale dependent velocity fluctuations are not useful in an astrophysical context. Within our work, we only showed how the influence of turbulence obeying basically Kolmogorov scaling can be numerically treated and what kind of results can be expected. We could not prove that turbulence in an astrophysical environment really can be described in this way. Theoretically, Kolmogorov derived his celebrated result assuming a forcing of turbulence restricted to the largest length scales, so that in the limit of infinite Reynolds numbers an undisturbed cascade down to smaller scales can develop. However, gravity is a force acting on all length scales, in contradiction to the ideas of Kolmogorov and our turbulence model. A better understanding of selfgravitating turbulence is therefore extremely important for the future of turbulence research in general. That's why in the future comparisons between direct numerical simulations of selfgravitating gas and simulations with our subgrid model should be conducted. If these simulations support our SGS model (which would also show, that Kolmogorov scaling is more universal than theory suggests), we can be confident in saying, that with our FEARLESS ansatz we developed a unique tool for describing turbulence which aside from cluster physics will lead to many other applications in astrophysics.

---

[1] For a derivation see appendix G.

A Dimensional analysis

We want to write down the general equations of fluid dynamics in dimensionless form. Therefore we introduce the following dimensionless quantities

$$\begin{aligned} r_i^* &= \frac{r_i}{l_0} \Rightarrow \frac{\partial}{\partial r_i} = \frac{\partial}{\partial r_i^*}\frac{\partial r_i^*}{\partial r_i} = \frac{1}{l_0}\frac{\partial}{\partial r_i^*}, \\ v_i^* &= \frac{v_i}{v_0}, \\ t^* &= \frac{t}{l_0} \Rightarrow \frac{\partial}{\partial t} = \frac{\partial}{\partial t^*}\frac{\partial t^*}{\partial t} = \frac{1}{t_0}\frac{\partial}{\partial t^*}, \\ \rho^* &= \frac{\rho}{\rho_0}. \end{aligned}$$

Inserting these into the continuity equation (2.1) we get

$$\begin{aligned} \frac{\rho_0}{t_0}\frac{\partial}{\partial t^*}\rho^* + \frac{v_0\rho_0}{l_0}\frac{\partial}{\partial r_j^*}(v_j^*\rho^*) = 0 \mid \cdot \frac{l_0}{\rho_0 v_0}, \\ \underbrace{\frac{l_0}{v_0 t_0}}_{Sr}\frac{\partial}{\partial t^*}\rho^* + \frac{\partial}{\partial r_j^*}(v_j^*\rho^*) = 0. \end{aligned}$$

This derivation shows that solutions of the continuity equation are similar, if the Strouhal number $Sr = \frac{l_0}{v_0 t_0}$ is the same. Flows with a Strouhal number $Sr = 0$ are so called stationary flows. Nevertheless, the Strouhal number is most often set to one, by assuming $v_o = \frac{l_0}{t_0}$. Using the additional dimensionless quantities $p^* = \frac{p}{p_0}, \sigma_{ij}^* = \frac{\sigma_{ij}}{\sigma_0}, g^* = \frac{g}{g_0}$ in the momentum equation (2.2) yields

$$\begin{aligned} \frac{\rho_0 v_0}{t_0}\frac{\partial}{\partial t^*}(\rho^* v_i^*) + \frac{\rho_0 v_0^2}{l_0}\frac{\partial}{\partial r_j^*}(v_j^*\rho^* v_i^*) = -\frac{p_0}{l_0}\frac{\partial}{\partial r_i^*}p^* + \frac{\sigma_0}{l_0}\frac{\partial}{\partial r_j^*}\sigma_{ij}^* + \rho_0 g_0 \rho^* g_i^* \mid \cdot \frac{l_0}{\rho_0 v_0^2}, \\ \underbrace{\frac{l_0}{v_0 t_0}}_{Sr}\frac{\partial}{\partial t^*}(\rho^* v_i^*) + \frac{\partial}{\partial r_j^*}(v_j^*\rho^* v_i^*) = -\underbrace{\frac{p_0}{\rho_0 v_0^2}}_{Ma_{iso}^{-2}}\frac{\partial}{\partial r_i^*}p^* + \underbrace{\frac{\sigma_0}{\rho_0 v_0^2}}_{Re^{-1}}\frac{\partial}{\partial r_j^*}\sigma_{ij}^* + \underbrace{\frac{\rho_0 g_0 l_0}{\rho_0 v_0^2}}_{Fr^{-1}}\rho^* g_i^*. \end{aligned}$$

The occurring dimensionless numbers are the isothermal Mach number Ma_{iso}, which is related to the Euler number Eu or the Ruark number Ru like $Ma_{iso}^2 = Eu = Ru^{-1}$, the Froude number Fr, which is related to the Richardson number Ri like $Fr = Ri^{-1}$

and the Reynolds number Re. All these numbers measure the importance of the term they are related to compared to the nonlinear advection term $\frac{\partial}{\partial r_j^*}(v_j^* \rho^* v_i^*)$, e.g. for high Mach numbers, the pressure term $\frac{\partial}{\partial r_i^*} p^*$ becomes less and less important compared to the advection term; for high Reynolds numbers the stress term $\frac{\partial}{\partial r_j^*}\sigma_{ij}^*$ becomes less and less important compared to the advection term, and the equation shows more and more nonlinear behavior. For a newtonian fluid with

$$\sigma_{ij} \simeq \eta \frac{\partial v_i}{\partial r_j} = \frac{\eta_0 v_0}{l_0} \eta^* \frac{\partial v_i^*}{\partial r_j^*}, \tag{A.1}$$

where we introduced the dimensionless quantity $\eta^* = \frac{\eta}{\eta_0}$, we get $\sigma_0 = \frac{\eta_0 v_0}{l_0}$ and therefore we can express the Reynolds number[1] like

$$Re = \frac{l_0 \rho_0 v_0^2}{\eta_0 v_0} = \frac{\rho_0 l_0 v_0}{\eta_0}. \tag{A.2}$$

Playing the same game with the equation for the internal energy

$$\frac{\partial}{\partial t} \rho e_{int} + \frac{\partial}{\partial r_j} v_j \rho e_{int} = T \left(\frac{\partial}{\partial t} \rho s + \frac{\partial}{\partial r_j} v_j \rho s \right) - p \frac{\partial}{\partial r_j} v_j \tag{A.3}$$

using $e_{int}^* = \frac{e_{int}}{u_0}$ we get

$$\underbrace{\frac{l_0}{v_0 t_0}}_{Sr} \frac{\partial}{\partial t^*} \rho^* e_{int}^* + \frac{\partial}{\partial r_j^*} v_j^* \rho^* e_{int}^* = - \underbrace{\frac{p_0}{\rho_0 u_0}}_{Ga_1} p^* \frac{\partial}{\partial r_j^*} v_j^* + \underbrace{\frac{\sigma_0}{\rho_0 u_0}}_{Ga_2} \sigma_{ij}^* \frac{\partial}{\partial r_j^*} v_i^*.$$

The new dimensionless quantities that occur in the energy equation seem to have no name in the literature, but we will call them "Gamma1" (Ga1) and "Gamma2" (Ga2) for now, since they are related to the adiabatic coefficient. This can be seen by replacing $p_0 p^*$ according to equation

$$p_0 p^* = (\gamma - 1) \rho_0 u_0 \rho^* e_{int}^*, \tag{A.4}$$

which is valid for an an ideal, nonisothermal ($\gamma \neq 1$) gas. Doing this we get[2]

$$Sr \cdot \frac{\partial}{\partial t^*} \rho^* e_{int}^* + \frac{\partial}{\partial r_j^*} v_j^* \rho^* e_{int}^* = -(\gamma - 1) \rho^* e_{int}^* \frac{\partial}{\partial r_j^*} v_j^* + Ga_2 \cdot \sigma_{ij}^* \frac{\partial}{\partial r_j^*} v_i^*.$$

---

[1] We neglected the second viscosity ζ. In principle there exists a second Reynolds number $Re_2 = \frac{\rho_0 l_0 v_0}{\zeta_0}$.

[2] We cannot get rid of Ga2 in the same way, since therefore we would have to assume an equation relating $\sigma_0 \sigma_{ij}^*$ to the internal energy. But this would only be possible, if we would assume that the internal energy is a tensorial quantity, which is not the way how internal energy is defined normally.

For a selfgravitating fluid we even have on more dimensionless quantity, which appears, when we write down the dimesionless form of the Poisson equation of gravity

$$\underbrace{\frac{g_0}{4\pi G\rho_0 l_0}}_{C_G}\frac{\partial g_i^*}{\partial r_i^*} = \rho^*. \tag{A.5}$$

But this quantity C_G also seems to have no name in the literature (e.g. Durst, 2007).

B Properties of second order tensors

A second order tensor can be decomposed into a symmetric and an antisymmetric part in the following way

$$T_{ij} = \underbrace{\frac{1}{2}(T_{ij} + T_{ji})}_{\text{symmetric}} + \underbrace{\frac{1}{2}(T_{ij} - T_{ji})}_{\text{antisymmetric}} . \tag{B.1}$$

It can also be decomposed into an isotropic and deviatoric part by subtracting and adding the trace of the tensor like

$$T_{ij} = \underbrace{\frac{1}{n}\delta_{ij}T_{kk}}_{\text{isotropic}} + \underbrace{T_{ij} - \frac{1}{n}\delta_{ij}T_{kk}}_{\text{deviatoric, tracefree}} . \tag{B.2}$$

Combining these two relations yields the general decomposition

$$T_{ij} = \underbrace{\overbrace{\frac{1}{n}\delta_{ij}T_{kk}}^{\text{isotropic}} + \rlap{$\displaystyle\overbrace{\phantom{\frac{1}{2}\left(T_{ij} + T_{ji} - \frac{2}{n}\delta_{ij}T_{kk}\right) + \frac{1}{2}(T_{ij} - T_{ji})}}^{\text{deviatoric, tracefree}}$}\underbrace{\frac{1}{2}\left(T_{ij} + T_{ji} - \frac{2}{n}\delta_{ij}T_{kk}\right)}_{\text{symmetric, tracefree}}}_{\text{symmetric}} + \underbrace{\frac{1}{2}(T_{ij} - T_{ji})}_{\text{antisymmetric}} . \tag{B.3}$$

An interesting relation can be found when computing the contraction of a unsymmetric tensor $U_{ij} \neq U_{ji}$ with a symmetric tensor $V_{ij} = V_{ji}$

$$U_{ij}V_{ij} = \frac{1}{2}U_{ij}V_{ij} + \frac{1}{2}U_{ji}V_{ji} = \frac{1}{2}U_{ij}V_{ij} + \frac{1}{2}U_{ji}V_{ij} = \frac{1}{2}(U_{ij} + U_{ji})V_{ij}. \tag{B.4}$$

In analogy one finds for the contraction of an unsymmetric tensor U_{ij} with an antisymmetric tensor $W_{ij} = -W_{ji}$

$$U_{ij}W_{ij} = \frac{1}{2}(U_{ij} - U_{ji})W_{ij}. \tag{B.5}$$

C Derivation of the stress tensor for a newtonian fluid

We derive the stress tensor by considering the dissipation of a motionless fluid seen by a rotating observer. This derivation is different from what is found in the literature (eg. Greiner and Stock, 1991) and therefore presented here.

It is generally assumed that friction between fluid elements is proportional to the area of their surfaces. So in general the frictional or viscous force on a fluid element can be expressed like

$$F_{visc,i} = \oint_A \sigma'_{ij} n_j dA = \int_V \frac{\partial}{\partial r_j} \sigma'_{ij} dV. \tag{C.1}$$

This force leads to an irreversible rise of temperature in the fluid or an irreversible decrease of kinetic energy expressed by the equation for the dissipation[1]

$$\frac{\partial}{\partial t} E_{kin,visc} = - \int_V \sigma'_{ij} \frac{\partial}{\partial r_j} v_i dV. \tag{C.2}$$

For a motionless fluid ($v_i = 0$) and for a fluid with constant velocity ($\frac{\partial v_i}{\partial r_j} = 0$) this integral is zero. But also a rotating observer of a motionless fluid should not see a rise in the temperature of a fluid [2] that means

$$\int_V \sigma'_{ij} \frac{\partial}{\partial r_j} v_i dV = 0. \tag{C.3}$$

A rotating observer of a motionless fluid sees a velocity field of the form

$$v_i = \epsilon_{ijk} \omega_j r_k. \tag{C.4}$$

---

[1] See Landau and Lifschitz (1991).

[2] We do not consider here the a rigidly rotating fluid as is often done in the literature, because a rigidly rotating fluid is unphysical. This is so, because a rigidly rotating fluid can never fulfill the boundary condition $v_i = 0$. However, for a rotating observer, the boundary is also rotating, so that the boundary condition for a boundary at distance R is $v_i = \epsilon_{ijk} \omega_j R_k$ and there is no contradiction to the velocity field (C.4).

where ω_j is the angular velocity vector and r_k is the position vector. It can be shown that for such a velocity field the Jacobian is antisymmetric (Greiner and Stock, 1991), that means

$$\frac{\partial v_i}{\partial r_j} = -\frac{\partial v_j}{\partial r_i}. \tag{C.5}$$

Using this and equation (B.5) in equation (C.3) we get

$$\int\limits_V \frac{1}{2}\left(\sigma'_{ij} - \sigma'_{ji}\right)\frac{\partial}{\partial r_j} v_i dV = 0. \tag{C.6}$$

This relation can only be fulfilled if the stress tensor σ'_{ij} is symmetric

$$\sigma'_{ij} = \sigma'_{ji}. \tag{C.7}$$

For a newtonian fluid is it assumed that the stress tensor is proportional only to the first derivatives of the velocity field. Together with the requirement of symmetry the most general form of such a tensor is

$$\sigma'_{ij} = a\left(\frac{\partial v_j}{\partial r_i} + \frac{\partial v_i}{\partial r_j}\right) + b\delta_{ij}\frac{\partial v_k}{\partial r_k}. \tag{C.8}$$

Usually the trace is split off the first term and added to the second term so

$$\sigma'_{ij} = a\left(\frac{\partial v_j}{\partial r_i} + \frac{\partial v_i}{\partial r_j} - \frac{2}{3}\delta_{ij}\frac{\partial v_k}{\partial r_k}\right) + \left(\frac{2a}{3} + b\right)\delta_{ij}\frac{\partial v_k}{\partial r_k}. \tag{C.9}$$

Using the definitions $a = \eta$ and $\frac{2a}{3} + b = \zeta$ we get the form most common in literature

$$\sigma'_{ij} = 2\eta\left[\frac{1}{2}\left(\frac{\partial v_i}{\partial r_j} + \frac{\partial v_j}{\partial r_i}\right) - \frac{1}{3}\delta_{ij}\frac{\partial v_k}{\partial r_k}\right] + \zeta\delta_{ij}\frac{\partial v_k}{\partial r_k}. \tag{C.10}$$

D Fourier transform and structure functions

The continuous one-dimensional Fourier transform in k-space $F(k)$ of some function in x-space $f(x)$is defined like

$$F(k) = \frac{1}{\sqrt{2\pi}} \int\limits_{-\infty}^{\infty} f(x) e^{-ikx} dx \quad \text{(Fourier transform)}. \tag{D.1}$$

Using the Fourier transform on a function twice will produce the original function again, but mirrored at the origin. That's why one conventionally defines an inverse Fourier transform[1], that will generate the not mirrored original function again, when used on the Fourier transform of a function

$$f(x) = \frac{1}{\sqrt{2\pi}} \int\limits_{-\infty}^{\infty} F(k) e^{ikx} dx \quad \text{(inverse Fourier transform)}. \tag{D.2}$$

In three dimensions one defines the Fourier transform like

$$F(\boldsymbol{k}) = \frac{1}{(2\pi)^{3/2}} \iiint\limits_{-\infty}^{\infty} f(\boldsymbol{x}) e^{-i\boldsymbol{k}\boldsymbol{x}} dV, \tag{D.3}$$

$$f(\boldsymbol{x}) = \frac{1}{(2\pi)^{3/2}} \iiint\limits_{-\infty}^{\infty} F(\boldsymbol{k}) e^{i\boldsymbol{k}\boldsymbol{x}} dK. \tag{D.4}$$

In cartesian coordinates the kernel of the Fourier transform $e^{-i\boldsymbol{k}\boldsymbol{x}} = e^{-i(k_x x + k_y y + k_z z)}$ separates and so the three-dimensional Fourier transform of a function which separates in cartesian coordinates $f(\boldsymbol{x}) = a(x)b(y)c(z)$ is also separable

$$F(\boldsymbol{k}) = A(k_x)B(k_y)C(k_z) = \frac{1}{(2\pi)^{3/2}} \int\limits_{-\infty}^{\infty} a(x) e^{-ik_x x} dx \int\limits_{-\infty}^{\infty} b(y) e^{-ik_y y} dy \int\limits_{-\infty}^{\infty} c(z) e^{-ik_z z} dz.$$

Thats why we like to use cartesian coordinates when we are using Fourier transforms.

---

[1] Nature does not know about the inverse Fourier transform. If you have some optical device, which produces the Fourier transform of some image and you use it twice on your image you will get a mirrored image!

D.1 Fourier transform of a delta function

An important result can be derived by computing the inverse Fourier transform of the Fourier transform of a delta function

$$\begin{aligned}\delta(x-x_0) &= \frac{1}{\sqrt{2\pi}}\int\limits_{-\infty}^{\infty}\frac{1}{\sqrt{2\pi}}\int\limits_{-\infty}^{\infty}\delta(x-x_0)e^{-ikx}dxe^{ikx}dk\\ &= \frac{1}{2\pi}\int\limits_{-\infty}^{\infty}e^{-ikx_0}e^{ikx}dk = \frac{1}{2\pi}\int\limits_{-\infty}^{\infty}e^{ik(x-x_0)}dk.\end{aligned}$$

From this we get that the inverse Fourier transform of a constant is the delta function

$$\frac{1}{\sqrt{2\pi}}\int\limits_{-\infty}^{\infty}e^{ik(x-x_0)}dk = \sqrt{2\pi}\delta(x-x_0).$$

Taking the complex conjugate of this equation and making use of the fact that $\delta^*(x-x_0) = \delta(x-x_0)$ we get as a definition for the delta function

$$\delta(x-x_0) = \frac{1}{2\pi}\int\limits_{-\infty}^{\infty}e^{\pm ik(x-x_0)}dk. \tag{D.5}$$

Using this we can derive the astonishing result

$$\int\limits_{-\infty}^{\infty}f(x)dx = \sqrt{2\pi}F(0) \tag{D.6}$$

as can be seen from

$$\begin{aligned}\int\limits_{-\infty}^{\infty}f(x)dx &= \int\limits_{-\infty}^{\infty}\frac{1}{\sqrt{2\pi}}\int\limits_{-\infty}^{\infty}F(k)e^{ikx}dkdx = \frac{1}{\sqrt{2\pi}}\int\limits_{-\infty}^{\infty}F(k)\underbrace{\int\limits_{-\infty}^{\infty}e^{ikx}\,dx}_{2\pi\delta(k)}dk\\ &= \sqrt{2\pi}\int\limits_{-\infty}^{\infty}F(k)\delta(k)dk = \sqrt{2\pi}F(0).\end{aligned}$$

D.2 Convolution theorem

The Fourier transform of the product of two function in k-space is

$$\begin{aligned}
&\frac{1}{\sqrt{2\pi}}\int\limits_{-\infty}^{\infty} F(k)G(k)e^{ikx}dk = \\
&= \frac{1}{\sqrt{2\pi}}\int\limits_{-\infty}^{\infty} \frac{1}{\sqrt{2\pi}}\int\limits_{-\infty}^{\infty} f(x')e^{-ikx'}dx'\frac{1}{\sqrt{2\pi}}\int\limits_{-\infty}^{\infty} g(x'')e^{-ikx''}dx''e^{ikx}dk \\
&= \frac{1}{(2\pi)^{3/2}}\iiint\limits_{-\infty}^{\infty} f(x')e^{-ikx'}g(x'')e^{-ikx''}e^{ikx}dx'dx''dk \\
&= \frac{1}{(2\pi)^{3/2}}\iint\limits_{-\infty}^{\infty} f(x')g(x'')\underbrace{\int\limits_{-\infty}^{\infty} e^{-ik(x'+x''-x)}dk}_{2\pi\delta(x''-(x-x'))}\,dx'dx'' \\
&= \frac{1}{\sqrt{2\pi}}\int\limits_{-\infty}^{\infty} f(x')\int\limits_{-\infty}^{\infty} g(x'')\delta(x''-(x-x'))dx''dx' \\
&= \frac{1}{\sqrt{2\pi}}\int\limits_{-\infty}^{\infty} f(x')g(x-x')dx' = h(x).
\end{aligned}$$

The integral $h(x)$ is called convolution of the functions $f(x)$ and $g(x)$. So the convolution theorem says that

$$h(x) = \frac{1}{\sqrt{2\pi}}\int\limits_{-\infty}^{\infty} f(x')g(x-x')dx' = \frac{1}{\sqrt{2\pi}}\int\limits_{-\infty}^{\infty} F(k)G(k)e^{ikx}dk. \tag{D.7}$$

D.3 Autocorrelation and Wiener-Khinchin Theorem

The autocorrelation of a function is defined as[2]

$$h_{AC}(x) = \frac{1}{\sqrt{2\pi}}\int\limits_{-\infty}^{\infty} f^*(x')f(x+x')dx'. \tag{D.8}$$

---

[2] Note that with our definition of the Fourier transform we cannot define the autocorrelation function as $h_{AC}(x) = \frac{1}{\sqrt{2\pi}}\int_{-\infty}^{\infty} f(x')f^*(x+x')dx'$, because we could then not derive the Wiener-Khinchin theorem.

The Wiener-Khinchin Theorem states that

$$\frac{1}{\sqrt{2\pi}}\int\limits_{-\infty}^{\infty} f^*(x')f(x+x')dx' = \frac{1}{\sqrt{2\pi}}\int\limits_{-\infty}^{\infty} |F(k)|^2 e^{ikx}dk, \tag{D.9}$$

which can be proved in analogy to the convolution theorem

$$\begin{aligned}
&\frac{1}{\sqrt{2\pi}}\int\limits_{-\infty}^{\infty} f^*(x')f(x+x')dx' = \\
&= \frac{1}{\sqrt{2\pi}}\int\limits_{-\infty}^{\infty} f^*(x')\int\limits_{-\infty}^{\infty} f(x'')\delta(x''-(x+x'))dx''dx' \\
&= \frac{1}{\sqrt{2\pi}}\int\limits_{-\infty}^{\infty} f^*(x')\int\limits_{-\infty}^{\infty} f(x'')\frac{1}{2\pi}\int\limits_{-\infty}^{\infty} e^{-ik(x'+x''-x)}dkdx''dx' \\
&= \frac{1}{\sqrt{2\pi}}\int\limits_{-\infty}^{\infty} \frac{1}{\sqrt{2\pi}}\int\limits_{-\infty}^{\infty} f^*(x')e^{ikx'}dx'\frac{1}{\sqrt{2\pi}}\int\limits_{-\infty}^{\infty} f(x'')e^{-ikx''}dx''e^{ikx}dk \\
&= \frac{1}{\sqrt{2\pi}}\int\limits_{-\infty}^{\infty} F^*(k)F(k)e^{ikx}dk = \frac{1}{\sqrt{2\pi}}\int\limits_{-\infty}^{\infty} |F(k)|^2 e^{ikx}dk.
\end{aligned}$$

A special case of the Wiener-Khinchin theorem is Parseval's theorem

$$\int\limits_{-\infty}^{\infty} |f(x)|^2 dx = \int\limits_{-\infty}^{\infty} |F(k)|^2 dk, \tag{D.10}$$

which can be obtained from the Wiener-Khinchin theorem for $x = 0$

$$\begin{aligned}
h_{AC}(0) &= \frac{1}{\sqrt{2\pi}}\int\limits_{-\infty}^{\infty} f^*(x')f(x')dx' = \frac{1}{\sqrt{2\pi}}\int\limits_{-\infty}^{\infty} |f(x)|^2 dx \\
&= \frac{1}{\sqrt{2\pi}}\int\limits_{-\infty}^{\infty} |F(k)|^2 e^{ik0}dk = \frac{1}{\sqrt{2\pi}}\int\limits_{-\infty}^{\infty} |F(k)|^2 dk.
\end{aligned}$$

D.4 Structure functions

A structure function of order p is defined as[3]

$$S_p(f(x)) = \langle [f(x+x') - f(x')]^p \rangle = \frac{1}{\sqrt{2\pi}} \int\limits_{-\infty}^{\infty} [f(x+x') - f(x')]^p dx'. \tag{D.11}$$

The second order structure function is related to the spectrum $|F(k)|$ of the function f like

$$\frac{1}{\sqrt{2\pi}} \int\limits_{-\infty}^{\infty} [f(x+x') - f(x')]^2 dx' = \frac{2}{\sqrt{2\pi}} \int\limits_{-\infty}^{\infty} (1 - e^{ikx}) \left|F(k)\right|^2 dk, \tag{D.12}$$

which can be proved[4] by expanding the second order structure function

$$\begin{aligned} S_2(f(x)) &= \frac{1}{\sqrt{2\pi}} \int\limits_{-\infty}^{\infty} [f(x+x') - f(x')]^2 dx' \\ &= \frac{1}{\sqrt{2\pi}} \left[\int\limits_{-\infty}^{\infty} \left|f(x+x')\right|^2 dx' - 2 \int\limits_{-\infty}^{\infty} f^*(x') f(x+x') dx' + \int\limits_{-\infty}^{\infty} \left|f(x')\right|^2 dx' \right]. \end{aligned}$$

Substituting $x'' = x + x'$ in the first term we get

$$\begin{aligned} S_2(f(x)) &= \frac{1}{\sqrt{2\pi}} \left[\int\limits_{-\infty}^{\infty} \left|f(x'')\right|^2 dx'' - 2 \int\limits_{-\infty}^{\infty} f^*(x') f(x+x') dx' + \int\limits_{-\infty}^{\infty} \left|f(x')\right|^2 dx' \right] \\ &= \frac{2}{\sqrt{2\pi}} \left[\int\limits_{-\infty}^{\infty} \left|f(x')\right|^2 dx' - \int\limits_{-\infty}^{\infty} f^*(x') f(x+x') dx' \right]. \end{aligned}$$

Using Parseval's and the Wiener-Khinchin theorem we obtain the final result

$$\begin{aligned} S_2(f(x)) &= \frac{2}{\sqrt{2\pi}} \left[\int\limits_{-\infty}^{\infty} \left|F(k)\right|^2 dk - \int\limits_{-\infty}^{\infty} \left|F(k)\right|^2 e^{ikx} dk \right] \\ &= \frac{2}{\sqrt{2\pi}} \int\limits_{-\infty}^{\infty} (1 - e^{ikx}) \left|F(k)\right|^2 dk. \end{aligned}$$

---

[3] See Pope (2000).

[4] A sketch of this prove can also be found in Pope (2000, Appendix G).

The structure functions used in the theory of Kolmogorov are the so called longitudinal structure functions of the velocity, which are defined as

$$S_2(v_\parallel(l)) = \langle \left([\boldsymbol{v}(\boldsymbol{x}+\boldsymbol{l}) - \boldsymbol{v}(\boldsymbol{x})] \cdot \frac{\boldsymbol{l}}{l} \right)^p \rangle = \langle \left(v_\parallel(\boldsymbol{x}+\boldsymbol{l}) - v_\parallel(\boldsymbol{x}) \right)^p \rangle. \tag{D.13}$$

They are related to the longitudinal velocity spectrum[5] $\left|V_\parallel(k)\right|^2$ via equation (D.12). Sometimes also second order transverse structure functions are measured. These are defined as

$$S_2(v_\perp(l)) = \langle \left(\frac{|[\boldsymbol{v}(\boldsymbol{x}+\boldsymbol{l}) - \boldsymbol{v}(\boldsymbol{x})] \times \boldsymbol{l}|}{l} \right)^p \rangle. \tag{D.14}$$

The behavior of the second order transverse structure functions for homogeneous turbulence is uniquely determined by the longitudinal structure function (Pope, 2000, p. 192, Eqs. (6.28)). They also show the characteristic 2/3-slope as predicted for the longitudinal structure functions (Frisch, 1995, p.60).

In general structure functions of vectorial quantities like the velocity are tensors, e.g. the general second order structure function of the velocity can be defined as

$$S_{ij}(\boldsymbol{x}, \boldsymbol{l}) = \langle [v_i(\boldsymbol{x}+\boldsymbol{l}) - v_i(\boldsymbol{x})][v_j(\boldsymbol{x}+\boldsymbol{l}) - v_j(\boldsymbol{x})] \rangle. \tag{D.15}$$

But it can be shown that for local isotropy only the longitudinal structure function $S_2(v_\parallel(l)) = S_{11}$ and the transversal structure $S_2(v_\perp(l)) = S_{22} = S_{33}$ are unequal zero (Pope, 2000). Since the transverse structure function is determined by the longitudinal structure function in case of local homogeneity, for homogeneous and isotropic turbulence S_{ij} is determined by the single scalar function $S_{11} = S_2(v_\parallel(l))$ (Pope, 2000).

The third order structure function used in Kolmogorov theory is defined as

$$S_{111}(\boldsymbol{x}, \boldsymbol{l}) = \langle [v_1(\boldsymbol{x}+\boldsymbol{l}) - v_1(\boldsymbol{x})]^3 \rangle, \tag{D.16}$$

which is often simply called $S_3(v(l))$. So the famous four-fifths law of Kolmogorov is actually true only for one component of the third order structure function tensor, but again for homogeneous and isotropic turbulence the third order structure function tensor S_{ijk} is uniquely determined by the single scalar function $S_{111} = S_3(v(l))$.

---

[5] In the literature this is often called kinetic energy spectrum, but this is only true for incompressible flows.

E The divergence equation

We start with the momentum equation (2.2)

$$\frac{\partial}{\partial t}(\rho v_i) + \frac{\partial}{\partial r_j}(v_j \rho v_i) = -\frac{\partial}{\partial r_i} p + \frac{\partial}{\partial r_j} \sigma'_{ij} - \rho \frac{\partial}{\partial r_i} \phi,$$

where we assumed $g_i = -\frac{\partial}{\partial r_i}\phi$. If we make the substitutions $\frac{\partial}{\partial r_i} p \rightarrow \frac{\partial}{\partial r_j} p \delta_{ij}$ and $\frac{\partial}{\partial r_i}\phi \rightarrow \frac{\partial}{\partial r_j}\phi\delta_{ij}$ we can write it in the form

$$\frac{\partial}{\partial t}(\rho v_i) + \frac{\partial}{\partial r_j}(v_j \rho v_i + p\delta_{ij} - \sigma'_{ij}) = -\rho \frac{\partial}{\partial r_j} \phi \delta_{ij}.$$

Taking the divergence of this equation we get

$$\frac{\partial}{\partial t}\left[\frac{\partial}{\partial r_i}(\rho v_i)\right] + \frac{\partial^2}{\partial r_i \partial r_j}(v_j \rho v_i + p\delta_{ij} - \sigma'_{ij}) = -\frac{\partial}{\partial r_i}\left(\rho \frac{\partial}{\partial r_j} \phi \delta_{ij}\right),$$

where we assumed that $\frac{\partial}{\partial t}$ and $\frac{\partial}{\partial r_i}$ commute. Using the continuity equation (2.1) we get a interesting form of the fluiddynamic equations

$$\frac{\partial^2}{\partial t^2}\rho - \frac{\partial^2}{\partial r_i \partial r_j}(v_j \rho v_i + p\delta_{ij} - \sigma'_{ij}) = +\frac{\partial}{\partial r_i}\left(\rho \frac{\partial}{\partial r_j} \phi \delta_{ij}\right). \tag{E.1}$$

In case of no gravitation, the fluiddynamic equation can be written in a form showing some similarity to a wave equation

$$\frac{\partial^2}{\partial t^2}\rho - \frac{\partial^2}{\partial r_i \partial r_j}(v_j \rho v_i + p\delta_{ij} - \sigma'_{ij}) = 0.$$

But despite its simple form, this equation hides an extreme complexity.

Solving for pressure this equation is written like

$$\frac{\partial^2}{\partial r_i^2} p = \frac{\partial^2}{\partial t^2}\rho - \frac{\partial^2}{\partial r_i \partial r_j}(\rho v_i v_j - \sigma'_{ij}) \tag{E.2}$$

and sometimes called the equation for the instantaneous pressure.

F Vlasov-Poisson Equations

The number of particles in the six-dimensional phase space element $dVdP$ at time t can be expressed as

$$N(t) = \int f(r_i, p_i, t) dV dP, \tag{F.1}$$

where $f(r_i, p_i, t)$ is the so called distribution function of particles in phase space. The particle density can be expressed in terms of the distribution function as

$$\rho(r_i, t) = mn(r_i, t) = m \int f(r_i, p_i, t) dP, \tag{F.2}$$

where $n(r_i, t)$ is the number density of all particles and m is the particle mass.

Without collisions, the distribution function satisfies the equation

$$\frac{d}{dt} f(r_i, p_i, t) = 0. \tag{F.3}$$

Writing the time derivative explicitely we get the collisionless Boltzmann equation

$$\frac{\partial}{\partial t} f + \frac{\partial r_i}{\partial t} \frac{\partial f}{\partial r_i} + \frac{\partial p_i}{\partial t} \frac{\partial p_i}{\partial f} = 0. \tag{F.4}$$

With the velocity $v_i = \frac{\partial r_i}{\partial t}$ and the gravitational force $F_i = \frac{\partial p_i}{\partial t} = mg_i$, this equation can be expressed as

$$\frac{\partial}{\partial t} f + v_i \frac{\partial f}{\partial x_i} + mg_i \frac{\partial p_i}{\partial f} = 0. \tag{F.5}$$

Together with the Poisson equation of gravity

$$\frac{\partial}{\partial r_i} g_i = 4\pi G m \int f(r_i, p_i, t) dP \tag{F.6}$$

equations F.5 and F.6 are often called the Vlasov-Poisson system of equations (Peebles, 1980). This system is used in astrophysics to describe the evolution of collisionless matter interacting only by gravity.

However in cosmological N-Body simulations it is not the Vlasov-Poisson system of equations that is solved. In fact, one assumes that the solution of the trajectories of N particles determined by Newtons laws

$$\frac{\partial p_{i,j}}{\partial t} = m_j g_{i,j}, \tag{F.7}$$

$$g_{i,j} = G \sum_{l=1}^{N} m_l \frac{r_{i,j} - r_{i,l}}{(r_{i,j} - r_{i,l})^3}, \tag{F.8}$$

where m_j, m_l and $r_{i,j}, r_{i,l}$ are the position of the jth and lth particle respectively, can be interpreted as Monte-Carlo-Approximation of the Vlasov-Poisson system (Steinmetz, 1999). So every particle in a cosmological N-Body simulation can in fact represent a huge number of particles, which is a major conceptual difference to N-body simulations used to model planetary systems or stars in star clusters, where each particle intends to mimic an actual physical body.

G Hydrostatic equilibrium

G.1 Standard derivation

The equations of hydrostatic equilibrium can be obtained from the equations of fluid dynamics (2.1)-(2.3) assuming $v_i = 0$[1]. This yields

$$\frac{\partial}{\partial t}\rho = 0, \tag{G.1}$$

$$\frac{\partial p}{\partial r_i} = \rho g_i. \tag{G.2}$$

The gravitational force for a sphere with a mass profile $M(r)$ is

$$g_i = -\frac{\partial \Phi}{\partial r_i} = -G\frac{M(r)}{r^2}, \tag{G.3}$$

so the equation of hydrostatic equilibrium for such a configuration is

$$\frac{1}{\rho}\frac{\partial p}{\partial r} = -G\frac{M(r)}{r^2}. \tag{G.4}$$

Substituting the ideal gas equation $p = \rho R_s T$ on the left hand side leads to

$$\frac{1}{\rho}\frac{\partial p}{\partial r} = \frac{R_s}{\rho}\left(\rho\frac{\partial T}{\partial r} + T\frac{\partial \rho}{\partial r}\right) = R_s T\left(\frac{1}{T}\frac{\partial T}{\partial r} + \frac{1}{\rho}\frac{\partial \rho}{\partial r}\right) = R_s T\left(\frac{\partial \ln T}{\partial r} + \frac{\partial \ln \rho}{\partial r}\right). \tag{G.5}$$

Plugging the last result into the equation for hydrostatic equilibrium (G.4), and solving for $M(r)$ gives an useful form of the hydrostatic equilibrium equation

$$M(r) = -\frac{R_s T r}{G}\left(r\frac{\partial \ln T}{\partial r} + r\frac{\partial \ln \rho}{\partial r}\right) = -\frac{R_s T r}{G}\left(\frac{\partial \ln T}{\partial \ln r} + \frac{\partial \ln \rho}{\partial \ln r}\right). \tag{G.6}$$

---

[1] Actually this assumption is a little bit to stringent. For a spherical symmetric system it is enough, that the average radial component of velocity $\langle v_r \rangle = 0$.

G.2 Derivation including turbulent pressure

If we add a turbulent pressure p_t to the ideal gas equation we get for the total pressure

$$p = p_{th} + p_t(l) = \rho R_s T + \frac{1}{3}\rho q^2(l). \tag{G.7}$$

If we substitute this into the equation for hydrostatic equilibrium (G.4), we get an additional term due to the turbulent pressure

$$\frac{\partial p_t(l)}{\partial r} = \frac{1}{3}\rho q^2(l)\left(\frac{\partial \ln q^2(l)}{\partial r} + \frac{\partial \ln \rho}{\partial r}\right). \tag{G.8}$$

Therefore the total gravitational mass within the radius r assuming hydrostatic equilibrium including a turbulent pressure associated with a length scale l is

$$M(r,l) = -\frac{r}{G}\left[R_s T_g\left(\frac{\partial \ln T_g}{\partial \ln r} + \frac{\partial \ln \rho_g}{\partial \ln r}\right) + \frac{q^2(l)}{3}\left(\frac{\partial \ln q^2(l)}{\partial \ln r} + \frac{\partial \ln \rho}{\partial \ln r}\right)\right]. \tag{G.9}$$

H Fluid dynamics in comoving coordinates

H.1 Introduction

On large scales (> 100Mpc) the distribution of matter in the universe is isotropic (it looks the same in all directions) and homogeneous (it is isotropic at each point). But only the space is assumed to be isotropic and homogenous. The observed expansion of the universe singles out a special direction in time.[1]

The physical distance on large scales[2] between two points in such an expanding universe varies with time like

$$r_i = a(t)x_i. \tag{H.1}$$

The factor a is a dimensionless scale factor greater than zero, which must be the same for each component of the distance vector because of the assumed isotropy. The scale factor can only depend on the time t and not on the position x_i because of the assumed homogeneity of space.

The change of the distance with time in an expanding universe is then

$$\dot{r}_i = \dot{a}x_i + a\dot{x}_i. \tag{H.2}$$

The global velocity of a particle $v_i = \dot{r}_i$ which does not move relative to the expanding space ($\dot{x}_i = 0$) is

$$\dot{v}_i = \dot{a}x_i = \frac{\dot{a}}{a}r_i = H(t)r_i \tag{H.3}$$

where H is the so called Hubble parameter. Is a particle moving relative to the expanding space ($\dot{x}_i \neq 0$) then we measure the additional local (also called proper) velocity $u_i = a\dot{x}_i$ of the particle. This local velocity can, according to special relativity, be never greater than the speed of light c. Nevertheless, the global velocity (e.g. the measured escape velocities of galaxies at great distances) can be greater than c (Davis and Lineweaver, 2004). Generally the physical velocity of a particle is the sum of global and local velocity

---

[1] In other words: The universe is not a maximally symmetric 4-dimensional manifold, but can be depicted as maximally symmetric 3-dimensional spacelike sheets in a 4-dimensional spacetime. The metric on such a manifold is the Robertson-Walker-metric.

[2] This is a very important point. If the space would also expand on small scales we couldn't measure the expansion, because everything including our distance measurement device would expand. But on small scales the universe is not homogenous. On small scales the metric of the universe is not a Robertson-Walker metric, but more like a Schwarzschild metric, which is isotropic, but not homogenous.

$$v_i = \dot{a}x_i + u_i(x_i, t). \tag{H.4}$$

H.2 Useful transformations

From the definition of the distance r_i and the velocity v_i in comoving coordinates we get

$$\begin{align}
\frac{\partial}{\partial r_i} &= \frac{1}{a}\frac{\partial}{\partial x_i}, \tag{H.5}\\
\frac{\partial}{\partial r_i} v_i &= \frac{1}{a}\frac{\partial}{\partial x_i} u_i + 3\frac{\dot{a}}{a}, \tag{H.6}\\
\frac{\partial}{\partial r_i} v_j &= \frac{1}{a}\frac{\partial}{\partial x_i} u_j + \frac{\dot{a}}{a}\delta_{ij}, \tag{H.7}\\
\left(\frac{\partial A}{\partial t}\right)_r + v_j\frac{\partial A}{\partial r_j} &= \left(\frac{\partial A}{\partial t}\right)_x + \frac{1}{a}u_j\frac{\partial A}{\partial x_j}, \tag{H.8}\\
A(r_i, v_i, t) &\neq A(x_i, u_i, t). \tag{H.9}
\end{align}$$

With the help of transformation (H.6) and (H.7) we can transform the stress tensor for a newtonian fluid in cartesian coordinates

$$\sigma'_{ij} = 2\eta\left[\frac{1}{2}\left(\frac{\partial}{\partial r_j}v_i + \frac{\partial}{\partial r_i}v_j\right) - \frac{1}{n}\delta_{ij}\frac{\partial}{\partial r_k}v_k\right] + \zeta\delta_{ij}\frac{\partial}{\partial r_k}v_k \tag{H.10}$$

into the stress tensor for a newtonian fluid in comoving coordinates

$$\begin{align}
\sigma'_{ij} =& 2\eta\left[\frac{1}{2}\left(\frac{1}{a}\frac{\partial}{\partial x_j}u_i + \frac{\dot{a}}{a}\delta_{ij} + \frac{1}{a}\frac{\partial}{\partial x_i}u_j + \frac{\dot{a}}{a}\delta_{ji}\right) - \frac{1}{n}\delta_{ij}\left(\frac{1}{a}\frac{\partial}{\partial x_k}u_k + n\frac{\dot{a}}{a}\right)\right] \tag{H.11}\\
&+ \zeta\delta_{ij}\left(\frac{1}{a}\frac{\partial}{\partial x_k}u_k + n\frac{\dot{a}}{a}\right) \tag{H.12}\\
=& 2\eta\left[\frac{1}{2a}\left(\frac{\partial}{\partial x_j}u_i + \frac{\partial}{\partial x_i}u_j\right) + \frac{\dot{a}}{a}\delta_{ij} - \frac{n}{n}\frac{\dot{a}}{a}\delta_{ij} - \frac{1}{na}\delta_{ij}\frac{\partial}{\partial x_k}u_k\right] \tag{H.13}\\
&+ \zeta\delta_{ij}\left(\frac{1}{a}\frac{\partial}{\partial x_k}u_k + n\frac{\dot{a}}{a}\right) \tag{H.14}\\
=& \frac{1}{a}\left\{2\eta\left[\frac{1}{2}\left(\frac{\partial}{\partial x_j}u_i + \frac{\partial}{\partial x_i}u_j\right) - \frac{1}{n}\delta_{ij}\frac{\partial}{\partial x_k}u_k\right] + \zeta\delta_{ij}\left(\frac{\partial}{\partial x_k}u_k + n\dot{a}\right)\right\}. \tag{H.15}
\end{align}$$

H.3 Equations in comoving coordinates

With the help of the relations described in the last section, we can write down the fluid dynamic equations in explicit comoving form

$$\frac{\partial}{\partial t}\rho + \frac{1}{a}\frac{\partial}{\partial x_j}(u_j\rho) = -3\frac{\dot{a}}{a}\rho, \tag{H.16}$$

$$\frac{\partial}{\partial t}(\rho u_i) + \frac{1}{a}\frac{\partial}{\partial x_j}(u_j\rho u_i) = -\frac{1}{a}\frac{\partial}{\partial x_i}p + \frac{1}{a}\frac{\partial}{\partial x_j}\sigma'_{ij} + \rho g_i^* - 4\frac{\dot{a}}{a}\rho u_i, \tag{H.17}$$

$$\begin{aligned}\frac{\partial}{\partial t}(\rho e) + \frac{1}{a}\frac{\partial}{\partial x_j}(u_j\rho e) = &-\frac{1}{a}\frac{\partial}{\partial x_j}(u_j p) + \frac{1}{a}\frac{\partial}{\partial x_j}(u_i\sigma'_{ij}) + \frac{1}{a}u_i\rho g_i^* \\ &-3\frac{\dot{a}}{a}(\rho e + \frac{1}{3}\rho u_i^2 + p),\end{aligned} \tag{H.18}$$

with Newtonian Gravity in comoving coordinates (Poisson Equation)

$$\frac{1}{a}\frac{\partial}{\partial x_i}g_i^* = 4\pi G, \tag{H.19}$$

where $g_i^* = -\frac{1}{a}\frac{\partial\varphi}{\partial x_i}$ and the gauge transformed newtonian potential $\varphi = \phi + \frac{1}{2}a\ddot{a}x_i^2$.

The energy equation is the sum of the equation for the kinetic energy and the internal energy

$$\frac{\partial}{\partial t}(\rho e_k) + \frac{1}{a}\frac{\partial}{\partial x_j}(u_j\rho e_k) = -\frac{1}{a}u_i\frac{\partial}{\partial x_i}p + \frac{1}{a}u_i\frac{\partial}{\partial x_j}\sigma'_{ij} + \frac{1}{a}\rho u_i g_i^* - 5\frac{\dot{a}}{a}\rho e_k, \tag{H.20}$$

$$\frac{\partial}{\partial t}(\rho e_{int}) + \frac{1}{a}\frac{\partial}{\partial x_j}(u_j\rho e_{int}) = -\frac{1}{a}p\frac{\partial}{\partial x_j}u_j - \frac{1}{a}\sigma'_{ij}\frac{\partial}{\partial x_j}u_i - 3\frac{\dot{a}}{a}(\rho e_{int} + p). \tag{H.21}$$

A even simpler form of the equations of fluid dynamics in comoving coordinates can be found by expressing density and pressure in comoving coordinates. The connection between the density in physical coordinates $r_i = a(t)\cdot x_i$ and the comoving coordinates x_i is given by

$$\rho(r_i) = \frac{dM}{dV} = \frac{dM}{dr_1 dr_2 dr_3} = \frac{1}{a(t)^3}\frac{dM}{dx_1 dx_2 dx_3} = \frac{1}{a(t)^3}\rho(x_i) = \frac{1}{a(t)^3}\tilde{\rho} \tag{H.22}$$

and in analogy for the pressure

$$p(r_i) = \frac{1}{a(t)^3}p(x_i) = \frac{1}{a(t)^3}\tilde{p}. \tag{H.23}$$

Because

$$\frac{\partial}{\partial t}\rho = \frac{\partial}{\partial t}\frac{1}{a(t)^3}\tilde{\rho} = \frac{1}{a(t)^3}\frac{\partial}{\partial t}\tilde{\rho} - 3\frac{\dot{a}}{a}\rho \tag{H.24}$$

the source term on the right hand side of the momentum equation (H.17) and energy conservation equation (H.18) is reduced and even vanishes in the mass conservation equation (H.16), so that we can write the system of equations for fluid dynamic in comoving coordinates like

$$\frac{\partial}{\partial t}\tilde{\rho} + \frac{1}{a}\frac{\partial}{\partial x_j}(u_j\tilde{\rho}) = 0, \tag{H.25}$$

$$\frac{\partial}{\partial t}(\tilde{\rho}u_i) + \frac{1}{a}\frac{\partial}{\partial x_j}(u_j\tilde{\rho}u_i) = -\frac{1}{a}\frac{\partial}{\partial x_i}\tilde{p} + \frac{1}{a}\frac{\partial}{\partial x_j}\sigma'_{ij} + \tilde{\rho}g_i^* - \frac{\dot{a}}{a}\tilde{\rho}u_i, \tag{H.26}$$

$$\begin{aligned}\frac{\partial}{\partial t}(\tilde{\rho}e) + \frac{1}{a}\frac{\partial}{\partial x_j}(u_j\tilde{\rho}e) = &-\frac{1}{a}\frac{\partial}{\partial x_j}(u_j\tilde{p}) + \frac{1}{a}\frac{\partial}{\partial x_j}(u_i\sigma'_{ij}) + \frac{1}{a}u_i\tilde{\rho}g_i^* \\ &-\frac{\dot{a}}{a}(\tilde{\rho}e + \frac{1}{3}\tilde{\rho}u_i^2 + \tilde{p}).\end{aligned} \tag{H.27}$$

I Color fields

There are two possibilities to implement a color field c in a fluid code. One can treat color like the density, i.e. the color variable obeys a conservation law like the density

$$\frac{\partial}{\partial t}c + \frac{\partial}{\partial r_j}(v_j c) = 0. \tag{I.1}$$

In this case c will exactly behave like density, if density and color have the same initial value.

On the other hand one can treat it like a specific quantity obeying a conservation law like

$$\frac{\partial}{\partial t}\rho c + \frac{\partial}{\partial r_j}(v_j \rho c) = 0. \tag{I.2}$$

In this case we see that if c is spatially constant at a time t_0, i.e. $c(t_0) = c_0$, $\frac{\partial c(t_0)}{\partial r_j} = 0$, it will stay constant forever

$$\begin{aligned} \frac{\partial}{\partial t}\rho c + \frac{\partial}{\partial r_j}(v_j \rho c) &= 0 \\ \Leftrightarrow \frac{\partial c}{\partial t} + v_j \frac{\partial c}{\partial r_j} &= 0 \\ \Leftrightarrow \frac{d}{dt}c &= 0 \\ \Rightarrow c &= const. = c_0 \end{aligned}$$

Bibliography

Abell, G. O. (1958). The Distribution of Rich Clusters of Galaxies. *ApJS*, 3:211–+. 9

Abell, G. O., Corwin, Jr., H. G., and Olowin, R. P. (1989). A catalog of rich clusters of galaxies. *ApJS*, 70:1–138. 9

Agertz, O., Moore, B., Stadel, J., Potter, D., Miniati, F., Read, J., Mayer, L., Gawryszczak, A., Kravtsov, A., Nordlund, A., Pearce, F., Quilis, V., Rudd, D., Springel, V., Stone, J., Tasker, E., Teyssier, R., Wadsley, J., and Walder, R. (2007). Fundamental differences between SPH and grid methods. *MNRAS*, 380:963–978. 64

Bartelmann, M. (2003). Strong and Weak Lensing by Galaxy Clusters. In Bowyer, S. and Hwang, C.-Y., editors, *Astronomical Society of the Pacific Conference Series*, volume 301 of *Astronomical Society of the Pacific Conference Series*, pages 255–+. 10

Berger, M. J. and Colella, P. (1989). Local adaptive mesh refinement for shock hydrodynamics. *J. Comput. Phys.*, 82(1):64–84. 43

Berger, M. J. and Oliger, J. (1984). Adaptive mesh refinement for hyperbolic partial differential equations. *Journal of Computational Physics*, 53(3):484–512. 43

Bertschinger, E. (1985). Self-similar secondary infall and accretion in an Einstein-de Sitter universe. *ApJS*, 58:39–65. 62

Biermann, L. and Schlüter, A. (1951). Cosmic Radiation and Cosmic Magnetic Fields. II. Origin of Cosmic Magnetic Fields. *Physical Review*, 82:863–868. 64

Boersma, B. J., Kooper, M. N., M., N. T. T., and Wesseling, P. (1997). Local Grid Refinement in Large-Eddy Simulation. *Journal of Engineering and Mathematics*, 32:161–175. 45

Boussinesq, J. (1877). Théorie de l'Écoulement Tourbillant. *Mem. Présentés par Divers Savants Acad. Sci. Inst. Fr.*, 23:46–50. 36

Brüggen, M., Ruszkowski, M., Simionescu, A., Hoeft, M., and Dalla Vecchia, C. (2005). Simulations of Magnetic Fields in Filaments. *ApJ*, 631:L21–L24. 64

Bryan, G. L., Abel, T., and Norman, M. L. (2001). Achieving Extreme Resolution in Numerical Cosmology Using Adaptive Mesh Refinement: Resolving Primordial Star Formation. *sc*, 00:13. 45

Bryan, G. L., L., N. M., Stone, J. M., Cen, R., and Ostriker, J. P. (1995). A piecewise parabolic method for cosmological hydrodynamics. *Computer Physics Communications*, 89:149–168. 49

Canuto, V. M. (1997). Compressible Turbulence. *ApJ*, 482:827–+. 21, 23

Carilli, C. L. and Taylor, G. B. (2002). Cluster Magnetic Fields. *ARA&A*, 40:319–348. 64

Cen, R. and Ostriker, J. P. (1999). Where Are the Baryons? *ApJ*, 514:1–6. 75

Churazov, E., Forman, W., Jones, C., Sunyaev, R., and Böhringer, H. (2004). XMM-Newton observations of the Perseus cluster - II. Evidence for gas motions in the core. *MNRAS*, 347:29–35. 69

Cook, A. W. (1999). A Consistent Approach to Large Eddy Simulation Using Adaptive Mesh Refinement. *Journal of Computational Physics*, 154:117–133. 46

Davé, R., Cen, R., Ostriker, J. P., Bryan, G. L., Hernquist, L., Katz, N., Weinberg, D. H., Norman, M. L., and O'Shea, B. (2001). Baryons in the Warm-Hot Intergalactic Medium. *ApJ*, 552:473–483. 76

Davis, T. M. and Lineweaver, C. H. (2004). Expanding Confusion: Common Misconceptions of Cosmological Horizons and the Superluminal Expansion of the Universe. *Publications of the Astronomical Society of Australia*, 21:97–109. 118

Deiterding, R. (2003). *Parallel adaptive simulation of multi-dimensional detonation structures*. PhD thesis, Brandenburgische Technische Universität Cottbus. 280 pages, 31MB PDF. 44

Dolag, K., Bykov, A. M., and Diaferio, A. (2008). Non-Thermal Processes in Cosmological Simulations. *Space Science Reviews*, 134:311–335. 11, 64

Dolag, K., Grasso, D., Springel, V., and Tkachev, I. (2005a). Constrained simulations of the magnetic field in the local Universe and the propagation of ultrahigh energy cosmic rays. *Journal of Cosmology and Astro-Particle Physics*, 1:9–+. 64

Dolag, K., Vazza, F., Brunetti, G., and Tormen, G. (2005b). Turbulent gas motions in galaxy cluster simulations: the role of smoothed particle hydrodynamics viscosity. *MNRAS*, 364:753–772. 12, 67

Durst, F. (2007). *Fluid Mechanics. An Introduction to the Theory of Fluid Flows.* Springer, Berlin. Deutsche Ausgabe: Durst, Grundlagen der Strömungsmechanik, Springer, Berlin 2006. 99

Eisenstein, D. J. and Hu, W. (1999). Power Spectra for Cold Dark Matter and Its Variants. *ApJ*, 511:5–15. 71

Eisenstein, D. J. and Hut, P. (1998). HOP: A New Group-Finding Algorithm for N-Body Simulations. *ApJ*, 498:137–+. 71

Falle, S. A. E. G. (1994). The Effect of Turbulence on the Largescale Structure of Radio Jets. *MNRAS*, 269:607–+. 46

Favre, A. (1969). Statistical equations of turbulent gases. *SIAM: Problems of hydrodynamics and continuum mechanics*, pages 231–266. 23

Felten, J. E., Gould, R. J., Stein, W. A., and Woolf, N. J. (1966). X-Rays from the Coma Cluster of Galaxies. *ApJ*, 146:955–958. 9

Feynman, R. P. (1964). *Feynman lectures on physics. Volume 2: Mainly electromagnetism and matter.* Reading, Ma.: Addison-Wesley, 1964, edited by Feynman, Richard P.; Leighton, Robert B.; Sands, Matthew. 16

Frisch, U. (1995). *Turbulence. The legacy of A.N. Kolmogorov.* Cambridge: Cambridge University Press, —c1995. 16, 17, 18, 77, 110

Germano, M. (1992). Turbulence - The filtering approach. *Journal of Fluid Mechanics*, 238:325–336. 22

Goldstein, D. E. and Vasilyev, O. V. (2004). Stochastic coherent adaptive large eddy simulation method. *Physics of Fluids*, 16:2497–2513. 46

Gottlöber, S., Yepes, G., Khalatyan, A., Sevilla, R., and Turchaninov, V. (2006). Dark and baryonic matter in the MareNostrum Universe. In Manoz, C. and Yepes, G., editors, *The Dark Side of the Universe*, volume 878 of *American Institute of Physics Conference Series*, pages 3–9. 76

Greiner, W. and Stock, H. (1991). *Hydrodynamik*, volume 2A of *Theoretische Physik*. Harri Deutsch, Frankfurt am Main, 4. aufl. edition. 103, 104

Gunn, J. E. and Gott, J. R. I. (1972). On the Infall of Matter Into Clusters of Galaxies and Some Effects on Their Evolution. *ApJ*, 176:1–+. 62

Gursky, H., Kellogg, E., Murray, S., Leong, C., Tananbaum, H., and Giacconi, R. (1971). A Strong X-Ray Source in the Coma Cluster Observed by UHURU. *ApJ*, 167:L81+. 9

Iapichino, L. and Niemeyer, J. C. (2008). Hydrodynamical adaptive mesh refinement simulations of turbulent flows - II. Cosmological simulations of galaxy clusters. *ArXiv e-prints*. 0801.4729. 71, 84

Jenkins, L. N.-C. (2007). Dwarf Galaxies in the Coma Cluster. http://photojournal.jpl.nasa.gov/catalog/PIA09561. 10

Kaiser, N. (1986). Evolution and clustering of rich clusters. *MNRAS*, 222:323–345. 11

Kang, H., Ryu, D., Cen, R., and Song, D. (2005). Shock-heated Gas in the Large-Scale Structure of the Universe. *ApJ*, 620:21–30. 75

Kellogg, E., Gursky, H., Tananbaum, H., Giacconi, R., and Pounds, K. (1972). The Extended X-Ray Source at M87. *ApJ*, 174:L65+. 9

Knop, R. A., Aldering, G., Amanullah, R., Astier, P., Blanc, G., Burns, M. S., Conley, A., Deustua, S. E., Doi, M., Ellis, R., Fabbro, S., Folatelli, G., Fruchter, A. S., Garavini, G., Garmond, S., Garton, K., Gibbons, R., Goldhaber, G., Goobar, A., Groom, D. E., Hardin, D., Hook, I., Howell, D. A., Kim, A. G., Lee, B. C., Lidman, C., Mendez, J., Nobili, S., Nugent, P. E., Pain, R., Panagia, N., Pennypacker, C. R., Perlmutter, S., Quimby, R., Raux, J., Regnault, N., Ruiz-Lapuente, P., Sainton, G., Schaefer, B., Schahmaneche, K., Smith, E., Spadafora, A. L., Stanishev, V., Sullivan, M., Walton, N. A., Wang, L., Wood-Vasey, W. M., and Yasuda, N. (2003). New Constraints on Ω_M, Ω_Λ and w from an Independent Set of 11 High-Redshift Supernovae Observed with the Hubble Space Telescope. *ApJ*, 598:102–137. 12

Kritsuk, A. G., Norman, M. L., Padoan, P., and Wagner, R. (2007). The Statistics of Supersonic Isothermal Turbulence. *ApJ*, 665:416–431. 19

Kulsrud, R. M. and Anderson, S. W. (1992). The spectrum of random magnetic fields in the mean field dynamo theory of the Galactic magnetic field. *ApJ*, 396:606–630. 64

Kulsrud, R. M. and Zweibel, E. G. (2008). On the origin of cosmic magnetic fields. *Reports of Progress in Physics*, 71(4):046901–+. 64

Landau, L. D. and Lifschitz, E. M. (1991). *Hydrodynamik*, volume 6 of *Lehrbuch der theoretischen Physik*. Akademie Verlag, Berlin. 15, 103

Léonard, S., Terracol, M., and Sagaut, P. (2006). A wavelet-based adaptive mesh refinement criterion for large-eddy simulation. *Journal of Turbulence*, 7:64–+. 46

Lynden-Bell, D. (1967). Statistical mechanics of violent relaxation in stellar systems. *MNRAS*, 136:101–+. 62

Markevitch, M., Forman, W. R., Sarazin, C. L., and Vikhlinin, A. (1998). The Temperature Structure of 30 Nearby Clusters Observed with ASCA: Similarity of Temperature Profiles. *ApJ*, 503:77–+. 85

Mason, P. and Brown, A. (1999). On Subgrid Models and Filter Operations in Large Eddy Simulations. *Journal of the Atmospheric Sciences*, 56:2101–2114. 33

Medvedev, M. V., Silva, L. O., and Kamionkowski, M. (2006). Cluster Magnetic Fields from Large-Scale Structure and Galaxy Cluster Shocks. *ApJ*, 642:L1–L4. 13

Messier, C. (1784). *Connaissance des Temps.* (Paris). 9

Mitran, S. (2001). A Comparison of Adaptive Mesh Refinement Approaches for Large Eddy Simulation. 46

Monin, A. and Yaglom, A. (1971). *Statistical Fluid Dynamics.* MIT Press. 22

Nagai, D., Vikhlinin, A., and Kravtsov, A. V. (2007). Testing X-Ray Measurements of Galaxy Clusters with Cosmological Simulations. *ApJ*, 655:98–108. 65, 67

Navarro, J. F., Frenk, C. S., and White, S. D. M. (1997). A Universal Density Profile from Hierarchical Clustering. *ApJ*, 490:493–+. 62

Norman, M. L. and Bryan, G. L. (1999). Cluster Turbulence. In Röser, H.-J. and Meisenheimer, K., editors, *The Radio Galaxy Messier 87*, volume 530 of *Lecture Notes in Physics, Berlin Springer Verlag*, pages 106–+. 67, 86

Norman, M. L., Bryan, G. L., Harkness, R., Bordner, J., Reynolds, D., O'Shea, B., and Wagner, R. (2007). Simulating Cosmological Evolution with Enzo. *ArXiv e-prints*, 705. 49, 50

Nägele, S. and Wittum, G. (2003). Large-eddy simulation and multigrid methods. *Electronic Transactions on Numerical Analysis*, 15:152–164. 46

Ostriker, J. P. (1993). Astronomical tests of the cold dark matter scenario. *ARA&A*, 31:689–716. 67

Pantano, C., Deiterding, R., Hill, D. J., and Pullin, D. I. (2007). A low numerical dissipation patch-based adaptive mesh refinement method for large-eddy simulation of compressible flows. *Journal of Computational Physics*, 221:63–87. 46

Peebles, P. J. E. (1980). *The large-scale structure of the universe.* Research supported by the National Science Foundation. Princeton, N.J., Princeton University Press, 1980. 435 p. 113

Peebles, P. J. E. and Yu, J. T. (1970). Primeval Adiabatic Perturbation in an Expanding Universe. *ApJ*, 162:815–+. 61

Peterson, J. R., Kahn, S. M., Paerels, F. B. S., Kaastra, J. S., Tamura, T., Bleeker, J. A. M., Ferrigno, C., and Jernigan, J. G. (2003). High-Resolution X-Ray Spectroscopic Constraints on Cooling-Flow Models for Clusters of Galaxies. *ApJ*, 590:207–224. 67

Pfrommer, C. (2005). *On the role of cosmic rays in clusters of galaxies.* Dissertation, LMU München: Faculty of Physics. 61

Pfrommer, C., Springel, V., Enßlin, T. A., and Jubelgas, M. (2006). Detecting shock waves in cosmological smoothed particle hydrodynamics simulations. *MNRAS*, 367:113–131. 74

Plionis, M., López-Cruz, O., and Hughes, D. (2008). *A Pan-Chromatic View of Clusters of Galaxies and the Large-Scale Structure*, volume 740 of *Lecture Notes in Physics*. 61, 63

Pope, E. C. D., Pittard, J. M., Hartquist, T. W., and Falle, S. A. E. G. (2008). The generation of optical emission-line filaments in galaxy clusters. *MNRAS*, pages 253–+. 46

Pope, S. B. (2000). *Turbulent Flows.* Cambridge University Press. 18, 36, 43, 109, 110

Pope, S. B. (2004). Ten questions concerning the large-eddy simulation of turbulent flows. *New Journal of Physics*, 6:35–+. 45

Pratt, G. W. and Arnaud, M. (2002). The mass profile of A1413 observed with XMM-Newton: Implications for the M-T relation. *A&A*, 394:375–393. 85

Price, D. J. (2007). Modelling discontinuities and Kelvin-Helmholtz instabilities in SPH. *ArXiv e-prints*, 709. 64

Rebusco, P., Churazov, E., Böhringer, H., and Forman, W. (2005). Impact of stochastic gas motions on galaxy cluster abundance profiles. *MNRAS*, 359:1041–1048. 69

Rebusco, P., Churazov, E., Böhringer, H., and Forman, W. (2006). Effect of turbulent diffusion on iron abundance profiles. *MNRAS*, 372:1840–1850. 69

Ricker, P. M. and Sarazin, C. L. (2001). Off-Axis Cluster Mergers: Effects of a Strongly Peaked Dark Matter Profile. *ApJ*, 561:621–644. 67

Roettiger, K., Loken, C., and Burns, J. O. (1997). Numerical Simulations of Merging Clusters of Galaxies. *ApJS*, 109:307–+. 67

Roettiger, K., Stone, J. M., and Burns, J. O. (1999). Magnetic Field Evolution in Merging Clusters of Galaxies. *ApJ*, 518:594–602. 64

Rogallo, R. S. and Moin, P. (1984). Numerical Simulation of Turbulent Flows. *Annual Review of Fluid Mechanics*, 16(1):99–137. 25

Sagaut, P. (2006). *Large eddy simulation for incompressible flows an introduction.* Berlin: Springer-Verlag. 28, 33, 34

Sagaut, P., Deck, S., and Terracol, M. (2006). *Multiscale and Multiresolution Approaches in Turbulence.* Imperial College Press. 46

Sarazin, C. L. (1988). *X-ray emission from clusters of galaxies.* Cambridge Astrophysics Series. Cambridge University Press. 61

Sarkar, S. (1992). The pressure-dilatation correlation in compressible flows. *Physics of Fluids*, 4:2674–2682. 34, 41

Schindler, S. and Mueller, E. (1993). Simulations of the evolution of galaxy clusters. 11. Dynamics of the intra-cluster gas. *A&A*, 272:137–+. 67

Schmidt, W. (2004). *Turbulent Thermonuclear Combustion in Degenerate Stars.* PhD thesis, Max-Planck-Insitute für Astrophysik. 33, 53

Schmidt, W. (2007). A Parameter Study of Forced Supersonic Turbulence in Large Eddy Simulations. in press. 42

Schmidt, W., Niemeyer, J. C., and Hillebrandt, W. (2006a). A localised subgrid scale model for fluid dynamical simulations in astrophysics. I. Theory and numerical tests. *A&A*, 450:265–281. 13, 19, 20, 21, 23, 29, 34, 36

Schmidt, W., Niemeyer, J. C., Hillebrandt, W., and Röpke, F. K. (2006b). A localised subgrid scale model for fluid dynamical simulations in astrophysics. II. Application to type Ia supernovae. *A&A*, 450:283–294. 33, 34, 45

Schuecker, P., Finoguenov, A., Miniati, F., Böhringer, H., and Briel, U. G. (2004). Probing turbulence in the Coma galaxy cluster. *A&A*, 426:387–397. 67, 68

Shyy, W. and Krishnamurty, V. (1997). Compressibility effects in modeling complex turbulent flows. *Progress in Aerospace Sciences*, 33:587–645(59). 41, 42

Steinmetz, M. (1999). Numerical Simulations of Galaxy Formation. *Ap&SS*, 269:513–532. 114

Sullivan, P. P., McWilliams, J. C., and Moeng, C.-H. (1996). A grid nesting method for large-eddy simulation of planetary boundary-layer flows. *Boundary-Layer Meteorology*, 80:167–202. 45

Sunyaev, R. A., Norman, M. L., and Bryan, G. L. (2003). On the Detectability of Turbulence and Bulk Flows in X-ray Clusters. *Astronomy Letters*, 29:783–790. 67

Takizawa, M. (2005). Hydrodynamic Simulations of a Moving Substructure in a Cluster of Galaxies: Cold Fronts and Turbulence Generation. *ApJ*, 629:791–796. 67

Terracol, M., Sagaut, P., and Basdevant, C. (2001). A Multilevel Algorithm for Large-Eddy Simulation of Turbulent Compressible Flows. *Journal of Computational Physics*, 167:439–474. 46

Terracol, M., Sagaut, P., and Basdevant, C. (2003). A time self-adaptive multilevel algorithm for large-eddy simulation. *Journal of Computational Physics*, 184:339–365. 46

Tyson, J. A., Wenk, R. A., and Valdes, F. (1990). Detection of systematic gravitational lens galaxy image alignments - Mapping dark matter in galaxy clusters. *ApJ*, 349:L1–L4. 10

Veynante, D. and Vervisch, L. (2002). Turbulent combustion modeling. *Progress in Energy and Combustion Science*, 28:193–266(74). 23

Vikhlinin, A., Kravtsov, A., Forman, W., Jones, C., Markevitch, M., Murray, S. S., and Van Speybroeck, L. (2006). Chandra Sample of Nearby Relaxed Galaxy Clusters: Mass, Gas Fraction, and Mass-Temperature Relation. *ApJ*, 640:691–709. 65, 66, 85

Vikhlinin, A. N. (2002). Coma Cluster: Gas Clouds Strike A Delicate Balance. http://chandra.harvard.edu/photo/2002/0150/. 11

Vogt, C. and Enßlin, T. A. (2005). A Bayesian view on Faraday rotation maps Seeing the magnetic power spectra in galaxy clusters. *A&A*, 434:67–76. 67, 68

Voit, G. M. (2005). Tracing cosmic evolution with clusters of galaxies. *Reviews of Modern Physics*, 77:207–258. 10, 11, 61, 84, 89

Vreman, B., Geurts, B., and Kuerten, H. (1994). Realizability conditions for the turbulent stress tensor in large-eddy simulation. *Journal of Fluid Mechanics*, 278:351–362. 28

Wolf, M. (1906). Über einen Nebelfleck-Haufen im Perseus. *Astronomische Nachrichten*, 170:211–+. 9

Yokokawa, M., Itakura, K., Uno, A., Ishihara, T., and Kaneda, Y. (2002). 16.4-Tflops Direct Numerical Simulation of Turbulence by a Fourier-Spectral Method on the Earth Simulator. Technical report. 19

Zwicky, F. (1933). Die Rotverschiebung von extragalaktischen Nebeln. *Helvetica Physica Acta*, 6:110–127. 9

Zwicky, F. (1937). On the Masses of Nebulae and of Clusters of Nebulae. *ApJ*, 86:217–+. 9

Acknowledgment

First of all, I want to thank my advisor Prof. Dr. Jens Niemeyer for offering me the opportunity to join the International Research Training Group ”Theoretical Astrophysics and Particle Physics” and to work on the forefront of turbulence research in astrophysics. His supervision and amazing intuition for physics always brought me back on track when my work came to a standstill.

I'm indebted to Dr. Wolfram Schmidt, for patiently answering a plethora of questions about his subgrid model and turbulence modeling in general. This work would have been impossible without his contributions. Also many thanks go to Dr. Luigi Iapichino for introducing me into the physics of galaxy clusters. Furthermore he had the astonishing talent of always finding the most interesting literature related to my work.

Many people contributed to the cosmological fluid code Enzo, which I used for this work: Dr. Wolfram Schmidt integrated the routines for random forcing; without them, driven turbulence simulation wouldn't been possible. Christoph Federrath implemented most of the routines for the statistics tool, which I heavily used for this work. Significant bug fixes and code contributions came from Dr. Luigi Iapichino and Markus Hupp. Also, important help was provided by the original developers of Enzo from the other side of the ocean, namely Alexei Kritsuk, Brian O'Shea, Robert Harkness, and David Collins. I thank all these people for their support.

Special thanks go to Greg Harper for proof-reading my thesis. I greatly appreciate his help.

I'm very much obliged to my parents, who patiently supported me during the entire duration of my study. But most of all I have to thank my girlfriend Olga, who never stopped encouraging me and sweetened this stressful time of life.

Zusammenfassung

Galaxienhaufen sind die größten, gravitativ gebundenen Strukturen im Universum. Nach dem hierarchischen Modell der Strukturentstehung, wonach größere, gravitativ gebundene Systeme aus kleineren Systemen entstehen, sind sie damit auch die jüngsten Strukturen im Universum. Daher kann die genaue Verfolgung ihrer Entwicklung, z.B. anhand ihrer Anzahldichte abhängig von der Zeit, zur Messung wichtiger kosmologischer Parameter verwendet werden.

Viele Eigenschaften von Galaxienhaufen können mit optischen Beobachtungen bestimmt werden, die derzeit verlässlichsten Daten erhält man jedoch durch Beobachtungen mit Röntgensatelliten wie z.B. CHANDRA und XMM-Newton. Aus diesen Daten ergeben sich Korrelationen z.B. zwischen Leuchtkraft und Temperatur oder zwischen Masse und Temperatur für Galaxienhaufen. Nimmt man an, dass alleine Gravitation eine Rolle bei der Entstehung von Galaxienhaufen spielt, sollten diese selbstähnlich sein, jedoch stimmen die experimentell gefundenen Relationen nicht mit dieser Annahme überein. Eine physikalische Erklärung, warum die Selbstähnlichkeit verletzt ist, kann die Existenz von turbulenten Strömungen in Galaxienhaufen sein.

Die bisherigen Untersuchungen von Turbulenz in Galaxienhaufen waren jedoch darauf beschränkt, alleine passiv nach Eigenschaften der Strömung in Galaxienhaufen zu suchen, die auf Turbulenz hinweisen. Die aktive Rolle der Turbulenz, d.h. den möglichen Einfluss von klein und kleinstskaligen Geschwindigkeitsfluktuationen auf die Strukturentstehung, zu modellieren war bisher nicht möglich. Ein Grund dafür ist, das die akzeptierte Kolmogorov-Theorie der Turbulenz nur für inkompressible, homogene und isotrope Strömungen angewendet werden kann, Strömungen in der Astrophysik jedoch meist kompressibel, selbstgravitierend und anisotrop sind. Ein zweiter Grund ist, dass die derzeitigen Modelle zur numerischen Beschreibung von Turbulenz (sog. Grobstruktursimulationen) auf der Filterung der fluiddynamischen Gleichungen bei einer bestimmten charakteristischen Längenskala beruhen, was im offenen Widerspruch zu numerischen Methoden der Astrophysik steht, welche mit adaptiven Gittern arbeiten, um die vielen Phänomene auf unterschiedlichsten Längenskalen in astrophysikalischen Umgebungen darzustellen.

Ziel dieser Arbeit war es daher, ein neues numerisches Modell zu entwickeln, welches es ermöglicht Grobstruktursimulationen auch mit adaptiven Gittercodes auszuführen, um Turbulenz über große Längenskalenbereiche konsistent zu simulieren. Da das frei verfügbare Programm Enzo zur Simulation kosmologischer Strömungen adaptive, in Blöcken organisierte Gitter und den wenig-dissipativen PPM-Lösungsalgorithmus benutzt, sollte unser neues Modell in diesen Code implementiert werden.

Um Grobstruktursimulationen mit Enzo zu ermöglichen, implementierten wir eine neue Erhaltungsgleichung für die turbulente Energie in das Programm und koppelten sie an die bereits vorhandenen Erhaltungsgleichungen von Impuls, kinetischer und interner Energie. Wichtigster Punkt und zentrale Idee um Grobstruktursimulationen mit adaptiven Gittern zu ermöglichen, war jedoch die Modifikation der Algorithmen zur Interpolation von turbulenter und kinetischer Energie bei der Erzeugung von Gittern, damit die turbulente Dissipation lokal auf verschiedenen Längenskalen erhalten bleibt.

Nach der Lösung sehr vieler numerischer und technischer Probleme, die uns der schlecht gewartete Enzo-Code leider aufzwang, ist es uns im Rahmen dieser Arbeit gelungen zu zeigen, dass die Annahme lokaler Erhaltung der turbulenten Dissipation zu einem konsistenten Skalierungsverhalten der turbulenten Energie in adaptiven Gittercodes führen kann. Wir konnten auch zeigen, dass unsere Modifikation nicht zu einer Verletzung der Energieerhaltung führt.

Motiviert von diesen Ergebnissen verwendeten wir unser neues numerisches Modell zur Simulation von Galaxienhaufen. Im Rahmen dieser Arbeit wurden dazu eine hochaufgelöste Simulation mit und eine ohne Turbulenzmodell durchgeführt, um den Einfluss unseres Turbulenzmodells auf die Entstehung eines Galaxienhaufens zu untersuchen. Die Auswertung der Simulationen ergab folgendes Bild:

- Unser Turbulenzmodell hat keinen signifikanten Einfluss auf Massenanteile der unterschiedlichen Gasphasen im interstellaren Medium.

- Die zeitlichen Entwicklung der turbulenten Energie lässt darauf schließen, dass alle Gasphasen auf der Längenskala einer Galaxie genug Zeit hatten, um im heutigen Universum eine turbulente Kaskade auszubilden. Wir konnten auch zeigen, dass die Produktion und Dissipation turbulenter Energie im heutigen Universum praktisch im Gleichgewicht zu sein scheint.

- Die Turbulenz auf der Längenskala einer Galaxie ist Unterschallturbulenz, die mittlere turbulente Machzahl bei einer Rotverschiebung $z = 0$ beträgt etwa 0.2.

- Große Fluktuationen der turbulenten Energie bei beginnender Galaxienhaufenbildung deuten darauf hin, dass „gewaltsames“Verschmelzen kleinerer zu großen Strukturen zu turbulenten Strömungen führt.

- Turbulenz in Galaxienhaufen wird durch die Akkretion kleinerer Strukturen nur am äußeren Rand ($r > R_{vir}$) getrieben. Dabei lässt sich aus der räumlichen Verteilung der turbulenten Energie auf die Akkretionsgeschichte des Galaxienhaufens zurückschließen, zumindest solange, bis die turbulenten Geschwindigkeitsfluktuationen in thermische Energie umgewandelt sind.

- Aus dem Skalierungsverhalten der turbulenten Energie lässt sich ableiten, dass Kräfte auf einer Längenskala von $\approx 100\,\mathrm{kpc\ h^{-1}}$ Energie in das System einkoppeln und sich zu kleineren Längenskalen hin eine turbulente Kaskade ausbildet. In den Radialprofilen des Galaxienhaufens findet man den Maximalwert der turbulenten Energie bei $r = 0.5\ R_{vir}$, wahrscheinlich verursacht durch die starke Abbremsung und damit verbundenen Verwirbelung von Material, wenn es auf den Rand des Galaxienhaufen $r = R_{vir}$ trifft.

- Aus den Radialprofilen folgt auch, dass nur im Zentrum ein signifikanter Einfluss unseres Turbulenzmodells auf die thermodynamischen Eigenschaften des Galaxienhaufens besteht. Aus dem effektiven adiabatischen Index ergibt sich, dass mit unserem Turbulenzmodell das interstellare Medium im Zentrum des Galaxienhaufens kühlt, d.h. die Entropie und die Temperatur sind niedriger, die Dichte und Geschwindigkeitsdispersion höher als ohne Turbulenzmodell.

Ausgehend vom letztgenannten Punkt kann man auch vermuten, dass Turbulenz als Mechanismus zur Lösung des „Überkühlungsproblems“ nicht in Frage kommt. Desweiteren führten vorläufige, niedrigaufgelöste Simulationen von Galaxienhaufen zu dem interessanten Resultat, dass die Kolmogorovkonstante im Skalierungsgesetz der turbulenten Geschwindigkeitsfluktuationen im Galaxienhaufenzentrum eine Größenordnung höher als in inkompressibler Turbulenz zu sein scheint.

Ein wichtiger Punkt bei der Quantifizierung von Turbulenz, der speziell in unserer Arbeit offensichtlich wurde, ist die Skalenabhängigkeit der turbulenten Energie und damit auch des turbulenten Druckes. Oft wird dies in der astrophysikalische Literatur nicht berücksichtigt, was viele Aussagen hinsichtlich der Stärke von Turbulenz unvollständig macht. Die Frage jedoch, ob mit einer skalenabhängigen turbulenten Energie, wie sie sich aus der Kolmogorov-Theorie und in unserem Turbulenzmodell ergibt, wirklich Turbulenz in selbstgravitierenden Strömungen korrekt beschrieben werden kann, können wir nicht beantworten. Ein besseres Verständnis selbstgravitierender, turbulenter Strömungen scheint daher unerlässlich und extrem wichtig für die weitere Erforschung von Turbulenz in der Astrophysik.

Lebenslauf

Name:		Andreas Maier
Geburtsdatum:		07. 06. 1978
Geburtsort:		Coburg
Staatsangehörigkeit:		deutsch
Schulbildung:	1984 – 1988	Grundschule Weitramsdorf/Scheuerfeld
	1988 – 1997	Gymnasium Ernestinum in Coburg Abschluss: *Allgemeine Hochschulreife*
Wehrdienst:	1997 – 1998	Stabsdienst in der Infanterieschule Hammelburg
Studium:	1998 – 2001	Physikstudium an der Julius–Maximilians–Universität in Würzburg
	2001 – 2002	Auslandsstudium der Physik als Graduate Student an der Rutgers State University of New Jersey, USA Abschluss: *Master of Science* Masterthesis: *Hermite Multi-Level Neighbor Scheme*
	2002 – 2005	Fortsetzung des Physikstudiums an der Julius–Maximilians–Universität in Würzburg Abschluss: *Diplom–Physiker* Diplomarbeit: *Detonationsfronten in teilweise verbranntem Sternmaterial*
Promotion:	seit 2005	Promotion bei Prof. Niemeyer am Astrophysikalischen Institut der Universität Würzburg als Stipendiat des *Graduiertenkollegs ”Theoretische Astrophysik und Teilchenphysik”* der DFG Dissertation: *Adaptively Refined Large-Eddy Simulations of Galaxy Clusters*

Erklärung

Ich erkläre, dass das Thema dieser Arbeit nicht identisch ist mit dem Thema einer von mir bereits für ein anderes Examen eingereichten Arbeit. Ich erkläre weiterhin, dass ich die Arbeit nicht bereits an einer anderen Hochschule zur Erlangung eines akademischen Grades eingereicht habe.

Ich versichere, dass ich diese Arbeit selbstständig verfasst und keine anderen Hilfsmittel als die angegebenen Quellen benutzt habe.

Würzburg, 15. Dezember 2008